

ISSN 1450-7404

# Journal of Research in Physics

Volume 30  
Number 1  
2004



DEPARTMENT OF PHYSICS

Faculty of Sciences  
University of Novi Sad - Novi Sad - Serbia and Montenegro

# Journal of Research in Physics

---

**Editor**  
Mario Škrinjar

**Editor-in-Chief**  
Ištvan Bikit

## INTERNATIONAL EDITORIAL BOARD

**Lajos Bata**  
Research Institute for  
Solid State Physics  
Budapest, Hungary

**Nikos Flytzanis**  
Physics Department  
University of Crete  
Iraklion, Greece

**Kazuo Tanaka**  
Institute of Laser  
Engineering  
Osaka, Japan

**Emilio Marquez Navarro**  
Departamento de Física  
de la Materia Condensada  
Universidad de Cadiz  
Cadiz, Spain

**Padma Shukla**  
Ruhr - Universität Bochum  
Bochum, Germany

**Stevica Djurović**  
**Svetlana Lukić**  
**Zoran Mijatović**  
**Jaroslav Slivka**  
**Jovan Šetrajić**  
Department of Physics  
University of Novi Sad  
Novi Sad  
Serbia

**Ivan Aničin**  
**Jaroslav Labat**  
**Jagoš Purić**  
Physical Faculty  
University of Belgrade  
Belgrade  
Serbia

**Milan Dimitrijević**  
Astronomical Observatory  
Belgrade  
Serbia

**Zoran Popović**  
Institute of Physics  
Belgrade  
Serbia

---

**Published by:** Department of Physics, Faculty of Sciences, University of Novi Sad,  
Trg Dositeja Obradovića 4, 21000 Novi Sad, Serbia

Phone: +381-21-455318

Fax: +381-21-459367  
<http://www.if.ns.ac.yu>

E-mail: [fizika@uns.ns.ac.yu](mailto:fizika@uns.ns.ac.yu)

## Magnetic Susceptibility of Glasses of the Sb-As-S-Se-I System

F. Skuban, S. R. Lukić, Yu. S. Tver'yanovich\*, D. M. Petrović, S. J. Skuban  
*Department of Physics, Faculty of Sciences, University of Novi Sad,*

*Trg D. Obradovića 4, 21000 Novi Sad*

*\*Department of Chemistry, St. Petersburg State University,  
Universitetsky pr. 2, Stary Petergof, 198904 St. Petersburg, Russian Federation*

Received: May 5, 2004

### Abstract

As part of a general physical characterization of amorphous materials of the type  $(\text{As}_2\text{Se}_3)_{100-x}(\text{SbSI})_x$ , their magnetic susceptibility was measured at room temperature. Measurements were carried out before and after thermal treatment of samples above the softening temperature. Structure of the glasses from this pseudobinary system was also studied by recording high-temperature X-ray diffraction spectra. The aim was to identify structural units forming the spatial network of the material. Based on the supposed structure, total diamagnetic susceptibilities of the glasses were calculated on the basis of the contributions of particular atoms (ions).

*Key words:* Magnetic susceptibility, chalcogenide glasses, X-ray diffraction

### 1. Introduction

Amorphous chalcogenides that are being subject of investigation in the present work can be presented by the chemical formula  $(\text{As}_2\text{Se}_3)_{100-x}(\text{SbSI})_x$  ( $x$  atomic percent). It is a pseudobinary system with the variable ratio of classical amorphous compound  $\text{As}_2\text{Se}_3$  and the molecule of antimony sulfoiodide,  $\text{SbSI}$ , which in the monocrystal form is characterized as a ferroelectric [1, 2]. These glasses have been studied with the aim of examining the possibility of obtaining some new structures on the basis of the materials with amorphous internal network, the structures that will have a higher quality in respect of dielectric properties. In view of the fact that the physical properties of amorphous materials can be modified in different ways, first of all by continuous variation of the ratio of the starting components and then by potential modification of the synthesis regime and subsequent physical (thermal, optical, electric, magnetic, irradiation, etc.) treatment, the aim is to find out optimal conditions for obtaining materials with desired physical properties. First of all, this is related to the formation of crystalline centers of antimony sulfoiodide in the glass structure, as well as to the improvement of other properties such as mechanical, thermal, optical, tendency towards crystallization, etc.

In view of the above and with the aim of obtaining a deeper insight into general physical and chemical characteristics of these materials, their magnetic susceptibility was

measured at room temperature. Besides, the diamagnetic properties of these glasses were calculated by summing up the contributions of the particular atoms, or more correctly, of their ions. As the predominant chemical bonds involved in the investigated glasses (i.e. glass-crystalline materials) are of covalent type, it was useful to compare the experimental and calculated values, and to assess the behavior of particular susceptibility components as a function of the material composition.

## 2. Experimental details

The synthesis of the materials in the pseudobinary system  $(\text{As}_2\text{Se}_3)_{100-x}(\text{SbSI})_x$  was carried out by standard procedure, by following of the previously established cascade regime of heating [3, 4]. The evacuated glass ampoules containing high-purity elementary components were held at the maximal temperature of the synthesis of  $650^\circ\text{C}$  for at least 20 h. Cooling was carried out either in air or in  $\text{Al}_2\text{O}_3$  powder. Amorphous character of the structure of obtained materials was confirmed by X-ray diffraction and polarization microscopy.

In the above way we synthesized materials with  $x = 0, 20, 30, 50, 70$  and  $80$  at. % SbSI. The corresponding glass samples for magnetic measurements were subjected to additional thermal treatment, to initiate formation of the SbSI crystalline centers as the carriers of ferroelectric properties. Thermal treatment was carried out at  $215 \div 220^\circ\text{C}$  during  $15 \div 20$  min. Masses of the glass samples as prepared and glassy-crystalline (thermally treated) samples for magnetic measurements were in the range of  $80 \div 130$  mg.

Magnetic measurements were carried out in the specially constructed apparatus described in [5, 6], at room temperature and at a mean magnetic induction of  $0.65 \div 0.66$  T. The method is absolute and in the case of materials containing no ferromagnetic admixtures, does not depend either on the mass of the sample used in the analysis or strength of the magnetic field employed. The susceptibility was calculated using the expression:

$$\chi = \frac{k^* \Delta Y}{LB^2} \quad (1)$$

where  $k^*$  is the constant characteristic of the magnet;  $\Delta Y$  is the deviation of the sample placed in the magnetic field from the equilibrium position (without the field);  $L$  is the length of the thread on which the samples were hanged;  $B$  is the intensity of magnetic induction. Measurements were repeated  $8 \div 10$  times for each sample, and the results were treated statistically. The relative standard deviation of individual measurement, as well as the value of standard deviation for a series of measurements, did not exceed 1 %.

On the other hand, in order to calculate total magnetic susceptibility of the investigated glasses and glass-crystals on the basis of contributions of particular atoms (or better to say ions) use was made of the values given for the ions in different oxidation states. Before that it was necessary to identify the form of the elements present in the structural network, that is to break it down into the constituent structural units. To this end we recorded X-ray diffraction on partly crystalline samples at room temperature on the one hand and at elevated temperatures on the other. The diffraction on selected samples was recorded using a Philips PW 1373 PW 1965/50 diffractometer with the camera for high-temperature analysis Anton Paar HTK-10. The camera had as a sample carrier of Pt or Ta, so that their diffraction maxima were recorded too.

### 3. Results and Discussion

Amorphous internal structure of the materials was confirmed by analyzing the diffractograms of the as-prepared samples as well as by polarization microscopy. Subsequent thermal treatment at temperatures exceeding the glass transition temperature  $T_g$ , i.e. in the range of 215 – 220°C, yielded formation of SbSI crystalline centers (Figure 1, diffractogram for  $x = 70$  at. % SbSI at 260°C). Certainly, the appearance of this structural unit was significantly facilitated in the compositions with more than 50 at. % SbSI, which exhibits tendency to crystallize. In contrast to that, in the materials with  $x = 20$  and 30 at. % SbSI, formation of these crystalline centers is practically almost blocked by the non-crystalline lattice of the main glass matrix. The spectrum of X-ray diffraction on the materials with lower antimony sulfiodide content at 300°C (Figure 1, diffractogram for  $x = 20$  at. % SbSI) confirms this statement, i.e. the predominant presence of antimony selenide ( $\text{Sb}_2\text{Se}_3$ ) and arsenic selenide ( $\text{As}_2\text{Se}_3$ ).

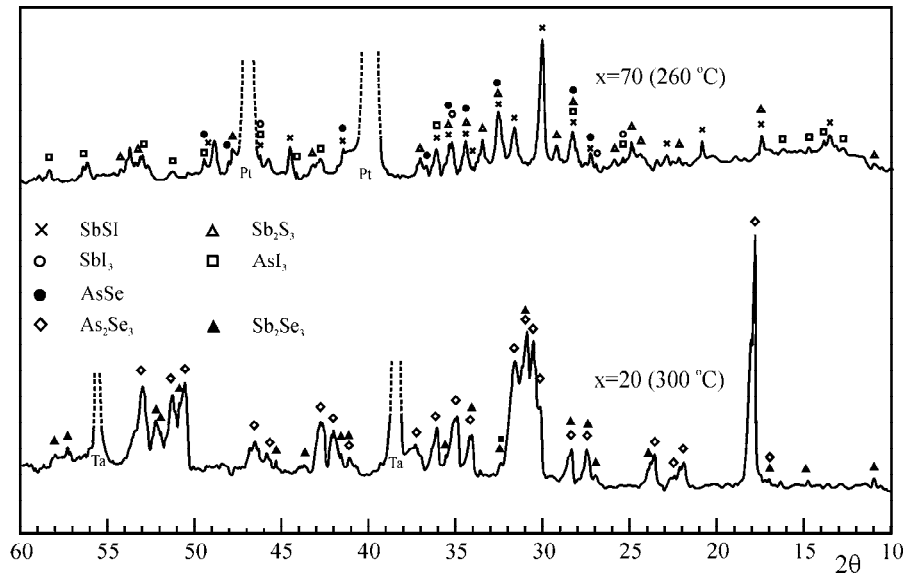


**Figure 1.** X-ray diffractograms of the glasses of the type  $(\text{As}_2\text{Se}_3)_{100-x}(\text{SbSI})_x$  at elevated temperatures.

Magnetic measurements showed that the examined materials are diamagnetic, which could be supposed on the basis of their composition. The measured susceptibility values were in the range of the literature data for the glass  $\text{As}_2\text{Se}_3$  ( $3.39 \cdot 10^{-9} \text{ m}^3/\text{kg}$  [7],  $3.41 \cdot 10^{-9} \text{ m}^3/\text{kg}$  [8]) and changed very little with the change in composition (Figure 2, Table 1). Higher SbSI contents yielded enhancement in the diamagnetic character. This can be a consequence of a decrease of the paramagnetic component in total magnetic characteristics, more exactly of the polarization (Van Vleck paramagnetism). In the case of a more complex structure and appearance of new structural units, an increase in population of the broken bonds and deformation of glass matrix can be sometimes observed, which results in the increase of paramagnetism. However, in such case one can think that more probable is statistical distribution of the mentioned constituent units, making their interactions increase the symmetry of the electronic charge of the existing atomic groups. In the solid solutions, to which the investigated glass system belongs, this causes a decrease of the polarization paramagnetism [9-12].

**Table 1.** Values of magnetic susceptibility for the glasses of the type  $(\text{As}_2\text{Se}_3)_{100-x}(\text{SbSI})_x$  (in the units  $10^{-9} \text{ m}^3/\text{kg}$ )  
 $\chi_{exp1}$  - glasses prior to thermal treatment;  $\chi_{exp2}$  - glasses after thermal treatment;  
 $\chi_d^{calc}$  - calculated values of magnetic susceptibility.

SbSI content [at. %]	$\chi_{exp1}$	$\chi_{exp2}$	$\chi_d^{calc}$
0	-3.46	—	-5.26
20	-3.59	-3.60	-5.15
30	-3.61	-3.60	-5.10
50	-3.70	-3.65	-5.00
70	-3.80	-3.76	-4.91
80	-3.83	-3.79	-4.87

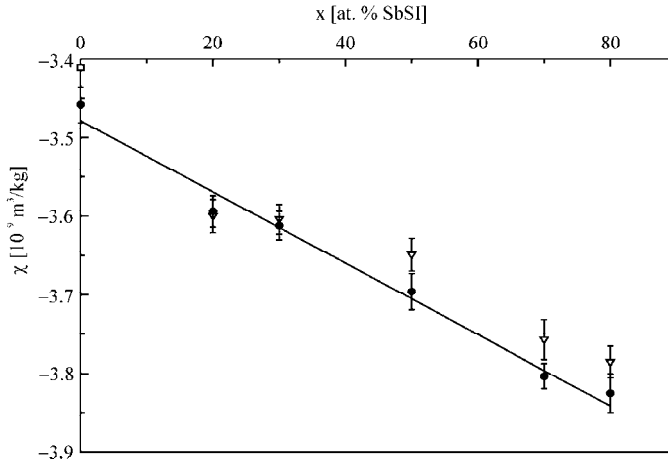


**Figure 2.** Dependence of measured susceptibility values on SbSI content in the glasses of the type  $(\text{As}_2\text{Se}_3)_{100-x}(\text{SbSI})_x$  before ( $\bullet$ ) and after ( $\nabla$ ) thermal treatment. Symbol  $\square$  stands for the literature value [8].

treatment can in some cases cause migration of some impurity elements closer to the surface and spin pairing, yielding the situation as if there were some sort of ferromagnetic behavior of the material. However, the probability of this in our case was low because the changes were too small to serve as the basis for such a conclusion. Besides, for the compositions with  $x = 20$  and  $30$  at. % SbSI, with a low level of the component with crystallization tendency, the paramagnetism changes were hardly evident because the mentioned thermal treatment changed insignificantly the glass network. The linearity of the  $\chi$  function with composition is quite acceptable, and is also in agreement with the literature data for the glassy  $\text{As}_2\text{Se}_3$ .

Finally, the experimental values of magnetic susceptibility measurements were compared with those obtained by calculation on the basis of ionic contributions taken from tables [13]. The analysis of the diffractograms from Figure 1, obtained for partly crystalline samples, yields to the conclusion that the investigated materials contained the following structural units: SbSI,  $\text{Sb}_2\text{S}_3$ ,  $\text{Sb}_2\text{Se}_3$ ,  $\text{SbI}_3$ ,  $\text{AsI}_3$ ,  $\text{AsSe}$ ,  $\text{As}_2\text{Se}_3$ ,... All ions in

The analysis of the obtained results shows that there is an insignificant decrease of the diamagnetism after thermal treatment of glass samples at  $215 \div 220^\circ\text{C}$  (Figure 2, Table 1). This can have different causes but it may also be explained by the changes in the material paramagnetism. The appearance of crystalline centers in the glass matrix after thermal treatment leads to such deformations of the network, i.e. changes in the degree of symmetry of electron density of covalent bond paired electrons, which influences the Van Vleck susceptibility component [9-12]. As second, thermal

these constituent units of the structural matrix are present in the unchanged oxidation states:  $\text{As}^{3+}$ ,  $\text{Sb}^{3+}$ ,  $\text{S}^{2-}$ ,  $\text{Se}^{2-}$ ,  $\text{I}^-$ , and the corresponding contributions to the diamagnetic susceptibility are presented in Table 2.

**Table 2.** Values of molar diamagnetic susceptibility of the ions involved in the investigated materials [13].

ion	$\text{As}^{3+}$	$\text{Sb}^{3+}$	$\text{S}^{2-}$	$\text{Se}^{2-}$	$\text{I}^-$
$\chi_d [-4\pi \cdot 10^{-12} \text{ m}^3/\text{mol}]$	9	17	38	48	52

For each composition we calculated the value of total diamagnetism, first molar, and then the mass one. Molar susceptibility increased with increase in SbSI content, but as the molar mass of the investigated compositions increased too, the calculated magnetic susceptibility  $\chi_d^{calc}$  showed a general decreasing trend (Figure 3).

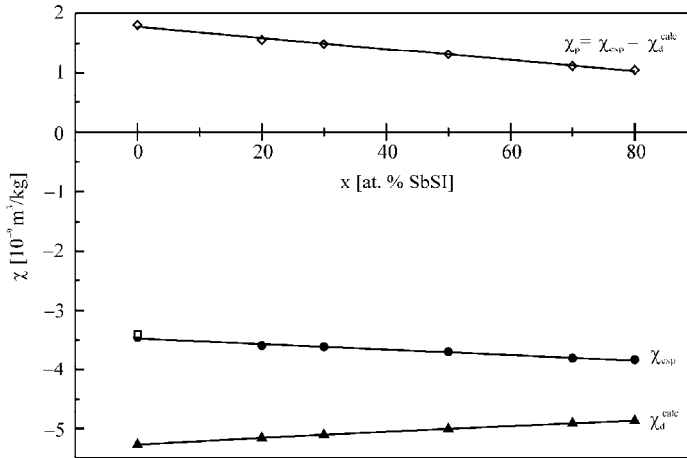


**Figure 3.** Dependence of measured susceptibility values ( $\chi_{exp}$ ) on SbSI content for the glasses of the type  $(\text{As}_2\text{Se}_3)_{100-x}(\text{SbSI})_x$  before thermal treatment and calculated diamagnetism values ( $\chi_d^{calc}$ ). Symbol  $\square$  stands for the literature value [8].

$$\% \text{ bond ionic character} = 100 \% \times \left(1 - e^{-0.25(x_A - x_B)^2}\right) \quad (2)$$

where  $(x_A - x_B)$  is the difference in the electronegativities of particular elements. Thus we obtained that the ionic ratio of the chemical bonds As—Se, As—I, As—Sb, Sb—S, Sb—Se, and Sb—I did not exceed 9 %. It is also difficult to account for the diamagnetic contributions of interatomic bonds because of the lack of reliable data for them, as well as because of the difficulties in the quantitative analysis of materials involving a large number of structural units in their composition.

Besides, it has also been observed a decrease in the difference between the calculated and experimental values with increase in the SbSI content. Probably, the Van Vleck paramagnetic component decreases with increased complexity of the material. As already mentioned, the interaction of numerous and statistically uniformly distributed structural units, leads to an increased symmetry of the electronic cloud, and this may be a sufficient reason for the observed behavior of magnetic properties in this pseudobinary system.

calculated magnetic susceptibility  $\chi_d^{calc}$  showed a general decreasing trend (Figure 3).

This is in contrast to the experimentally found trend of the concentration dependence of mass susceptibility. The disagreement is primarily a consequence of the conditionality of the calculation carried out only on the basis of ionic contributions of the particular elements because of the prevailing covalent character of chemical bonds in these glasses. Namely, the degree of ionic character of the bonds can be calculated from the Pauling relation [14]:

## 4. Conclusion

On the basis of the above discussion it can be concluded that the glasses of the system  $(\text{As}_2\text{Se}_3)_{100-x}(\text{SbSI})_x$  with  $x = 20, 30, 50, 70$  and  $80$  at. % SbSI are typical diamagnetics, with very small differences in their susceptibility. The susceptibility values show an approximately linear increase with increase in the SbSI content in the glasses. Thermal treatment of the materials with the aim of initiating partial crystallization of SbSI in the glass matrix exhibited an insignificant decrease of diamagnetism, which is a possible consequence of the change in the Van Vleck (polarization) component of paramagnetism, reflecting the deformation of the structural matrix. Materials with SbSI content below 50 at. % did not show such tendency.

Finally, the conditional comparison of experimental values with total diamagnetic contributions of individual ions in the composition leads to the conclusion that the observed differences are mainly a consequence of the enhanced covalent character of chemical bonds involved in these chalcogenide glasses, whereas the calculation was based on the existence of mostly ionic bonds. The opposite concentration changes of the experimental and calculated values are probably a consequence of the change in polarization component of paramagnetism appearing in more complex compositions of these solid solutions.

## Acknowledgments

This work was partly financed by the Ministry for Science and Environmental Protection of the Republic of Serbia, within the project "Amorphous and Nanostructural Chalcogenides and Ceramics", No. 1812.

## References

1. E. Fatuzzo, G. Harbeke, W. Y. Merz et al., *Physics Review B* **127**, 6, 2036 (1962).
2. V. M. Fridkin, *Segnetoelektriki - poluprovodniki*, p. 408, (Nauka, Moskva, 1976).
3. A. F. Petrović, D. M. Petrović, M. I. Avramov, V. V. Khiminets, XL Conf. ETRAN, Budva, Yugoslavia, p. 482 (1996).
4. F. Skuban, I. Guth, A. F. Petrović, Ž. N. Popović, M. M. Garić, XIV Nat. Conf. Phys. Cond. Mat., Ioannina, Greece, p. 53 (1998).
5. Yu. S. Tver'yanovich, *Vest. LGU* **2**, 144 (1977).
6. I. Guth, PhD Thesis, Faculty of Sciences, University of Novi Sad, Yugoslavia (2001).
7. L. A. Baydakov, L. N. Blinov, Yu. N. Zubenko and all, *Vestn. LGU, Ser. Fizika i khimiya* **4**, 40 (1966).
8. M. S. Gutenev, *Fizika i khimiya stekla* **14**, 6, 874 (1988).
9. Z. U. Borisova, *Khimiya stekloobraznih poluprovodnikov*, p.247, (Izd-vo LGU, Leningrad, 1972).
10. M. S. Gutenev, I. V. Viktorovskiy, L. A. Baydakov, A. V. Pazin, *Fizika i khimiya stekla* **4**, 4, 350 (1975).

11. Ja. G. Dorfman, *Diamagnetizm i khimicheskaya svyaz*, p. 281, (Fizmatgiz, Moskva, 1961).
12. K. D. Tsendin, *Elektronnie yavleniya v khalkogenidnih stekloobraznih poluprovodnikah*, p. 486, (Nauka, Sankt-Petersburg, 1996).
13. E. A. Boudreaux, L. N. Mulay, *Theory and Applications of Molecular Paramagnetism*, (John Wiley & Sons, New York, 1976).
14. L. Pauling, *The Nature of the Chemical Bond*, p. 644, (Cornell University Press, New York, 1960).

## Structure and Magnetic Properties of the Solid Solutions of (Al<sub>1-x</sub>Fe<sub>x</sub>)(H<sub>2</sub>O)<sub>6</sub>(NO<sub>3</sub>)<sub>3</sub>·3H<sub>2</sub>O Type

M. Vučinić-Vasić<sup>a</sup>, M. Mitrić<sup>b</sup>, A. Kapor<sup>c</sup>, N. Furmanova<sup>d</sup>

<sup>a</sup>Faculty of Technical Sciences, University of Novi Sad,

Trg D. Obradovića 6, 21000 Novi Sad, Serbia and Montenegro

<sup>b</sup>Institute of Nuclear Sciences "Vinca", Laboratory of Solid State Physics,

P.O. Box 522, 11001 Belgrade, Serbia and Montenegro

<sup>c</sup>Department of Physics, Faculty of Sciences, University of Novi Sad,

Trg D. Obradovića 4, 21000 Novi Sad, Serbia and Montenegro

<sup>d</sup>Russian Academy of Sciences, Institute of Crystallography,

Leninskii prosp. 59, 117333 Moscow, Russia

Received: June 1, 2004

### Abstract

In this work we present results of the refinement of the single crystal structure of the solid solution (Al<sub>1-x</sub>Fe<sub>x</sub>)(H<sub>2</sub>O)<sub>6</sub>(NO<sub>3</sub>)<sub>3</sub>·3H<sub>2</sub>O ( $x = 0.5$ ) and measurements of the temperature dependence of magnetic susceptibility of these solid solutions ( $x = 0.15; 0.20; 0.25; 0.50; 0.75$ ). A possible correlation between the crystal structure and magnetic properties of these materials is explored.

The solid solutions were obtained by slow crystallization from saturated aqueous solutions of initial components Al(III) and Fe(III) hexaaqua-nitrate-trihydrates.

The refinement of the single crystal structure of the solid solution ( $x = 0.5$ ) confirmed isostructurality with initial components. Final cation distribution in studied single crystal was (Al<sub>0.68</sub>Fe<sub>0.32</sub>)(H<sub>2</sub>O)<sub>6</sub>(NO<sub>3</sub>)<sub>3</sub>·3H<sub>2</sub>O. Geometry analysis of the refined structure confirmed the existence of the regular octahedral surrounding of central metal ion (Fe<sup>3+</sup> or Al<sup>3+</sup>) with water molecules.

The magnetic susceptibility of the solid solutions was measured by the Faraday method in the temperature range from 78 K to room temperature (298 K). The values of the effective magnetic moments for Fe<sup>3+</sup> ions agree, within error limit, with spin only value of free Fe<sup>3+</sup> ion. Calculated values of the effective magnetic moments confirmed that iron ions are in the high-spin state in the octahedral surrounding of water molecules.

*Key words:* Crystal structure, crystal fields, magnetic properties.

### 1. Introduction

Previous investigations of X-ray powder diffraction spectra of the solid solutions (Al<sub>1-x</sub>Fe<sub>x</sub>)(H<sub>2</sub>O)<sub>6</sub>(NO<sub>3</sub>)<sub>3</sub>·3H<sub>2</sub>O [1] as well as the similar (Al<sub>1-x</sub>Cr<sub>x</sub>)(H<sub>2</sub>O)<sub>6</sub>(NO<sub>3</sub>)<sub>3</sub>·3H<sub>2</sub>O [2] indicated that these solid solutions possess unlimited component solubility and that

they are isostructural with initial components. The phase transformations in the solid solution  $(\text{Al}_{1-x}\text{Fe}_x)(\text{H}_2\text{O})_6(\text{NO}_3)_3 \cdot 3\text{H}_2\text{O}$  show that investigated materials belong to the solid solution of substitution type [3].

It is known that Al(III) and Fe(III) hexaaqua-nitrate-trihydrates crystallize in the centrosymmetric space group  $P2_1/c$  (monoclinic system) [4, 5]. Metal ions occupy special positions  $2a$  (0, 0, 0) and  $2d$  (0.5, 0, 0.5) with local symmetry  $\bar{1}$ . Occupation factor of special positions is 0.5. The analysis of the structures of Al(III), Fe(III) and Cr(III) hexaaqua-nitrate-trihydrates indicates that the octahedral coordination of the central metal ion by water molecules is present. The remaining three molecules are bonded as crystalline water and build hydrogen bonds with the oxygen from the octahedral surrounding as well as with nitrate groups. Nitrate groups form layers in  $bc$  crystallographic planes, which alternate with layers formed by the octahedra (Figure 1).

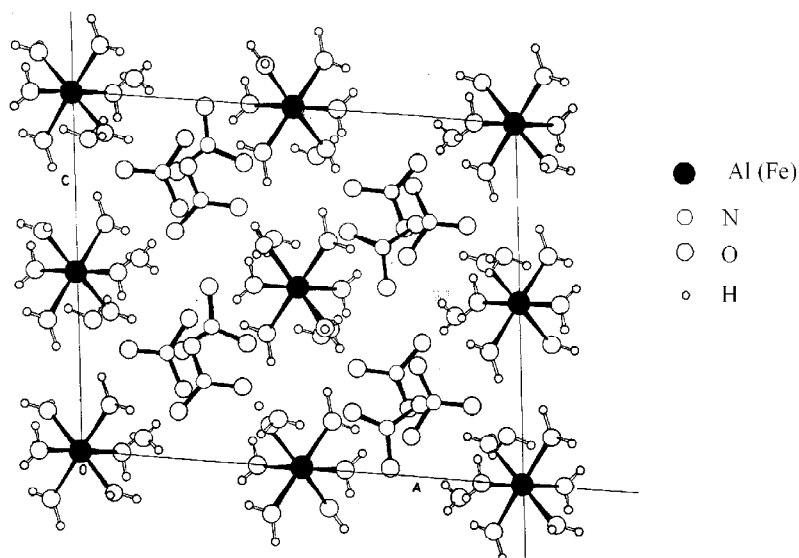


**Figure 1.** Crystal packing viewed along  $b$  axis.

It is known that magnetic ions in crystals are exposed to the influence of the crystal surrounding (named "ligand" or "crystal" field). The crystal field can change the magnetic properties of ions with respect to free ion properties. The systems that contain isolated magnetic ions are close to ideal paramagnetic substances and they are very convenient for the study of the crystal field effect. The absence of magnetic interaction between ions gives an opportunity to observe purely the crystal field effect. Magnetic properties of Cr(III) and Fe(III) hexaaqua-nitrate-trihydrate have been recently studied [6, 7]. Deviation of these materials from the Curie-Weiss law has been explained as a consequence of both the zero-field splitting and temperature independent (Van-Vleck) paramagnetism.

Here we present the refinement of the crystal structure of the solid solution  $(\text{Al}_{1-x}\text{Fe}_x)(\text{H}_2\text{O})_6(\text{NO}_3)_3 \cdot 3\text{H}_2\text{O}$  with  $x = 0.5$  and magnetic properties of solid solutions with  $x = 0.15; 0.20; 0.25; 0.50; 0.75$ .

## 2. Experimental details

Investigated solid solutions  $(\text{Al}_{1-x}\text{Fe}_x)(\text{H}_2\text{O})_6(\text{NO}_3)_3 \cdot 3\text{H}_2\text{O}$  were obtained by slow crystallization at room temperature and atmospheric pressure from saturated aqueous solutions of initial components Al(III) hexaaqua-nitrate-trihydrate (Merck 99.9 %) and Fe(III) hexaaqua-nitrate-trihydrate (Kemika 99.9 %) mixed with various molar ratios ( $x = 0.15; 0.20; 0.25; 0.50; 0.75$ ).

Single crystal sample of the solid solution  $(\text{Al}_{0.5}\text{Fe}_{0.5})(\text{H}_2\text{O})_6(\text{NO}_3)_3 \cdot 3\text{H}_2\text{O}$  was sealed in a quartz capillary since the samples are highly hygroscopic. Intensity data used for solving the crystal structure collected on an automatic four-circle diffractometer Enraf-Nonius CAD-4F using graphite-monochromatized Mo  $K_\alpha$  radiation. Reflections were recorded with Miller indices:  $-19 < h < 19$ ,  $0 < k < 13$ ,  $0 < l < 15$ , in angle range  $1.47^\circ < \theta < 29.9^\circ$  and merged to 2936 independent reflections. Data were corrected for Lorentz and polarization effects. No absorption correction was applied.

The magnetic susceptibility of the solid solutions  $(\text{Al}_{1-x}\text{Fe}_x)(\text{H}_2\text{O})_6(\text{NO}_3)_3 \cdot 3\text{H}_2\text{O}$  was measured by the Faraday method in the temperature range from 78 K to room temperature (298 K). The applied field was 1 T. Measured samples correspond to  $x = 0.15; 0.20; 0.25; 0.50; 0.75$ . Compound  $\text{Ho}_2\text{O}_3$  was used as standard.

## 3. Results and discussion

### *Crystal structure*

The crystal structure of a single crystal from solid solution ( $x = 0.5$ ) was solved by the direct method using SHELXS-97 [8]. Crystal and relevant X-ray data are given in Table 1. The Patterson synthesis confirmed that heavy atoms (ions  $\text{Al}^{3+}$  or  $\text{Fe}^{3+}$ ) occupy two independent sets of special positions  $2a$  (0, 0, 0) and  $2d$  (0.5, 0, 0.5) in space group  $\text{P}2_1/\text{c}$ . The refinement of the fractional coordinates of the non-H atoms with isotropic atomic displacement parameters and occupation factors of special positions was performed by the full-matrix least-squares method on all  $\text{F}^2$  data using SHELXL-97 [9] up to the final R-factor listed in Table 1. All H atoms were located from a difference Fourier map and refined isotropically. The fractional coordinates and equivalent isotropic displacement parameters for the non-H atoms are given in Table 2, together with the occupation factors of spatial positions  $2a$  and  $2d$ .

At the beginning of refinement occupation numbers of  $\text{Al}^{3+}$  and  $\text{Fe}^{3+}$  ions in spatial positions  $2a$  and  $2d$  were coupled in order to keep stoichiometric ratio  $(\text{Al}_{0.50}\text{Fe}_{0.5})(\text{H}_2\text{O})_6(\text{NO}_3)_3 \cdot 3\text{H}_2\text{O}$ . In the final step of refinement they were refined for each position separately. During the final step occupation factors of  $\text{Al}^{3+}$  and  $\text{Fe}^{3+}$  ions in special positions  $2a$  and  $2d$  were correlated to 0.5 for each position, due to symmetry. Thus, found stoichiometry was  $(\text{Al}_{0.68}\text{Fe}_{0.32})(\text{H}_2\text{O})_6(\text{NO}_3)_3 \cdot 3\text{H}_2\text{O}$ . The final cation distribution in special positions  $\text{sof}(\text{Fe}1) = 0.074(2)$ ,  $\text{sof}(\text{Fe}2) = 0.246(3)$  shows an expressed preferential occupation of special position  $2d$  by  $\text{Fe}^{3+}$  ions.

Octahedral volumes in special positions were analyzed. The results given in Table 3 show the existence of larger octahedral void in special position  $2d$  in crystal structure of both initial components [4, 5]. This fact explained the obtained result of cation distribution which was to be expected due to large difference in the ionic radii of  $\text{Al}^{3+}$  (0.57 Å) and  $\text{Fe}^{3+}$  (0.67 Å). Iron with bigger ionic radii "prefers" to occupy position with larger octahedral void.

**Table 1.** Crystal and relevant X-ray data.

Empirical formula	$(\text{Al}_{0.5}\text{Fe}_{0.5})(\text{NO}_3)_3 \cdot 9\text{H}_2\text{O}$
Formula weight	$M_r = 389.56$ [g/mol]
Wavelength	$\lambda = 0.71070$ [Å] (Mo $K_\alpha$ radiation)
Temperature	$T = 293(2)$ [K]
Crystal system	Monoclinic
Space group	$P2_1/c$
Unit cell dimensions	$a = 13.926(10)$ [Å] $b = 9.641(3)$ [Å] $c = 10.986(7)$ [Å] $\beta = 95.46(6)$ [°]
Volume	$V = 1468(2)$ [Å <sup>3</sup> ]
Number of asymmetric units per cell	$Z = 4$
Density (calculated)	$D_x = 1762$ [kg/m <sup>3</sup> ]
Density (measured)	$D_m = 1757$ [kg/m <sup>3</sup> ]
Absorption coefficient	$\mu = 0.686$ [mm <sup>-1</sup> ]
F (000)	798
Crystal size	$0.25 \times 0.30 \times 0.80$ [mm]
Theta range for data collection	$\theta = 1.47 - 29.9$ [°]
Habit	Plate
Color	Violet
Index range	$h = -19 \rightarrow 19$ $k = 0 \rightarrow 13$ $l = 0 \rightarrow 15$
Enraf-Nonius CAD-4 diffractometer	$\omega/2\theta$ scans
Reflections collected	3094
Independent reflections	2936 $R_{int} = 0.0335$
Refinement method	Full-matrix least-squares on $F^2$
Quantity minimized	$\sum w(F_o - F_c)^2$
Extinction coefficient	0.000(2)
Data/ restraints/ parameters	2936/ 12/ 277
Final $R$ indices $I > 2\theta(I)$	$R1 = 0.0477$ $wR2 = 0.1280$
$R$ indices (all data)	$R1 = 0.0507$ $wR2 = 0.1314$
Goodness of fit	1.045
Largest difference peak and hole	0.757 -0.775 [eÅ <sup>-3</sup> ]

Table 4 shows geometry of octahedra (bond lengths and angles) positioned in the special positions  $2a$  and  $2d$  for the solid solution with  $x = 0.32$  together with the same values for initial components Al(III) hexaaqua-nitrate-trihydrate ( $x = 0$ ) and Fe(III) hexaaqua-nitrate-trihydrate ( $x = 1$ ). Analyzing values given in Table 4, one can notice the change of the central metal ion – oxygen bond lengths depending on surrounding. It is evident that increasing of iron contents induces increase of bond lengths in octahedra. However, bond length increase is not the same in octahedron 1 and 2. Higher increment of the bond length in octahedron 2 is the result of the expressed preferential occupation of the special position  $2d$  by  $\text{Fe}^{3+}$  ions.

**Table 2.** Fractional coordinates, equivalent isotropic displacement parameters ( $U_{eq}$  [ $\text{\AA}^2$ ]) and occupation factors (sof) for the non-H atoms.

atom	site	$x$	$y$	$z$	$U_{eq}$	sof
Fe1	2a	0.00000	0.00000	0.00000	0.0196(3)	0.074(2)
Al1	2a	0.00000	0.00000	0.00000	0.0196(3)	0.426(2)
Fe2	2d	0.50000	0.00000	0.50000	0.0222(2)	0.246(3)
Al2	2d	0.50000	0.00000	0.50000	0.0221(2)	0.254(3)
N1	4e	0.7160(1)	-0.7132(2)	0.2796(2)	0.0302(4)	
N2	4e	0.7991(1)	-0.3115(2)	0.2082(2)	0.0268(4)	
N3	4e	0.3063(1)	-0.5092(2)	0.3730(2)	0.0295(4)	
O11	4e	0.7438(1)	-0.6617(2)	0.1844(2)	0.0431(5)	
O12	4e	0.6289(1)	-0.7379(2)	0.2856(2)	0.0482(5)	
O13	4e	0.7759(1)	-0.7421(2)	0.3683(2)	0.0384(4)	
O21	4e	0.7461(1)	-0.3136(2)	0.1073(2)	0.0341(4)	
O22	4e	0.8867(1)	-0.2856(2)	0.2064(2)	0.0391(5)	
O23	4e	0.7636(1)	-0.3341(2)	0.3054(2)	0.0402(5)	
O31	4e	0.2320(1)	-0.4962(2)	0.2999(2)	0.0409(5)	
O32	4e	0.3014(2)	-0.4856(2)	0.4828(2)	0.0510(6)	
O33	4e	0.3846(1)	-0.5469(2)	0.3362(2)	0.0425(5)	
OW1	4e	0.0335(1)	-0.1210(2)	0.3702(2)	0.0327(4)	
OW2	4e	0.5500(2)	-0.3879(2)	0.3709(2)	0.0369(4)	
OW3	4e	0.8563(2)	-0.0256(2)	0.4510(2)	0.0413(5)	
OW11	4e	-0.0933(1)	-0.1431(2)	-0.0050(2)	0.0271(4)	
OW12	4e	-0.0724(1)	0.1060(2)	0.1050(2)	0.0287(4)	
OW13	4e	0.0668(1)	-0.0849(2)	0.1375(2)	0.0288(4)	
OW21	4e	0.5703(1)	-0.1128(2)	0.3910(2)	0.0357(4)	
OW22	4e	0.4014(1)	-0.1424(2)	0.4990(2)	0.0366(4)	
OW23	4e	0.4291(4)	0.0927(2)	0.3655(2)	0.0330(4)	

**Table 3.** Octahedral volumes in special positions  $2a$  and  $2d$  vs. iron contents.

$x$	$V_a$ [ $\text{\AA}^3$ ]	$V_d$ [ $\text{\AA}^3$ ]
0	8.80(2)	8.83(2)
0.32	9.03(2)	9.67(2)
1	10.38(3)	10.56(3)

*Magnetic measurements*

Crystallographic structure influences the magnetic properties of investigated solid solutions. Crystallographic data manifest an important ratio of one transition metal ion per 39 other atoms, implying that the compound is highly diluted from the point of view of magnetism, and also that due to large values of unit cell parameters, metal ions are mutually widely separated by a large number of diamagnetic atoms, so most probably they do not interact directly, i.e. they are in a paramagnetic phase.

**Table 4.** Selected bond lengths [Å] and angles [°] for  $(\text{Al}_{1-x}\text{Fe}_x)(\text{H}_2\text{O})_6(\text{NO}_3)_3 \cdot 3\text{H}_2\text{O}$ .

Octahedron 1 (special position $2a$ )				
$x$	0	0.074(2)	1	
M1-OW11	1.878(2)	1.892(2)	1.986(3)	
M1-OW12	1.880(2)	1.900(2)	1.985(3)	
M1-OW13	1.870(2)	1.884(2)	1.974(3)	
OW11-M1-OW12	90.2(1)	90.39(9)	89.8(1)	
OW11-M1-OW13	89.6(1)	89.53(9)	89.1(1)	
OW12-M1-OW13	89.8(1)	89.82(9)	90.0(1)	
Octahedron 2 (special position $2d$ )				
$x$	0	0.246(3)	1	
M2-OW21	1.892(3)	1.949(2)	1.992(3)	
M2-OW22	1.881(2)	1.941(2)	2.014(3)	
M2-OW23	1.862(2)	1.918(2)	1.966(3)	
OW21-M2-OW22	90.1(1)	89.9(10)	90.1(1)	
OW21-M1-OW23	91.9(1)	92.21(10)	89.0(1)	
OW22-M2-OW23	90.5(1)	90.77(10)	87.8(1)	

The crystal field can change the magnetic properties of transition metal ions with respect to free ion properties. In complex compounds the degeneracy of the  $d$  orbitals will be partially removed by the effects of the electric field produced by the ligand. If the ligand field is weak, energy separation between multiples is small and electrons fill orbitals according to Hund's rule of maximum multiplicity, thus producing high-spin state. However, if the field is strong, energy separation between multiples may become larger than energy of Coulomb interaction between  $d$  electrons. In this case electrons first go into lower energy multiple thus producing low-spin state.

$\text{Al}^{3+}$  free ions have electronic configuration  $1s^2 2s^2 2p^6$ , without unpaired electrons, and have effect only on diamagnetism.

$\text{Fe}^{3+}$  free ions have electronic configuration  $d^5$ , ground state is  ${}^6S_{5/2}$  ( $L = 0$ ). Two limiting cases of spin-only magnetic moments values for complex  $\text{Fe}^{3+}$  ion in octahedral crystal field are given below [10]. A  $\text{Fe}^{3+}$  ion in an ideal octahedral coordination is high-spin configured  $t_{2g}^3 e_g^2$  with spin only magnetic moment  $5.92 \mu_B$  ( $S = 5/2$ ). Otherwise, when the octahedron is axially distorted the twofold degeneracy orbital  $e_g$  will be lifted due to Jahn-Teller effect. Electrons are confined in low-spin state with configuration  $t_{2g}^5$  and spin only magnetic moment  $1.73 \mu_B$  ( $S = 1/2$ ).

Temperature dependence of uncorrected values of inverse mass magnetic susceptibility for all samples is depicted in Figure 2. The magnetic susceptibility measurement data are converted into gram-ion susceptibility data and corrected for the diamagnetic contribution using ionic diamagnetic values [11]. Inverse gram-ion susceptibility data in function of temperature for sample  $x = 0.75$  are shown on Figure 3. These inverse gram-ion susceptibility data were fitted to Curie-Weiss law:

$$\frac{1}{\chi} = \frac{T - \theta_0}{C_M}, \quad (1)$$

where  $\chi$  is the gram-ion magnetic susceptibility,  $C_M$  is Curie molar constant,  $\theta_0$  Curie-Weiss paramagnetic temperature and  $T$  is absolute temperature. In this procedure, Curie

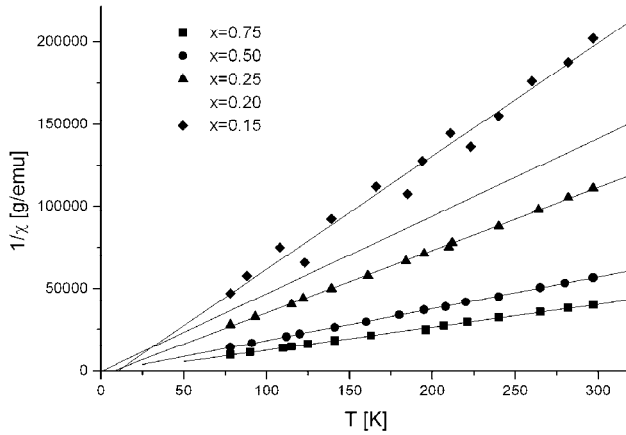


**Figure 2.** Uncorrected values of inverse mass susceptibility of solid solutions  $(\text{Al}_{1-x}\text{Fe}_x)(\text{H}_2\text{O})_6(\text{NO}_3)_3 \cdot 3\text{H}_2\text{O}$ .

concentration was found. This could be explained by the fact that layers formed by the octahedra could be divided into layers containing only  $2d$  spatial positions and layers with ratio of 4:1 for spatial positions  $2a$  and  $2d$  respectively. The effect of preferential occupation of  $\text{Fe}^{3+}$  ions in spatial position  $2d$  does not influence magnetic properties at lower concentration of magnetic ions. A certain clusterisation of  $\text{Fe}^{3+}$  ions in layers contain only  $2d$  positions is probably present at higher concentrations of magnetic ions thus producing some local ordering and decreasing of Curie-Weiss paramagnetic temperature.

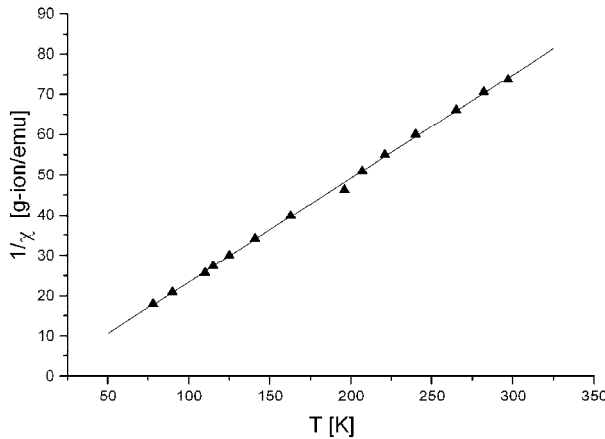


**Figure 3.** Temperature dependence of the inverse gram-ion susceptibility for sample with  $x = 0.75$ .

Calculated values for effective magnetic moments for  $\text{Fe}^{3+}$  ions for all samples are given in Table 5. They agree with spin only value for  $\text{Fe}^{3+}$  ions in high-spin state. The small difference between the observed and theoretical value of effective magnetic moments of  $\text{Fe}^{3+}$  ions may be due to crystal field effects as has been observed in many other solids [13, 14].

molar constant and Curie-Weiss paramagnetic temperature were treated as fitting parameters. The  $C_M$  was obtained from the slopes of the lines and  $\theta_0$  by extrapolation to  $T$  axis. Calculated values for  $C_M$  and  $\theta_0$  are given in Table 5. The negative values of Curie-Weiss temperature indicate that there is antiferromagnetic interaction in the samples  $x = 0.5$  and  $x = 0.75$ , however, according to [7], this is not observed for  $\text{Fe}(\text{III})$  hexaaquanitrate-trihydrate in the curve of magnetic susceptibility down to 4 K. The increase of  $\theta_0$  at lower

Analyzing the results of calculations and magnetic measurement data we may conclude that the gram-ion susceptibilities are almost independent on iron contents, which means that direct interaction between magnetic ions is absent. Temperature dependence of the inverse gram-ion susceptibility shows that all samples are in paramagnetic phase in whole temperature range.

The effective magnetic moments for  $\text{Fe}^{3+}$  ions in octahedral surrounding of water molecules are calculated using relation [12]:

$$\mu_{eff} = \sqrt{8C_M}. \quad (2)$$

**Table 5.** Calculated values for Curie molar constants, Curie-Weiss paramagnetic temperature and effective magnetic moments of  $\text{Fe}^{3+}$  ions in solid solutions  $(\text{Al}_{1-x}\text{Fe}_x)(\text{H}_2\text{O})_6(\text{NO}_3)_3 \cdot 3\text{H}_2\text{O}$ .

$x$	$\theta_0$ [K]	$C_M$ [emuK/g-ion]	$\mu_{eff}$ [ $\mu_B$ ]
0.15	2(7)	4.2(3)	5.9(2)
0.20	3(3)	4.3(1)	5.90(9)
0.25	0.4(8)	4.40(3)	5.93(3)
0.50	-2.5(3)	4.17(1)	5.78(2)
0.75	-7(1)	4.02(3)	5.67(3)

#### 4. Conclusion

The structure refinement confirmed that solid solutions  $(\text{Al}_{1-x}\text{Fe}_x)(\text{H}_2\text{O})_6(\text{NO}_3)_3 \cdot 3\text{H}_2\text{O}$  are isostructural with initial components Al(III) and Fe(III) hexaaqua-nitrate-trihydrates which crystallize in centrosymmetric space group  $\text{P}2_1/\text{c}$ . Metal ions are surrounded within regular octahedral crystal field by water molecules. Final cation distribution in special positions for  $\text{Fe}^{3+}$  ions (0.074(2) for 1 and 0.246(3) for 2) shows expressed preferential occupations of special position  $2d$ .

Temperature dependence of the inverse gram-ion susceptibility is almost independent on iron contents. It shows that all samples are in paramagnetic phase in whole measured temperature range.

Calculated values of effective magnetic moment agree, within error limit, with spin only magnetic moment for free  $\text{Fe}^{3+}$  ion in high-spin state.

Such values of the effective magnetic moment indicate that iron ion being octahedrally surrounded by water molecules is under weak influence of crystal field compared to spin-orbital interaction, i.e. there are no electrons pairing and the formation of low-spin state.

#### Acknowledgments

This work was supported by Serbian Ministry of Science and Technologies under Project No. 2022 "Physical Properties of Bulk and Nanoparticled Rare Earths and Transition Metal Based Magnetic materials".

#### References

1. M. Vučinić, A. Kapor, N. Furmanova, VI Conference of the Serbian Crystallographic Society, Sokobanja, Yugoslavia, p. 34 (1997).
2. S. Rakić, A. Kapor, N. Furmanova, Z Kristallogr. NSC **213**, 449 (1998).
3. M. Vučinić, S. Rakić, A. Kapor, Proc. 4th Int. Conf. on Fundamental and Applied Aspects of Physical Chemistry, Belgrade, Yugoslavia, p. 61 (1998).
4. D. Lazar, B. Ribar, B. Prelesnik, Acta Cryst. C **47**, 2282 (1991).
5. N.J. Hair, K.J. Beattie, Inorganic Chemistry **16**, 245 (1977).

6. V Kusigerski, M. Mitrić, V. Spasojević, Proc. 5th Int. Conf. on Fundamental and Applied Aspects of Physical Chemistry, Belgrade, Yugoslavia, p. 414 (2000).
7. M. Vučinić, M. Mitrić, V. Kusigerski, A. Kapor, A. Szytula, J. Res. Phys. **29**, 79 (2002).
8. Sheldrick G. M., "SHELXS-97", University of Göttingen, Germany (1997).
9. Sheldrick G. M., "SHELXL-97", University of Göttingen, Germany (1997).
10. J. Crangle, *Solid State Magnetism*, (Edward Arnold, London, 1991).
11. Yu. V. Rakitin, V. T. Kalinnikov, *Modern Magnetochemistry*, (Nauka, St. Petersburg, 1994).
12. J. Smart, *Effective Field Theories of Magnetism*, (W. B. Saunders Company, Philadelphia London, 1966).
13. D. H. Martin, *Magnetism in Solids*, (Illete Books, London, 1967).
14. K. R. Dunbar, E. J. Schelter, B. S. Tsukerblat, S. M. Ostrovsky, V. Y. Mirovitsky, A. V. Palii, Polyhedron **22**, 2545 (2003).

## Structural Properties of Ferroelectric Liquid Crystals with 2-Alkoxypropionate Chiral Group by X-ray Diffraction

D. Ž. Obadović<sup>1</sup>, M. Garić<sup>1</sup>, A. Vajda<sup>2</sup>, A. Bubnov<sup>3</sup>, M. Kašpar<sup>3</sup>, and V. Hamplová<sup>3</sup>

<sup>1</sup>*Department of Physics, Faculty of Sciences, University of Novi Sad,*

*Trg D. Obradovića 4, Novi Sad, Serbia and Montenegro;*

<sup>2</sup>*Research Institute for Solid State Physics and Optics of the Hungarian Academy of Sciences, H-1525 Budapest, P.O. Box 49, Hungary;*

<sup>3</sup>*Institute of Physics, Academy of Sciences of the Czech Republic, Na Slovance 2, 182 21 Prague, Czech Republic*

Received: September 27, 2004

### Abstract

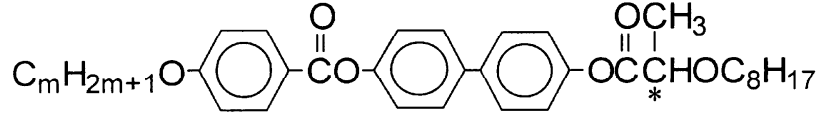
The structural properties of the non-substituted ferroelectric liquid crystals with 2- alkoxypropionate chiral group with one chiral centre are studied. In these compounds, the blue phase, the chiral nematic N\* phase, the ferroelectric smectic C\* phase and a low temperature liquid crystalline SmX phase have been detected. All substances exhibit a broad temperature range of the SmC\* phase characterized by high values of the spontaneous polarization. The substances have been studied by Differential Scanning Calorimetry (DSC) and optical microscopy. Using detailed structural investigation by X-ray diffraction method on non-oriented samples, a low temperature crystalline SmX phase was identified as the hexatic SmB phase. According to the X-ray diffraction data, the molecular parameters have been calculated: the layer spacing in the SmC\* and SmB phases and the average intermolecular distances between neighbouring parallel molecules in all investigated mesophases. Temperature dependence of the layer spacing,  $d$ , is presented.

*Key words:* Ferroelectric liquid crystal, spontaneous polarization, phase transition, X-ray diffraction, molecular parameters

### 1. Introduction

The peculiarities of the molecular arrangement in mesophases of the ferroelectric liquid crystalline materials have been intensively studied by various authors<sup>1-2</sup>. A lot of efforts have been directed to obtain polar liquid crystalline materials that can respond application demands for electro-optical devices.

In these work we present a continuation of the studies on the three homologous series of ferroelectric liquid crystals with 2-alkoxypropionate chiral group and one chiral centre denoted. Synthesis of the studied compounds and some basic properties were presented earlier<sup>3-5</sup>. General formula of the studied compounds is:



denoted as H  $m/8$ , where  $m = 6, 8, 9$ . Sequence of phases and phase transition temperatures of investigated substances are shown in Table 1. These compounds show the blue phase BP, the chiral nematic N\* phase, the ferroelectric smectic SmC\* phase and a low temperature liquid crystalline SmX phase have been detected.

**Table 1.** Sequence of phases, phase transition temperatures [°C] and values of spontaneous polarisation  $P_s$  [nCcm<sup>-2</sup>] at temperature 20 K below the transition to the SmC\* phase. All these data were obtained on cooling from the isotropic phase.

(• the phase exists; – the phase does not exist).

	SmX	SmC*	N*	BP	Iso	$P_s$
H 6/8	• 67	• 122	• 138	• 139	•	103
H 8/8	• 58	• 128	• 134	–	•	105
H 9/8	• 57	• 129	• 130	• 133	•	95

The aim of this study is to identify a low temperature liquid crystalline SmX phase by X-ray diffraction method<sup>6</sup> and to determine the intermolecular distances and layer spacing in the mesophases presented. The layer spacing ( $d$ ), and the average intermolecular distance between the long axes of neighbouring parallel molecules ( $D$ ) have been determined for all the phases (except SmB) using the Bragg law:  $n\lambda = 2d\sin\theta$ , where  $d$  and  $D$  were calculated from the position of the small angle and large angle diffraction peaks, respectively. But in the hexatic SmB phase, the average intermolecular distance between the long axes of neighbouring parallel molecules, is the function of  $D$ <sup>7</sup>, and can be calculated as  $b = 2D/3^{1/2}$ .

## 2. Experimental details

Optical study was performed using polarization microscope Amplival Pol-U with a Boetius heating/cooling stage. The heating rate was 4°C/min, the cooling rate was not controlled.

Non-oriented samples were investigated by the X-ray diffraction in a transmission geometry using conventional powder diffractometer, Seifert V-14, CuK $\alpha$  radiation at 0.154 nm, with an automated high temperature kit Paar HTK-10.

The values of spontaneous polarisation ( $P_s$ ) have been evaluated from  $P(E)$  hysteresis loop detected during  $P_s$  switching in a.c. electric field  $E$  of frequency 60 Hz on 25  $\mu$ m thick planar samples. The  $P_s$  measurements were done on cooling.

The values of the spontaneous tilt angle ( $\theta_s$ ) have been determined optically from the difference between extinction positions at crossed polarisers under opposite d.c. electric fields  $\pm 40$  kVcm<sup>-1</sup>. Well aligned samples were used for  $\theta_s$  measurements. The  $\theta_s$  measurements were done on cooling.

## 3. Results and discussion

X-ray diffraction studies were carried out on all the investigated compounds and the

examples of the X-ray diagrams of non-oriented sample as a function of the temperature are shown in Figure 1. Molecular parameters substituted compounds for all observed phases at a fixed temperature  $T$  [°C] are shown in Table 2, namely, angles corresponding to the reflection peaks  $2\Theta$  [degrees], effective layer thickness  $d$  [Å] (error of measurements  $\delta_d$  was about  $\pm 0.04$  Å), average repeat distance  $D$  [Å] (error of measurements  $\delta_D$  was about  $\pm 0.002$  Å) and intermolecular distance in SmB phase  $b$  [Å]. In the BP and N\* phase,  $d$  equals approximately the length of the molecule.

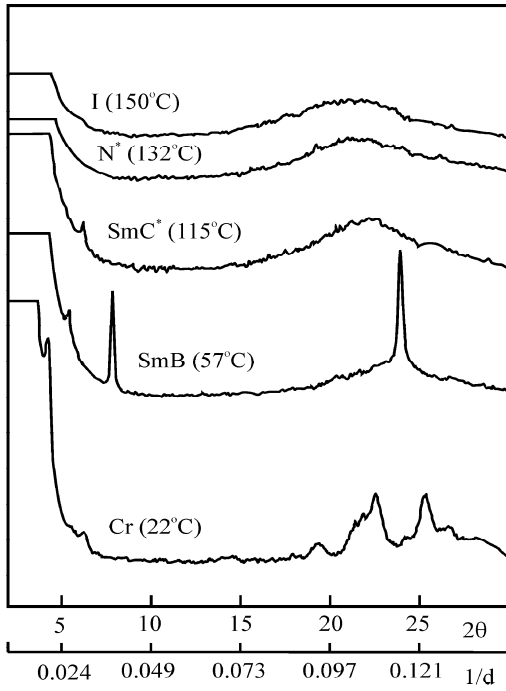


**Figure 1.** X-ray diffraction profiles for H 8/8 for all investigated phases.

In the case of H 8/8 (see Fig. 1(a)) the enantiotropic SmC\* and the N\* phases were determined. The analysis of X-ray diagrams in the SmC\* phase shows the presence of the reflections at small angles ( $2\theta \sim 6.1^\circ$ ), indicating the appearance of the layer structure, besides the diffuse outer scattering ( $2\theta \sim 22.2^\circ$ ) is presented corresponding to average intermolecular distance  $D$ . The calculation of effective layer thickness  $d$ , gives the value of 16.87 Å, and 4.66 Å for the intermolecular distance  $D$  at the temperature of 115°C. If the temperature decreases, the intensity of the small angle peak increases and the effective layer thickness decreases (see Fig. 2(a)).

In the case of the blue phase and the chiral nematic phase some low angle peaks ( $2\theta \sim 3 - 6^\circ$ ) depending on the compound, can be noticed. These peaks correspond to the long spacing distance approximately equal to the length of the molecule ( $d \sim l$ ), which slightly decreases with the temperature increase<sup>8</sup>.

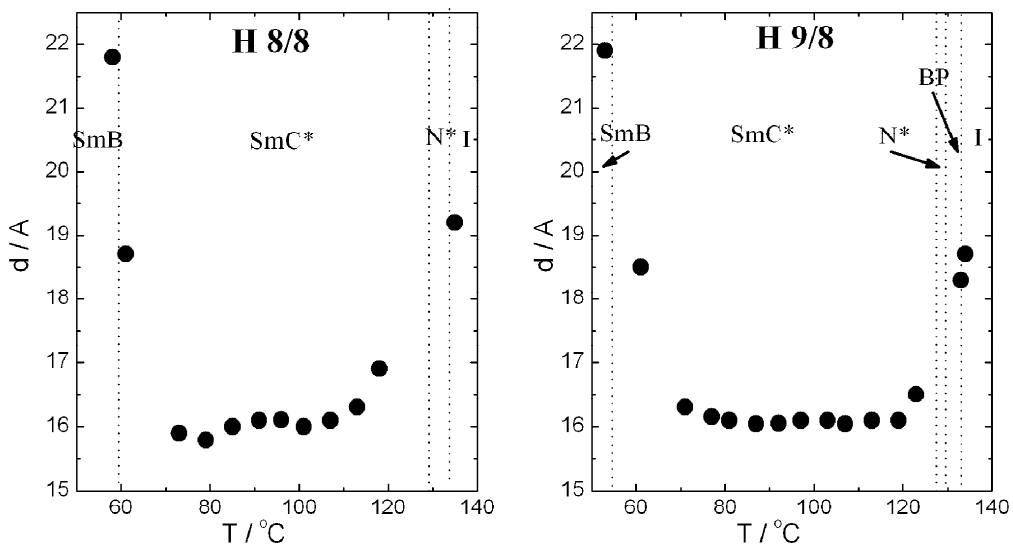


**Figure 2.** Temperature dependences of the layer spacing for H 8/8 and H 9/8 compounds.

For the compound H 8/8, at the temperature of 57°C, two peaks ( $2\theta \sim 4.75^\circ$  and  $7.2^\circ$ ) appear at the position of the small angle reflection, corresponding to short spacing distance. Moreover, an additional strong peak ( $2\theta \sim 23.2^\circ$ ) arises. Such a strong peak corresponds to the hexagonal packing of the centres of mass of the molecules along smectic layers and characterizes SmB phase. Hence the unidentified SmX phase was attributed to the hexatic SmB phase.

For this compound, the SmB phase appears on cooling in a wide temperature range 58 – 50°C, when the first signs of crystallization appear (see Fig. 1(a)). The SmC\*→SmB phase transition is also connected with a jump of the layer thickness in all investigated compounds (see Table 2).

**Table 2.** Molecular parameters for all investigated compounds.

	phase	$T$ [°C]	$2\Theta$ [°]	$d$ [Å]	$D$ [Å]	$b$ [Å]
H 6/8	I	160.0	20.00	–	5.169	–
	BP	138.5	3.30	31.21	–	–
			21.00	–	4.925	–
	N*	130.0	21.50	–	4.805	–
	SmC*	102.0	6.30	16.30	–	–
21.90			–	4.716	–	
H 8/8	I	150.0	20.75	–	4.984	–
	N*	132.0	21.8	–	4.879	–
	SmC*	115.0	6.10	16.87	–	–
			22.2	–	4.662	–
	SmB	57.0	4.75	21.66	–	–
7.20			14.29	–	–	
23.2			–	4.464	5.155	
H 9/8	I	150.0	21.20	–	4.869	–
	BP	131.0	6.25	19.42	–	–
			21.8	–	4.791	–
	N*	129.5	5.55	18.50	–	–
			21.8	–	4.737	–
SmC*	120.0	5.65	18.17	–	–	
		21.90	–	4.716	–	
		SmB	54.0	4.70	21.85	–
7.10	14.47			–	–	
23.3	–			4.436	5.122	

The calculation of the average intermolecular distance between long axes of the neighbouring parallel molecules indicates the increase of the molecule packing density (or the mean lateral intermolecular spacing), giving for the compound H 8/8 values of  $D$  of 4.98 Å, 4.87 Å and 4.66 Å for the isotropic, chiral nematic, and SmC\* phases, respectively. In Figure 2, temperature dependence of the layer spacing,  $d$ , for the compounds of H 8/8 and H 9/8 is shown. In the SmC\* phase, the layer spacing values decrease on cooling. At the SmC\*→SmB phase transition temperature, the stretching of the aliphatic molecular chains and increased orientational order of the molecular long axes are the causes of the increasing  $d$  value. At the SmC\*→N\* phase transition temperature,  $d$  increases, meaning

that a trend appears of the molecular axes to take the position parallel with the director, and the angle between the molecular axes and the director vanishes.

In Figure 3, microphotograph of the cholesteric texture with oily streaks typical for the studied compounds is shown. Microphotograph of the tilted ferroelectric SmC\* phase texture is shown in Figure 4. Non-regular dechiralisation lines indicate the partly unwound helical structure of the phase.

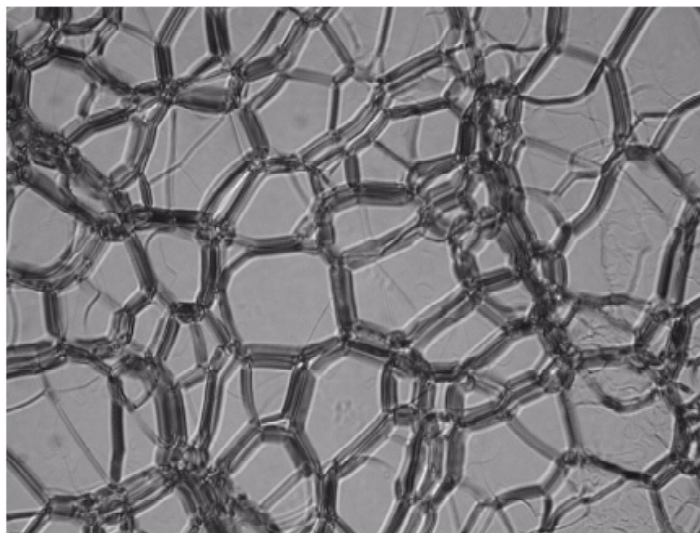


**Figure 3.** Microphotograph of the cholesteric N\* phase texture with oily streaks between crossed polarisers for the compound H 8/8 taken at 130°C. The width of the photo is about 150  $\mu\text{m}$ .

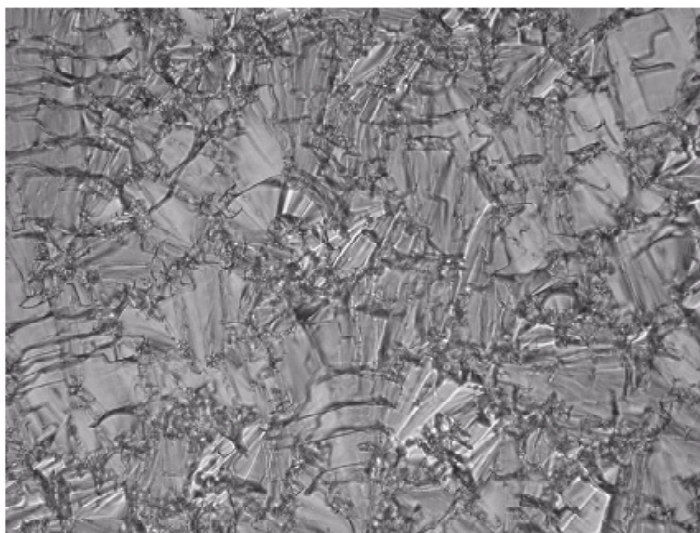


**Figure 4.** Microphotograph of the ferroelectric SmC\* phase texture between crossed polarisers for the compound H 8/8 taken at 100°C. The width of the photo is about 150  $\mu\text{m}$ .

All substances exhibit a broad temperature range of the ferroelectric SmC\* phase. For the material H 8/8, the temperature dependences of the spontaneous polarization and spontaneous tilt angle, typical for the materials studied here, are shown in Figure

5. The studied materials are characterized by relatively high values of the spontaneous polarization of about  $100 \text{ nC/cm}^2$  at saturation (see Table 1 and Figure 5 for H 8/8). At the  $\text{N}^* \rightarrow \text{SmC}^*$  phase transition temperature  $T_c$ , a finite jump up in  $P_s$  and  $\theta_s$  was found, which is typical for the first order phase transition. The values of the spontaneous tilt angle, being temperature independent, were within interval of  $38 - 43^\circ$  for all these compounds (see Figure 5 for H 8/8). The slight increase in the values of the spontaneous polarization and spontaneous tilt angle, just below the phase transition temperature, can be explained by the phase coexistence region of a several degrees broad.

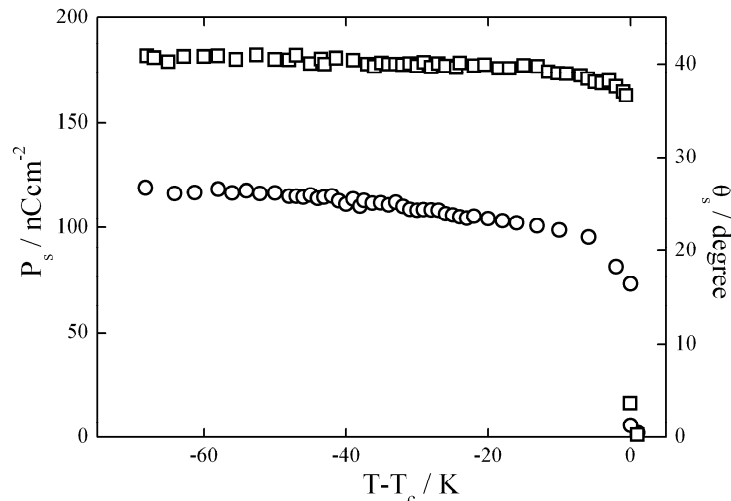


**Figure 5.** Temperature dependences of the spontaneous polarization  $P_s$  (circles) and of the spontaneous tilt angle  $\theta_s$  (squares) for H 8/8 ( $T_c$  is the temperature of the  $\text{N}^* \rightarrow \text{SmC}^*$  phase transition).

#### 4. Conclusion

The results of the study on the homologue series of ferroelectrics liquid crystals with 2-alkoxypropionate chiral group, with one chiral centre and without any lateral group have been presented. All substances exhibit a broad temperature range of the  $\text{SmC}^*$  phase characterized by high values of the spontaneous polarization of about  $100 \text{ nC/cm}^2$  at saturation. At the  $\text{N}^* \rightarrow \text{SmC}^*$  phase transition temperature  $T_c$ , a finite jump up in  $P_s$  and  $\theta_s$  was found, which is characteristic for the first order phase transition. The values of the spontaneous tilt angle, being temperature independent, were within interval of  $38 - 43^\circ$  for all these compounds.

On the base of X-ray diffraction data on the crystalline powder of non-oriented samples, the low temperature liquid crystalline  $\text{SmX}$  phase was identified as the hexatic  $\text{SmB}$  phase. The molecular parameters have been determined, namely, the average intermolecular distance,  $D$ , and long spacing distance,  $d$ , approximately equal to the length of the molecule ( $d \sim l$ ) in the BP and  $\text{N}^*$  phase or the interlayer spacing, in the  $\text{SmC}^*$  and  $\text{SmB}$  phases.

Intermolecular distance  $D$  and the long spacing distance  $d$ , increase with the temperature increase, for all investigated compounds in the case of  $\text{SmC}^* \rightarrow \text{I}$  phase transitions. At the temperature of the  $\text{SmC}^* \rightarrow \text{SmB}$  phase transition, the stretching of the aliphatic mole-

cular chains and increased orientational order of the molecular long axes are the causes of the jump of  $d$  values (Table 2). At the  $\text{SmC}^* \rightarrow \text{N}^*$  phase transition temperature for H 9/8,  $d$  increases, meaning that a trend appears of the molecular axes to take the position parallel with director, and the angle between molecular axes and director vanishes.

## Acknowledgments

This work was supported in part by the following grants: research Grant No. 1578 from the Ministry of Science, Technologies and Development of the Republic of Serbia, special financial Grant from VANU of the project "Natural and spiritual resource of Vojvodina", Grants No. 202/03/P011, 202/02/0840 from the Grant Agency of the Czech Republic, European Project COST D14 WG15, Hungarian Research Grant OTKA T032667.

## References

1. R. Dabrowski, J. Szulc, and B. Sosnovska, *Mol. Cryst. Liq. Cryst.* **215**, 215 (1991).
2. A. Fukuda, Y. Takanishi, T. Isozaki, K. Ishikawa, and H. Takezoe, *J. Mater. Chem.* **4**, 997 (1994).
3. M. Kašpar, M. Glogarová, V. Hamplová, H. Severnyák, and S. A. Pakhomov, *Ferroelectrics* **148**, 103 (1993).
4. M. Kašpar, E. Gorecka, H. Severnyák, V. Hamplová, M. Glogarová, and S. A. Pakhomov, *Liquid Crystals* **19**, 589 (1995).
5. M. Kašpar, V. Hamplová, S. A. Pakhomov, I. Stibor, H. Sverenyák, A. M. Bubnov, M. Glogarová, and P. Vanek, *Liquid Crystals* **22**, 557 (1997).
6. D. Ž. Obadović, L. Bata, T. Thot-Katona, A. Bota, K. Fodor-Csorba, A. Vajda, and M. Stančić, *Mol. Cryst. Liq. Cryst.* **303**, 85 (1997).
7. J. M. Seddon, In D. Demus, J. Goodby, G. W. Gray, H. W. Spiess, V. Vill, eds. *Handbook of Liquid Crystals*, Vol. 1, p. 635 (Weinheim: WILEY-VCH Verlag GmbH, 1998).
8. A. de Vries, *Mol. Cryst. Liq. Cryst.* **20**, 2119 (1973).

## Three-Particle Interactions with a Possible Application to Cold Fusion

Ljubisav Novaković

*Faculty of Science, P. O. Box 60, 34000 Kragujevac, Serbia and Montenegro*

*e-mail: ljnovak@kg.ac.yu*

Received: April 19, 2004

### Abstract

By starting from very general assumptions we have studied a cold - fusion research programme and came to the conclusion that it can be established on three physically independent approaches. On the one hand this programme can be described classically, while on the other hand it certainly has a quantum - mechanical origin. However, all numerical results, if obtained by consistent use of both the classical as well as quantum - mechanical equations of motion, may be tested experimentally only with the help of yet another approach which calls for the methods of electrodynamics. Equations of motion will be applied to a specific geometric - structural model of three - particle clusters,  $e_1^- p(d) e_2^-$ . Here the heavy particle (proton, deuteron) is assumed to perform an orbital motion about the axis which joins the motionless (or almost motionless)  $e_1, e_2$  electrons. Furthermore, we have directed the present study towards metallic lattices of the palladium group to see just how the heavy particle can experience such an acrobatic dynamics. For this reason we considered the action of a time - dependent electric field combined with a constant magnetic induction field (known as the *Lorentz force*), presumably materialized within a palladium lattice structure, to see a possible physical mechanism by which a particular three - particle cluster may pass from one stationary state to the other.

*Key words:* Cold-fusion channels, Lorentz force, critical conditions.

### 1. Introduction

Recently observed "excess heat", in a cold-fusion research programme, requires a more fundamental approach to the problem of the binding energies of a non-nuclear origin. Here obviously we deal with a research field which is somewhere between atomic physics, on one side, and nuclear physics, on the other. Energies and separation distances in atomic physics have orders of magnitude 10 eV,  $10^{-8}$  cm, respectively, while these quantities in nuclear physics have orders of magnitude  $10^6$  eV,  $10^{-13}$  cm, respectively.

In an ordinary high - temperature plasma the protons must be accelerated up to the energies 1 MeV whose actual speeds are in the vicinity  $10^9$  cm s $^{-1}$ . This is a considerable fraction in comparison with the speed of light. However, a fundamental chemical reaction

taking place in a cold-fusion process, if it starts at all, is expressed by a dissociation of heavy water molecules, in the first stage, into the following elementary constituents,



where  $D, O$  stand for deuterium and oxygen, respectively. Here  $D^+$  is just a deuteron, while  $O^{2(-)}$  designates an oxygen ion with the three lowest electron shells being filled up:  $1s^2 2s^2 2p^6$ , making a magic atomic structure.

Similar chemical reactions hold for the dissociation of the molecular entities  $HDO$  and  $H_2O$ .

What is more important, a technical machinery surrounding an ordinary hot plasma requires temperatures something like  $10^7$  K, or even higher, in order that the protons or deuterons penetrate into the Coulomb barrier which exists among the colliding particles. However, particles could be accelerated by using more moderate methods. There are at our disposal two competing processes which are hidden somewhere between atomic physics and nuclear physics, as follows.

- (i) We can imagine on purely theoretical grounds that the protons (deuterons) may experience, in a time - dependent electric field, a linear oscillatory motion to catch up speeds like  $v = A\omega$ , where  $A$  is an amplitude in the  $10^{-7}$  cm range,  $\omega$  is a frequency of the periodical electric field whose order of magnitude is something like  $10^{16}$  s $^{-1}$ , so that  $v$  may attain the above quoted limit.
- (ii) Alternatively, these particles, if subjected to a time - dependent electric field combined with a constant magnetic induction, may nevertheless catch up the required speeds in the form  $v = R(\omega, B_x)\omega$  by performing orbital motions, where  $R(\omega, B_x)$  designates a radius of such an orbit,  $\omega$  is an orbital frequency. If a critical condition  $m_3\omega = qB_x$  is fulfilled exactly, while  $\omega$  has some value within the  $10^7$  s $^{-1}$  frequency range and  $B_x \approx 0.1$  T, then the velocity of the orbiting heavy particle (proton, or deuteron) might tend to infinity as well as the radius of the orbiting motion. This condition may generate a large probability of a given deuteron to penetrate into the Coulomb barrier of another deuteron, so as to initiate a release of energy.

If one of the above introduced processes takes place, or both of them, we shall name it a *cold - fusion reaction*.

Having studied a two-body problem with a potential of the type  $(\alpha/r)(1 - \vec{v}_1 \cdot \vec{v}_2)$ , where  $\alpha$  is a constant while these two vectors refer to the velocities of two charged particles like electron - positron, or proton - antiproton, Barut and Craig (1993) discovered a series of very tightly bound states among the oppositely charged particles. The authors used a Bohr - Sommerfeld quantization rule to obtain almost stable tightly bound states of positive energy at very short distances which come from the magnetic interactions between the oppositely charged particles.

A similar idea was considered by Dragić *et al* (2000) in a paper where an "excess heat" in cold - fusion experiments could be related to the tightly bound states of the hydrogen atom. What is more important, these authors indicated an electromagnetic mechanism by which the heavy particle (proton, or deuteron) might materialize a motion around the motionless (or almost motionless) electrons. Although novel in atomic physics, the mentioned mechanism does not seem to be clearly specified by the non-Coulomb forces,

such as spin - orbit, or spin - spin, among the heavy as well as light particles. This idea has been independently developed by Kirkinskii and Novikov (1999) in the sense that a palladium metallic structure, through its outer and feebly bound electrons, might influence the screening of the Coulomb repulsion between the protons, or deuterons, in order to initiate a nuclear fusion. Like the previous reference, these two authors did not seem to have indicated the precise electrodynamic mechanism by which a penetration over the Coulomb barrier in an actual experiment might have taken place.

In the meantime Miles (2000) discovered a number of sensitive calorimetric methods where the excess power effect was measured through an anomalous increase of the cell temperature. In spite of the huge power effect, this author could not clearly define the exact triggering mechanism by which the internal energy has been liberated. Similar observations of the cold - fusion heat power were published by Oh (1999) and by Xiao and Li (1999). A different experimental method based on the so-called "phonon maser" was introduced by Kamada (2001). In his paper this author measured an anomalous melting of the *Al* surface which is being implanted with deuterium on the irradiation with high energy electrons in a transmission electron microscope. Having failed to find a conventional explanation of the effect, within the models of solid-state physics, this author suggested a "cold - fusion" mechanism as a possible theoretical approach. At the same time a number of papers have been published and developed new technical innovations to be used for the detection of liberated neutrons which surround the cold - fusion experiments. One of these methods is a contribution of Cisbani *et al* (2001) who developed a high - efficiency neutron detector with a large angular acceptance and low noise.

It should be emphasized that David J. Nagel (1998) published a paper *The Status of Cold Fusion* where he called for an attention aimed at the examination of the entire problem of "cold fusion" from a more exact point of view. His question is directed to many scientists who have so far expressed a serious dissatisfaction, if not disagreement, about the reports of nuclear reactions in a low - energy region. Not only for practical reasons, but also for our theoretical knowledge, we must undertake a considerable effort to explain exactly what mechanism, if any, is governing the motion of the heavy charged particles from an atomic level down to the nuclear structure - the process that seems responsible for the unusual liberation of energy. If properly conducted, such investigations, according to D. J. Nagel (1998), will supply useful information for a long - term theoretical understanding as well as technological utility.

There are of course papers, like that published by Voss (1999), which examine the very idea of having a "cold fusion" process by putting forward questions whether such a process might have anything to do with the realistic excess heat. Nevertheless, in spite of the above mentioned author's serious doubts and skepticism, the cold-fusion research still survives and keeps attracting more attention among the physicists. At the same time, this research field seems more attractive to conventional institutions and laboratories which support the idea financially.

In this work we start with the idea that some deeply bound states of three - particle systems may exist, such as  $e_1^- p e_2^-$ , or the electrically equivalent  $e_1^- d e_2^-$ , where  $p, d$  designates the proton or deuteron. Our present study is directed towards three various approaches, classical, quantum - mechanical, and electrodynamic. First, we will look at the system of three bound particles under the classical action of various Coulomb forces (attractive as well as repulsive), where the heavy particle (proton, deuteron) has an angular momentum about the axis which passes through the two motionless electrons (Section 2). Second, a

quantum - mechanical approach will be simultaneously introduced, based on a series of algebraic transformations of the operators that are associated with the kinetic and potential energies of the constituents of any three - particle cluster. These transformations end up with an eigenvalue problem where the heavy particle ( $p$ ,  $d$ ) moves in a twodimensional potential field (Sections 3, 4).

There is also an electrodynamic approach. Just how the two kinds of particle (electrons on the one side, the heavy particles on the other) behave under the action of an applied Lorentz force within a palladium metallic lattice, which might lead to the collapse of the three - particle cluster to deeply bound states, is considered in Sections 5 and 6. Critical approach to the relevant physical quantities including possible orders of magnitude (e.g. binding energies, separation distances, electric field, magnetic induction) and descending mechanism are examined in Section 7. Possible realistic prospects in an actual technical environment are discussed in Section 8.

## 2. Classical approach to the three-particle cluster by having neglected magnetic interactions among the electrons

In fact, with three particles in mind we can develop two different geometric - structural models, whose distinctions will be based solely on the electrostatic arguments. In the present section we shall neglect a possible influence of magnetic forces acting among the electrons. These forces are important in studying the tightly bound states of heavy particles ( $p$  or  $d$ ) and will be considered in Sections 6 - 8 in more detail.

- (i) There is a model where one particle stays almost still all the time while the other two are moving around, the model usually associated with the helium - atom problem. This we shall name *Model one*, which is materialized as a negative hydrogen ion  $H^-$ .
- (ii) Another model is materialized where two particles stay almost motionless all the time while the third particle is moving around their joining line, the model similar to a hydrogen molecular ion,  $H_2^+$ . This we shall name *Model two*, which is materialized as a three- particle cluster  $e^-p(d)e^-$ .

We shall consider the model under (ii) in more detail, but with the nucleus playing the role of the electron, while the electrons stay almost motionless. Here we have to introduce 9 constants of motion as a consequence of having a physical system with 9 degrees of freedom. Three degrees of freedom are associated with the centre of mass of the entire cluster, as illustrated by the point  $C$  in Figure 1. Here we have to identify

$$A_1BA_2 \Rightarrow e_1^-p(d)e_2^-.$$

Additional three degrees of freedom are associated with the identical particles  $A_1$  and  $A_2$  (a fixed separation distance  $R$ , plus the fixed  $A_1A_2$  line, making altogether three degrees of freedom).

Finally, the problem is reduced to the consideration of another set of three degrees of freedom, i. e. three constants of motion left available for the third particle. Obviously, this particle may move in a plane which is perpendicular to a line which joins  $A_1$  with  $A_2$ , so that there are two constants of motion materialized by the angular momentum of the third particle. (An angular momentum, being a vector, is defined by two elements, one scalar quantity and the direction of the vector). Lastly, the ninth constant of motion is

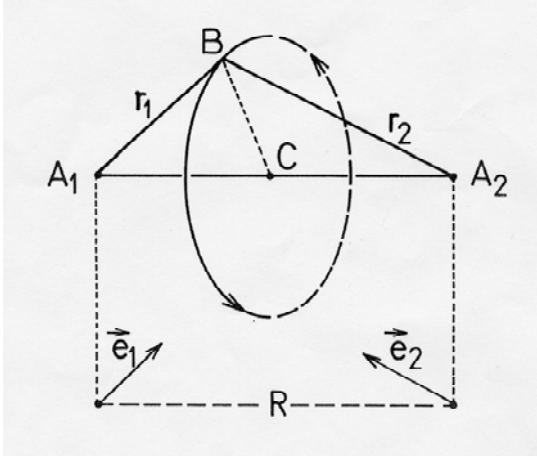


**Figure 1.** Two identical particles ( $A_1$ ,  $A_2$ ) are placed a distance  $R$  apart with a centre of mass  $C$ , while the third particle  $B$  is orbiting around the common centre  $C$  in a plane which is perpendicular to the  $A_1A_2$  line. The unit vectors  $\vec{e}_1$  and  $\vec{e}_2$  are parallel with  $A_1B$  and  $A_2B$ , respectively.

just the energy of the third particle, which is at same time the energy of the entire cluster. Hence, there are three degrees of freedom, or equivalently three constants of motion, associated with the third particle (angular momentum, plane of the motion, total energy).

Actually we have to prove that such a geometric - structural model, as illustrated in Figure 1, can be materialized to have the angular momentum as the true constant of motion. Suppose that the third particle  $B$  has to move under the influence of two various forces,  $\vec{F}_1$  and  $\vec{F}_2$ , whose origins come from the identical particles placed at the points  $A_1$  and  $A_2$ , respectively. Then an angular momentum  $\vec{L}$  of the third particle is defined by a sum of two terms, each term coming from an appropriate vector product, as follows

$$\vec{L} = \vec{r}_1 \times \vec{p} + \vec{r}_2 \times \vec{p}, \quad (1)$$

where  $\vec{p}$  designates a linear momentum associated with the  $B$  particle. It is just a product over the mass of the particle ( $m_3$ ) and its velocity. The equation of motion for the vector  $\vec{L}$  is given by

$$\frac{d\vec{L}}{dt} = \frac{d}{dt}(\vec{r}_1 + \vec{r}_2) \times \vec{p} + (\vec{r}_1 + \vec{r}_2) \times \frac{d\vec{p}}{dt}, \quad (2)$$

where  $t$  is a local laboratory time. Writing

$$\vec{F}_1 + \vec{F}_2 = \frac{d\vec{p}}{dt}; \quad \vec{p} = m_3 \frac{d}{dt}(\vec{r}_1 + \vec{r}_2) = \vec{p}_1 + \vec{p}_2, \quad (3)$$

we obtain

$$\frac{d\vec{L}}{dt} = \frac{1}{m_3}(\vec{p}_1 + \vec{p}_2) \times (\vec{p}_1 + \vec{p}_2) + (\vec{r}_1 + \vec{r}_2) \times (\vec{F}_1 + \vec{F}_2). \quad (4)$$

It should be emphasized that a vector sum  $\vec{r}_1 + \vec{r}_2$  in equations (2) to (4) appears as a single vector in a plane which is perpendicular to the  $A_1A_2$  line. Therefore, the direction of the angular momentum vector  $\vec{L}$  is identical with the above mentioned line, Figure 1. Having in mind that central forces act simultaneously on the  $B$  particle, i.e.  $\vec{F}_1$  is parallel to  $\vec{r}_1$  while  $\vec{F}_2$  is parallel to  $\vec{r}_2$ , and taking into account that a vector product of parallel vectors vanishes, we can write equation (4) as follows:

$$\frac{d\vec{L}}{dt} = \frac{1}{m_3}(\vec{p}_1 \times \vec{p}_2 + \vec{p}_2 \times \vec{p}_1) + (\vec{r}_1 \times \vec{F}_2 + \vec{r}_2 \times \vec{F}_1). \quad (5)$$

The first term in equation (5) is obviously equal to zero. As to the second term in the brackets, it can be transformed into a specific form appropriate for the equation of motion

for  $\vec{L}$ . Hence,

$$\frac{d\vec{L}}{dt} = -e^2 \left( \frac{1}{r_1^3} - \frac{1}{r_2^3} \right) \vec{r}_1 \times \vec{r}_2. \quad (6)$$

We know that the vector product  $\vec{r}_1 \times \vec{r}_2$ , due to the geometric - structural model, cannot vanish and yet the angular momentum must be one of the constants of motion associated with the  $B$  particle, Figure 1. Hence,

$$\frac{d\vec{L}}{dt} = 0. \quad (7)$$

Therefore, it follows that a scalar equation  $r_1 = r_2$  must hold all the time.

It should be emphasized that this proof holds if and only if the particles  $A_1$  and  $A_2$  are identical so long as we are concerned with electrostatic forces.

We start from a reasonable approximation according to which electrostatic forces alone at long distances ( to be named a *long-range approach*) are sufficient to describe the actual stationary states so that the energy levels will be determined by the Hamiltonian  $H_{lr}$  to be constructed as follows. It must include an electron - electron interaction due to a Coulomb force, where the electrons are identified as the  $A_1, A_2$  points in Figure 1; it must also include two identical terms due to the Coulomb force acting between the heavy particle sitting at the  $B$  point in this figure with these two electrons; and finally this Hamiltonian must contain a kinetic energy as coming from an orbital motion of the heavy particle about the  $A_1 A_2$  line in Figure 1. We write, therefore,

$$H_{lr}(R, r_1) = -2\frac{e^2}{r_1} + \frac{e^2}{R} + \frac{2L^2}{m_3(4r_1^2 - R^2)}, \quad (8)$$

where  $L$  designates an angular momentum of the heavy particle. We will accept the energy levels in the regime of long - range forces to be described by an approximation where this angular momentum is determined by applying the so-called Niels Bohr's *third postulate* by which  $L = n\hbar$ . Here  $\hbar$  is Planck's constant divided by  $2\pi$ , while  $n = 1, 2, \dots$

In this case we obtain an equation of motion which the heavy particle performs in a regime materialized by the action of the electrostatic long - range forces. Stable and yet stationary states of the heavy particle are obtained by searching for a minimum of the entire energy by treating  $r_1, R$  as two independent variables. Therefore we write

$$\frac{\partial H_{lr}}{\partial R} = 0; \quad \frac{\partial H_{lr}}{\partial r_1} = 0. \quad (9)$$

Having solved equation (9) with a number of elementary transformations we obtain the energy of the stable and stationary state

$$H_{lr}(R, r_1) = -\frac{0.439}{n^2} \eta E_a. \quad (10)$$

Here  $E_a$  is an atomic unit of energy,  $a_0$  is an atomic unit of length,

$$E_a = \frac{m_1 e^4}{\hbar^2} = \frac{e^2}{a_0}. \quad (11)$$

Here  $\eta$  is a ratio of the two masses in question: a heavy particle  $m_3$  over the mass of the electron  $m_1$ ; i.e.  $\eta = m_3/m_1$ . Notice that the two apparently independent variables are, in a state of the lowest energy, linked by the relationship

$$R = 2^{1/3}r_1. \quad (12)$$

As already observed, we adopted in the present paper a method based on a reasonable assumption that the angular momentum of the heavy particle  $L$  is treated according to Niels Bohr's model of the ordinary hydrogen atom. Also we selected the coordinate system  $r, \vartheta, \varphi$  in such a way as to make a  $z$  axis to coincide with the  $A_1A_2$  line in Figure 1. In this particular case  $\vartheta = \pi/2$  while  $\varphi$  is arbitrary. Here the operator of the angular momentum becomes

$$\mathcal{L}^2 = -\hbar^2 \frac{d^2\psi}{d\varphi^2}; \quad \psi(\varphi) = \frac{1}{\sqrt{2\pi}} \exp(im\varphi). \quad (13)$$

In equation (13)  $m = 0, \pm 1, \pm 2, \dots$  is a magnetic quantum number. In this particular case the quantity  $|m|$ , for  $m$  different from zero, can be identified in Niels Bohr's atomic model with the angular momentum quantum number  $n$ . Just how good is the Niels Bohr's model in approaching some fundamental problems in atomic physics is studied by Berry (1989).

For practical reasons, the numerical values of the physical quantities introduced here are given in the appendix.

### 3. On the quantum-mechanical motion in a twodimensional potential field by having neglected magnetic forces among the electrons

Fortunately, cold - fusion reactions depend directly on a number of arguments coming from all three fields of research: classical, quantum - mechanical, as well as electrodynamic. In view of a classical model developed in Section 2, we will replace these equations by a more realistic formula which would be more appropriate in describing the orbital motion of heavy particles (protons, deuterons).

Therefore, we shall in the present section consider a quantum - mechanical solution of the following equation

$$-\frac{\hbar^2}{2m_3} \left( \frac{\partial^2}{\partial x^2} + \frac{\partial^2}{\partial y^2} \right) \Phi + [V(r) - W] \Phi = 0, \quad (14)$$

where a twodimensional electrostatic potential is defined by

$$V(r) = -2 \frac{e^2}{\sqrt{r^2 + (R/2)^2}}. \quad (15)$$

In equation (14)  $m_3$  is the heavy particle (proton, deuteron),  $W$  is the total energy of the particle whose motion is restricted in the  $xy$  plane passing through the midpoint between  $A_1$  and  $A_2$ , Figure 1. The solution will be achieved in a series of three computing stages. First, the total wave function will be represented by a product of two wave functions, one depending on  $r$ , another on the azimuthal angle  $\varphi$ . We write:

$$\Phi(r, \varphi) = \chi(r) \cdot \psi(\varphi); \quad x = r \cos \varphi; \quad y = r \sin \varphi. \quad (16)$$

Partial derivatives in a system of rectangular coordinates as appearing in equation (16) could be transformed into the system of polar coordinates, as follows,

$$\frac{\partial^2}{\partial x^2} + \frac{\partial^2}{\partial y^2} = \frac{\partial^2}{\partial r^2} + r^{-2} \frac{\partial^2}{\partial \varphi^2}. \quad (17)$$

Second, we introduce a dimensionless coordinate  $\rho$  and a dimensionless energy  $\epsilon$ , as follows

$$r = \eta^{-1} a_0 \rho; \quad W = \eta E_a \epsilon; \quad \eta = \frac{m_3}{m_1}; \quad (18)$$

$$a_0 = \frac{\hbar^2}{m_1 e^2}; \quad E_a = \frac{e^2}{a_0} = \frac{m_1 e^4}{\hbar^2}; \quad \xi = \frac{R}{a_0}. \quad (19)$$

Hence, equation (14) goes over into

$$\left( \rho^2 \frac{\partial^2}{\partial \rho^2} + \frac{\partial^2}{\partial \varphi^2} \right) \Phi + 2\rho^2 \epsilon \Phi + 4 \frac{\rho^2}{\sqrt{\rho^2 + (\xi/2)^2}} \Phi = 0. \quad (20)$$

Third, we now separate  $\chi(\rho)$  from  $\psi(\varphi)$ , by introducing a constant  $C$ , which leads to a couple of equations:

$$\frac{d^2 \psi}{d\varphi^2} = -C \psi(\varphi); \quad C = m^2, \quad (21)$$

$$\left( \frac{d^2}{d\rho^2} + 2\epsilon + \frac{4}{\sqrt{\rho^2 + (\xi/2)^2}} - \frac{C}{\rho^2} \right) \chi(\rho) = 0. \quad (22)$$

The term involving the potential field in equation (22) reflects the fact that all the algebraic transformations derived in Section 2 have a similar meaning as far as the stability condition is concerned. More mathematical details are elaborated in references: Novaković (2002, 2003, 2004). In the framework of quantum mechanics this condition will require almost the same numerical value for an angle closed by the unit vectors  $\vec{e}_1, \vec{e}_2$  in Figure 1, and that is  $78^\circ$ , almost the right angle! This condition leads to

$$R = 2r; \quad \xi = 2\rho; \quad \Rightarrow \frac{4}{\sqrt{\rho^2 + (\xi/2)^2}} = \frac{2\sqrt{2}}{\rho}. \quad (23)$$

The last equation (22), if supplemented with the stability condition according to equation (23), can be reduced to the eigenvalue problem whose solution is actually available, see Landau and Lifshitz (1987). Having introduced a substitution:

$$\chi(\rho) = \exp(-\alpha\rho) \rho^k \cdot h(\rho), \quad (24)$$

and two dimensionless quantities  $\alpha, k$

$$2\epsilon = -\alpha^2; \quad k = \frac{1}{2} \left( 1 + \sqrt{1 + 4m^2} \right). \quad (25)$$

we arrive at the following differential equation for  $h(z)$ , instead of  $h(\rho)$ ,

$$zh''(z) + (c - z)h'(z) - ah(z) = 0. \quad (26)$$

It is rather obvious that there are several abbreviations which simplify the structure of the differential equations. These are given by:

$$z = 2\alpha\rho; \quad c = 2k; \quad a = \frac{\alpha k - 2\sqrt{2}}{\alpha}. \quad (27)$$

Notice that the quantum number  $k$  appearing in equations (24) to (27) represents an orbital angular momentum of a particle moving in a two - dimensional potential field in the same way the quantum number  $\ell + 1$  in the case of a particle moving in the three - dimensional field does. This analogy is even more striking if we compare a few lowest - order quantum numbers. Here the possible values for  $k$  are given by

$$k = 1; \quad \frac{1}{2}(1 + \sqrt{5}); \quad \frac{1}{2}(1 + \sqrt{17}); \dots \quad m = 0, 1, 2, \dots \quad (28)$$

The actual solution of equations (24), (25) is obtained by employing the confluent hypergeometric function:

$$h(z) = N(a, c) \left[ 1 + \frac{az}{c1!} + \frac{a(a+1)z^2}{c(c+1)2!} + \dots \right], \quad (29)$$

where  $N(a, c)$  is a normalization factor to be determined from the condition

$$\int_0^\infty [\chi(\rho)]^2 \rho d\rho = 1. \quad (30)$$

First, we would like to emphasize that the above introduced integration runs over a plane, rather than the entire three-dimensional space as employed in conventional quantum - mechanical problems. Second, the representation (29) for the function  $h(z)$  must be interrupted in order to make the expansion series convergent. This will take place whenever the parameter  $a$  is a negative integer or zero. Therefore, by writing

$$a = -n_r, \quad n_r = 0, 1, 2, \dots \quad (31)$$

we obtain:

$$\alpha = \frac{\sqrt{2}}{k + n_r}; \quad \epsilon = -\frac{\alpha^2}{2} = -\frac{1}{(k + n_r)^2}. \quad (32)$$

Here  $n_r$  designates the number of nodes, i.e. the number of null - points of the polynomial  $h(z)$ . It is easy to evaluate the radius  $r$  at which the wave function  $[\chi(\rho)]^2\rho$ , (it represents a quantum - mechanical distribution associated with a planar motion of the particle), has a maximum. Indeed, assuming the lowest stationary state generated by the quantum number  $n_r = 0$ , we search for the solution

$$\frac{d}{d\rho} [\exp(-2\alpha\rho)\rho^{2k+1}] = 0 \Rightarrow \rho_0 = \frac{2k+1}{2\alpha}. \quad (33)$$

In conclusion, we should emphasize that equations (24), (25) and (31), (32) for large values of  $m$ , lead to expressions very similar to those of the particle dynamics in the three - dimensional electrostatic potential

$$k \approx m; \quad \epsilon \approx -\frac{1}{m^2}. \quad (34)$$

This result is to be compared with the well - known formula for the energy levels in the three - dimensional case,  $\epsilon \approx -1/(2n^2)$ , where  $2n^2$  stands in place of  $m^2$ . Besides, the particle moving in a two - dimensional electrostatic potential field behaves (for large values of  $m$ ) as if it has the angular momentum  $L \approx m\hbar$ , which is in agreement with Niels Bohr's third postulate  $L = n\hbar$  introduced in Section 2, with  $n$  replacing  $m$ .

#### 4. Classical approach to the three-particle cluster by having included magnetic forces among the electrons

Fortunately, it is technically possible to produce magnetic induction fields in the  $10^2$  T range (one tesla is equivalent to  $10^4$  gauss), but unfortunately it is hardly possible technically to generate the electric fields (actually the voltage drops) as required by the  $10^{16}$  s<sup>-1</sup> range. However, a metallic structure that might be combined with the property of a semiconductor, in one direction, and the property of a classical ferromagnet, in the other direction, might serve as one of hybridized geometric-structural devices capable of generating the electrodynamic environment as required by the present theoretical model.

Chemical elements of the palladium group (a charge number  $Z = 46$ ) may expose properties of a semiconductor like germanium ( $Z = 32$ ); but they also may expose a ferromagnetic property of the metallic lattice like iron ( $Z = 26$ ). To demonstrate these properties we shall outline briefly some important points of the band theory within a quantum - mechanical approach.

Palladium has the envelope of nickel in addition to the electron configuration

$$(4s)^2(4p)^6(4d)^{10}.$$

On the one hand, a semiconducting order is to be partially expected (due to a possible overlapping between the  $4s$  and  $4p$  energy bands) with some electron concentration  $N_s$ , along one of the crystallographic axes. On the other hand, we should also expect partially a ferromagnetic order (due to a possible overlapping between the  $4s$  and  $4d$  energy bands) to be materialized with another electron concentration  $N_f$ , along a different crystallographic axis. Clearly, the two electron concentrations here introduced must satisfy an equation of the form

$$N_s = \frac{8}{46}N; \quad N_f = \frac{10}{46}N, \quad (35)$$

where  $N$  designates a total available number of electronic charges on the lattice structure of palladium, reduced to a unit volume.

Let us assume that the two different concentrations are materialized in two different directions  $y, -x$ , respectively. If the former process is in question we shall expect the kind of a plasma frequency which may appear as follows. Suppose that the electrons within the  $N_s$  concentration are displaced some distance  $\vec{b}$  along the  $y$  axis with respect to the lattice composed of positive ions. Then, according to Brown (1967) and Ziman (1972), there will appear a polarization,  $\vec{P}$ , such that

$$\vec{P} = N_s e \vec{b}. \quad (36)$$

This will generate an electric field  $\vec{E}$  in the form

$$\vec{E} = -4\pi \vec{P}. \quad (37)$$

Now the equation of motion of each charge within the available concentration  $N_s$  will be given by

$$m_0 \frac{d^2 \vec{b}}{dt^2} = e\vec{E} = -4\pi N_s e^2 \vec{b}. \quad (38)$$

Here  $m_0$  designates the mass of the electron within the available concentration  $N_s$ ,  $t$  is a local laboratory time. With  $\omega$  the plasma frequency and  $\vec{A}$  an arbitrary amplitude, we can write the solution of equation (38)

$$\vec{b} = \vec{A} \cos(\omega t); \quad \omega = \left( \frac{4\pi}{m_0} N_s e^2 \right)^{1/2}. \quad (39)$$

Here we include a possible action of the two electrons, which are localized at the  $A_1 A_2$  points in Figure 1, that comes from an interaction between the two magnetic moments  $\vec{\mu}_1, \vec{\mu}_2$ . Indeed, the relevant interaction term may be written

$$U_{mag} = \frac{(\vec{\mu}_1 \cdot \vec{\mu}_2)}{R^3} - 3 \frac{(\vec{\mu}_1 \cdot \vec{R})(\vec{\mu}_2 \cdot \vec{R})}{R^5}, \quad (40)$$

where  $R$  is identical with the length  $A_1 A_2$  in Figure 1. Having assumed that the two magnetic moments are parallel with a magnetic induction vector  $\vec{B}$ , and also with the above introduced  $A_1 A_2$  line, we can easily incorporate this term into the long-range Hamiltonian considered in Section 2. For this reason, one has to evaluate the point where the potential  $e^2/R$  (as coming from an electrostatic repulsion) becomes equal to the absolute value of the potential term

$$U_{mag}(R) = -\frac{\alpha}{R^3}; \quad \alpha = 2\mu_B^2. \quad (41)$$

Notice that  $U_{mag}$  is coming from an entirely attractive force. The total Hamiltonian, including those terms introduced in Section 2, now becomes

$$H_t(R, r_1) = H_{lr}(R, r_1) + U_{mag}(R). \quad (42)$$

A detailed study of this effect requires the introduction of a *cold-fusion unit of length*  $b_0$  and also a *cold-fusion unit of energy*  $E_b$ . By definition

$$\frac{e^2}{R} - \frac{\alpha}{R^3} = 0 \quad \Rightarrow \quad R = b_0. \quad (43)$$

Having solved equation (43) we arrive at the result:

$$\alpha = e^2 b_0^2; \quad b_0 = \sqrt{2} \frac{\hbar}{2m_0 c} = 273.05 \cdot 10^{-13} \text{ cm}; \quad (44)$$

$$a_0 = 193.80 b_0; \quad E_b = 193.80 E_a = 5274.1 \text{ eV}. \quad (45)$$

Here  $c$  designates the speed of light. It should be emphasized that an electron - electron interaction (a combination of repulsion as well as attraction) will influence the heavy particle (proton, deuteron) to move, under the action of a Lorentz force, within a deep potential field.

A detailed analysis is based on an extensive use of various transformations, similar to those reported in Section 2. It is sufficient for the present purpose to quote here some

of the final results. At first we search for a minimum of the total energy by solving the equations

$$\frac{\partial H_t}{\partial R} = 0; \quad \frac{\partial H_t}{\partial r_1} = 0. \quad (46)$$

Solving these equations will give us a minimum of  $H_t$ . To do this, we introduce two dimensionless coordinates  $\rho, \rho_1$ , instead of the physical variables  $R, r_1$ , as follows:

$$R = \rho b_0; \quad r_1 = \rho_1 b_0. \quad (47)$$

Therefore the minimum of  $H_t$  becomes

$$H_t(R, r_1) = \left( -\frac{1}{\rho_1} + \frac{0.5}{\rho} + \frac{0.5}{\rho^3} \right) \frac{e^2}{b_0}; \quad (48)$$

$$\rho_1 = \left[ 0.5\rho^5 / (\rho^2 - 3) \right]^{1/3}. \quad (49)$$

Furthermore, we can treat the number  $n(R, r_1)$ , which appears in the angular momentum of the proton (deuteron), as a continuous variable. So, the quantity  $L(R, r_1) = \hbar n(R, r_1)$  becomes a continuous variable in the same way as does the number  $n$  in the expression  $L = n\hbar$ . Having performed a series of elementary transformations we arrive at

$$n(R, r_1) = \left[ K_1(4\rho_1^2 - \rho^2) \left( \frac{1}{\rho_1} - \frac{0.5}{\rho} + \frac{1.5}{\rho^3} \right) \right]^{1/2}, \quad (50)$$

where  $K_1(p) = 4.73681$  is just a dimensionless numerical factor. It should be emphasized that this numerical factor, in passing over from protons to deuterons, will be replaced by a value twice as large, i.e.  $K_1(d) = 2K_1(p)$ .

It is absolutely obvious from the above introduced equations that such a motion will be restricted within a range where  $R \gg b_0$ . However, as  $R$  approaches the critical limit  $R_{crit} = \sqrt{3}b_0$ , the heavy particle will experience a tight binding state within the  $A_1BA_2$  triangle, Figure 1. Furthermore, having treated the quantum number  $n$  as a continuous function of the variables  $R, r_1$ , we disclosed that there will appear a tight minimum around the value  $n(R, r_1) \approx 5$  for protons, whereas  $n(R, r_1) \approx 7$  for deuterons. If combined with the angular momentum  $L = n\hbar$ , an orbiting speed of the heavy particle will also become a function of the same variables, i.e.  $v = v(R, r_1)$ . In this case and under these conditions this physical quantity will be given by

$$v(R, r_1) = \frac{2n(R, r_1)\hbar}{m_3\sqrt{4r_1^2 - R^2}} = \left[ K_2 \left( \frac{1}{\rho_1} - \frac{0.5}{\rho} + \frac{1.5}{\rho^3} \right) \right]^{1/2}, \quad (51)$$

where  $K_2$  is another numerical factor defined by  $\sqrt{K_2(p)} = 1.00595 \cdot 10^8 \text{ cms}^{-1}$ . As in the previous case, here again in passing over from protons to deuterons it must be replaced by a somewhat different factor, i.e.  $\sqrt{K_2(d)} = 0.7113 \cdot 10^8 \text{ cms}^{-1}$ .

Just how the heavy particle ( $p, d$ ) may experience a rotational motion under the above described conditions is analyzed and discussed in Section 6.

## 5. A time-dependent Lorentz force

Turning now to a possible action of the ferromagnetic order of the electrons within the available concentration  $N_f$  we may introduce a magnetic induction vector  $\vec{B}$  along the  $-x$

axis. With Feynman's (1964) definition of the external magnetic field  $\vec{H}$  we write:

$$\vec{B} = \vec{H} + \vec{M}/(\epsilon_0 c^2); \quad \epsilon_0 c^2 = 10^7/4\pi. \quad (52)$$

Here  $\vec{M}$  designates a sum of all magnetic moments of the electrons ( $\mu_B$ ) within the available concentration  $N_f$  reduced to a unit volume.

Just how the electrons might attain some motionless positions, even for a short time interval, while the heavy particle ( $p$ , or  $d$ ) performs a rotational motion may be gained from the following idea. Suppose, the mentioned composite cluster moves in a linear direction under the action of the crossed electric field and a magnetic induction,  $E_y$  and  $B_x$ , with a certain initial velocity  $\vec{v}_0$ , Figure 2. Such a combined field is named a *Lorentz force*, see Burghes and Downs (1975), Feynman *et al* (1964), and Yavorsky and Pinsky (1987).

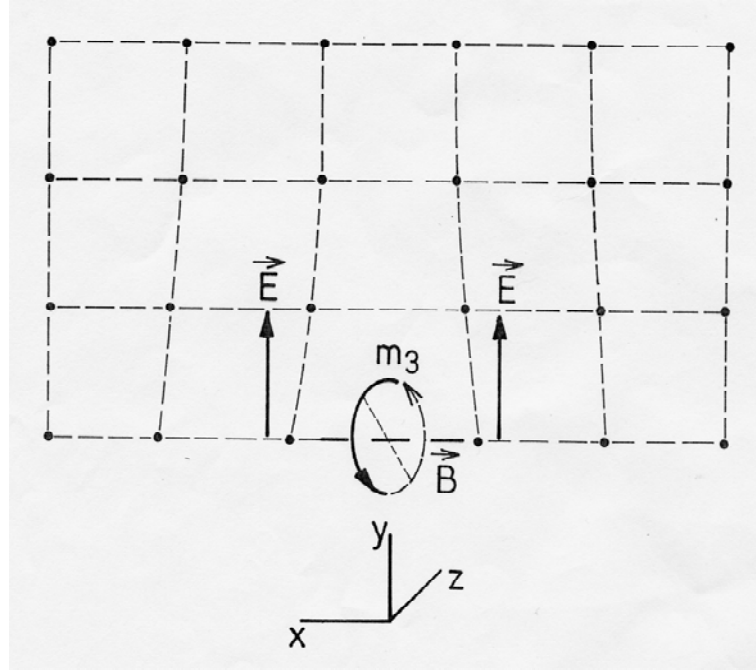


**Figure 2.** An electric field  $\vec{E}$  along the  $y$  axis and a magnetic induction  $\vec{B}$  along the  $-x$  axis are depicted to represent a Lorentz force acting on a proton (deuteron) within a palladium metallic lattice. The former component of the Lorentz force may come from an overlapping between the  $(4s)^2(4p)^6$  electron wave functions (resembling a semiconductor), while the latter component may be generated by the presence of the  $(4d)^{10}$  localized electrons (resembling a ferromagnet).

The motion of each particle with the charge  $q$  and mass  $m$  is compelled by the Lorentz force  $\vec{F}$  according to the equations

$$\vec{F} = q(\vec{E} + \vec{v} \times \vec{B}), \quad (53)$$

$$\vec{v} \times \vec{B} = \begin{vmatrix} \vec{u}_1 & \vec{u}_2 & \vec{u}_3 \\ v_x & v_y & v_z \\ -B_x & 0 & 0 \end{vmatrix}. \quad (54)$$

We shall consider specifically the clusters  $e_1^- p e_2^-$ , or  $e_1^- d e_2^-$ , with the following characteristic parameters; electron ( $q = -e, m = m_1$ ), proton ( $q = e, m = m_p$ ), and deuteron

( $q = e, m = m_d$ ). Obviously, the three unit vectors  $\vec{u}_1, \vec{u}_2, \vec{u}_3$ , are oriented along the rectangular system of axes  $x, y, z$ , respectively. We write the equations of motion

$$F_x = m_3 \dot{v}_x = 0; \quad F_y = m_3 \dot{v}_y = qE_y - qB_x v_z; \quad (55)$$

$$F_z = m_3 \dot{v}_z = qB_x v_y. \quad (56)$$

Here  $e$  is an elementary electrostatic charge. Dots on the components of the velocity designate the appropriate time derivatives. The solutions to the system of the above linear equations with constant coefficients ( $m_3, q, B_x$ ) are some functions of a local laboratory time  $t$ ,  $y(t)$  and  $z(t)$ , as well as  $E_y$ , such that the entire motion, under the action of a Lorentz force, develops in the  $yz$  plane.

In the first stage we write the set of solutions in terms of the laboratory time  $t$  jointly with the initial conditions. By introducing certain integration constants  $A_1, A_2, C_1, C_2, E_1, E_2$  we write the set of solutions in terms of the parameters  $a, b$

$$a = m_3 |\omega|; \quad b = |q| B_x. \quad (57)$$

In equation (57) both  $\omega, q$  are positive for charged particles ( $p, d$ ), whereas negative for electrons.

Notice that both  $a$  and  $b$  have one and the same dimension. The solutions are:

$$v_x = v_0 = 0; \quad (58)$$

$$v_y = A_1 \cos(\omega t) + A_2 \sin(\omega t); \quad (59)$$

$$v_z = C_1 \cos(\omega t) + C_2 \sin(\omega t); \quad (60)$$

$$E_y = E_1 \cos(\omega t) + E_2 \sin(\omega t). \quad (61)$$

If now the initial conditions are imposed on equations (59) to (61) then there will appear four relations connecting the integration constants above introduced. We write

$$A_1 = -\frac{qa}{a^2 - b^2} E_2; \quad A_2 = \frac{qa}{a^2 - b^2} E_1; \quad (62)$$

$$C_1 = -\frac{qb}{a^2 - b^2} E_1; \quad C_2 = -\frac{qb}{a^2 - b^2} E_2. \quad (63)$$

One more stage is required to integrate over the fundamental equations so far introduced in order to obtain the solutions in terms of a Cartesian system of coordinates. Apart from  $x$  we arrive at

$$y = y(t) = y_0 + \frac{1}{\omega} [A_1 \sin(\omega t) - A_2 \cos(\omega t)]; \quad (64)$$

$$z = z(t) = z_0 + \frac{1}{\omega} [C_1 \sin(\omega t) - C_2 \cos(\omega t)]. \quad (65)$$

Having studied the structure of the solutions one easily observes that each charged particle (either electrons  $e_1^-, e_2^-$ , protons  $p$ , or deuterons  $d$ ) will move along the circle with a certain radius  $R(\omega, B_x)$ . We write

$$[y(t) - y_0]^2 + [z(t) - z_0]^2 = R(\omega, B_x)^2, \quad (66)$$

where  $y_0, z_0$  are certain integration constants to be determined from the initial conditions imposed on the particles as they enter the field of the Lorentz force.

The radius of the circular orbit for each of the charged particles depends on two vital parameters, one being the frequency of the electric force ( $\omega$ ), the other is the strength of the magnetic induction field ( $B_x$ ). We obtain

$$R(\omega, B_x) = \frac{|q|}{\omega(a^2 - b^2)} \left[ a^2(E_1 \cos(\omega t) + E_2 \sin(\omega t))^2 + b^2(E_1 \sin(\omega t) - E_2 \cos(\omega t))^2 \right]^{1/2}. \quad (67)$$

Therefore, the electrons move in one direction around the magnetic induction field  $\vec{B}$ , while the heavy particles ( $p$ , or  $d$ ) move in the opposite direction. Light particles (electrons) will describe smaller circles in such a way as to materialize a left - handed coordinate system with respect to the vector of the magnetic induction field. On the contrary, heavy particles (protons, deuterons) will describe larger circles, exactly  $\eta = m_3/m_1$  times, in the opposite direction, whereby materializing the right - handed coordinate system with respect to the vector of the above mentioned field. It is important to emphasize that by "electrons" in this particular study we must understand those electrons coupled firmly with the ionic lattice, so that the actual mass  $m_1$  and of course  $m_2$  must be in the range of heavy ions which compose the metallic lattice.

In a theoretical model those "electrons" are motionless or almost motionless all the time. At the origin, marked by  $O$ , Figure 2, the material cluster starts its simple spiralling, highly rhythmic dancing, along the magnetic induction field lines. Compared to heavy particles those "electrons" will perform their motions in the opposite direction. Also the circles are centered differently for the two kinds of particle. A similar problem was studied by Burghes and Downs (1975) in relation to the Hall drift, an effect coming from a classical theory of magnetoconductivity.

Having analyzed this situation it seems that there is a strong probability of having the three - particle cluster to collapse to a more profound bound state as predicted by specifically geometric - structural model.

## 6. Critical values of orbiting frequency, magnetic induction field, and orbital radius

So far introduced physical quantities may become rather crucial in studying further the cold - fusion phenomena, in particular an orbiting frequency  $\omega$  and the magnetic induction field  $B_x$ , both quantities having being imposed from the outside on the motion of heavy particles (protons, or deuterons). Therefore an orbital radius of the heavy particle will be determined exactly by those two quantities as part of the cold - fusion channels. If we continue to study this theoretical model in more detail then we arrive at the following mechanism by which the three - particle clusters go over from one to the other. On the one hand, the three - particle cluster exists as a system in a tightly bound state as indicated by a specialized geometric structure, *Model two* or  $e^-p(d)e^-$ . It is a hydrogen molecular ion  $H_2^+$ , as sketched as item (ii) in Section 2. This is then equivalent to suggesting that a Lorentz force has produced a system where the heavy particle (proton, deuteron) spends some time in one of highly - excited quasi - stationary states. On the other hand, such a

state is not stable just because it may last as long as the actions of an electric field ( $\vec{E}$ ) combined with the magnetic induction field ( $\vec{B}$ ) take place.

Therefore, we should expect that there is some probability of initiating the collapse of the three - particle cluster into a more profound bound state as established by *Model one*, or  $H^-$ . It is a negative hydrogen ion  $H^-$ , as sketched as item (i) in Section 2.

In an actual experiment one should expect the physical mechanism to take place in the opposite direction. Indeed, there will appear *Model one* (hydrogen ions, where a proton keeps the two electrons in a common orbital plane) in the first place, while *Model two* (proton performing an orbital motion about the axis as materialized by the motionless electrons) will come later by following the above mentioned actions of  $\vec{E}, \vec{B}$ .

With an internuclear distance of the order  $2.8 \cdot 10^{-8}$  cm, an average density 8 times the density of water, we are able to estimate the electron concentrations  $N_s, N_f$  introduced in Section 4, as follows

$$N_s \approx 7.8 \cdot 10^{21} \text{ cm}^{-3}; \quad N_f \approx 9.8 \cdot 10^{21} \text{ cm}^{-3}. \quad (68)$$

To obtain a numerical insight into the geometric - structural mechanism we employ the system of units where  $1 \text{ J} = 10^7 \text{ erg}$ ;  $1 \text{ T} = 10^4 \text{ G}$ , see the appendix. The frequency of the proton orbiting about the vector  $\vec{B}$  is estimated to cover the  $\omega \approx 10^{16} \text{ s}^{-1}$  range, while the strength of the magnetic induction field is something like  $B_x \approx 0.1 \text{ T}$ . The vital parameters  $a, b$  are given by

$$a = m_p |\omega| \approx 10^{-11} \text{ kgs}^{-1}; \quad b = |q| B_x \approx 10^{-20} \text{ kgs}^{-1}. \quad (69)$$

We can observe that the present critical condition according to equations (57) and (69), which implies an equality  $a = b$  in order to produce a considerable value in the radius of the orbiting proton, is not in a full expected agreement by nine orders of magnitude. In other words, if the parameter  $a$  should achieve a value something like  $10^{-11}$ , by using a hybrid semiconductor - ferromagnetic structure, then the other parameter  $b$  may achieve only the value something like  $10^{-20}$ , a figure nine orders of magnitude smaller.

However, even with a small strength  $B_x$  of the magnetic induction field, a lattice structure of palladium might generate an orbital motion of protons (deuterons), both classically and quantum - mechanically, about the vector  $\vec{B}$  - a mechanism necessary for the liberation of energy. What is more important, some other members of the palladium group might also meet the physical conditions as visualized by the present theoretical prediction.

## 7. Proton dynamics materialized by low-lying energy levels

We arrive at the following numerical evidence.

(1) We must in the first place make a clear distinction between a broadly bound states of the heavy particle ( $p, d$ ), which are characterized by large values of  $n$ , and those tightly bound states to be generated by an interaction as coming from the magnetic moments of the two electrons. With Niels Bohr's third postulate within the limits of classical mechanics one obtains a straightforward interpretation. If the heavy particle (proton, deuteron) should perform its orbital motion in a plane which is perpendicular to the line connecting the two electrons, as depicted in Figure 1, then we may associate an angular momentum operator

$$L = \hbar \cdot n(R, r_1)_{min} , \hbar \cdot [n(R, r_1)_{min} + 1], \dots \quad (70)$$

where obviously this series can be continued.

If we accept an approximation by which the orbital motion of heavy particles (protons, deuterons) is determined by a series of energy levels  $H_t(R, r_1)$  then one might establish a fundamental relationship between this physical quantity and the quantum numbers  $n(R, r_1)$  as follows,

$$H_t(R, r_1) = -\frac{const}{n(R, r_1)^2}, \quad (71)$$

where  $const$  is a constant with the dimension of energy. Its numerical value has the order of magnitude  $const \approx 24 \cdot 10^3$  eV.

Using the results of Section 4 where the minimum of  $n$  is established to be around  $n(R, r_1)_{min} \approx 5$  for protons, whereas around  $n(R, r_1)_{min} \approx 7$  for deuterons, we could estimate the energy difference that corresponds to the two lowest energy levels. For protons, one such level with  $n(R, r_1) = 5$  and another with the next value  $n(R, r_1) = 6$  will supply a useful data base that can be tested experimentally. Using equations as derived in Section 4, we obtain this energy difference as follows

$$H_t(R, r_1)[n = 6] - H_t(R, r_1)[n = 5] = \hbar\omega[n = 6 \rightarrow n = 5], \quad (72)$$

with an obvious meaning of the used symbols. Using equations (46) to (49) we obtain the orbital frequency, for protons,

$$\omega[n = 6 \rightarrow n = 5] = 5 \cdot 10^{17} \text{ s}^{-1}. \quad (73)$$

The frequency expressed by equation (73), if compared with the plasma frequency of an electron fluid which is generated within a lattice volume of a semiconductor as considered in Section 4, is naturally suggesting that the two phenomena are in resonance. In other words, an orbital frequency  $10^{17} \text{ s}^{-1}$  of the heavy particle (proton, deuteron) about the  $A_1A_2$  line as its axis of rotation, Figure 1, on the one hand, is in a tight resonance with the electron fluid and its frequency  $10^{16} \text{ s}^{-1}$  within the lattice volume of a semiconductor, on the other hand.

A full list of energy levels for protons for low - lying quantum numbers, starting from  $n = 5$  up to  $n = 9$ , is given in Table 1.

**Table 1.** Low-lying levels for protons, outlined by three parameters as follows; Quantum numbers  $n + 1 \rightarrow n$  as they appear in Niels Bohr's angular momentum  $L = \hbar n$ ; classical radii  $R[n + 1] \rightarrow R[n]$  in units  $b_0$  as they are associated with subsequent transitions; energy levels  $H_t[n + 1] - H_t[n]$  in units eV.

$n + 1 \rightarrow n$	$R[n + 1] \rightarrow R[n], b_0$	$H_t[n + 1] - H_t[n], \text{eV}$
6 $\rightarrow$ 5	5.9 $\rightarrow$ 2.9	330.035
7 $\rightarrow$ 6	8.5 $\rightarrow$ 5.9	175.161
8 $\rightarrow$ 7	11.3 $\rightarrow$ 8.5	109.345
9 $\rightarrow$ 8	14.5 $\rightarrow$ 11.3	73.6705
...	...	...

These energy levels may be continued up to the point in the spectrum where the heavy particles are no longer bound to the metallic lattice.

This type of analysis may be performed for deuterons, but one must expect slightly different numerical results due to a different mass in passing over from the protons to deuterons, as shown in Table 2.

**Table 2.** Low-lying levels for deuterons, outlined by three parameters,  $n + 1 \rightarrow n$ ;  $R[n + 1] \rightarrow R[n]$ ;  $H_t[n + 1] - H_t[n]$ , similar to Table 1.

$n + 1 \rightarrow n$	$R[n + 1] \rightarrow R[n], b_0$	$H_t[n + 1] - H_t[n], \text{eV}$
8 $\rightarrow$ 7	5.1 $\rightarrow$ 2.9	243.208
9 $\rightarrow$ 8	6.8 $\rightarrow$ 5.1	161.424
10 $\rightarrow$ 9	8.7 $\rightarrow$ 6.8	110.001
11 $\rightarrow$ 10	10.7 $\rightarrow$ 8.7	79.4355
...	...	...

## 8. Discussion and conclusions

(1) Just how the two kinds of particle, bound at the beginning as a linear triatomic molecule  $e^-pe^-$ , or  $e^-de^-$ , like a helium atom, may achieve a very deep bound state is observed from a series of very fundamental theoretical arguments presented in Sections 5, 6. Indeed, under the action of an electric field coupled to a magnetic induction field, the linear triatomic molecule becomes broken in such a way as to form a right angle (or, almost the right angle) as closed by the straight lines  $e_1^- - p$  and  $p - e_2^-$ . According to equations as derived in Section 5, the "electrons" would stay almost motionless while the heavy particle ( $p$ , or  $d$ ) will perform a spiralling, highly rhythmic dancing, in circles which are three orders of magnitude larger than those performed by those "electrons". Using a proper vocabulary, this situation will greatly enhance the chance for the generation of partially stable states, until the linear triatomic molecule collapses into a tightly bound state as studied and analyzed in details in Sections 2, 3, and 4.

In order to gain a numerical insight into the physical mechanism we quote the following estimation. If only the electric field  $\vec{E}$  is acting, while the magnetic induction is vanishing  $\vec{B} = 0$ , the physical system could still achieve a stable state by allowing the proton, or deuteron, to perform a linear oscillatory motion along the  $y$  axis, with a frequency  $\omega$  according to equations as derived in Sections 5 and 6. Such a linear oscillatory motion would not be capable of initiating the molecule  $e^-p(d)e^-$  to collapse into one of profoundly bound states as visualized in the present work. It is possible to estimate a diameter outlined by the heavy particle in its orbital motion around the  $A_1A_2$  line as its axis of rotation in Figure 1.

Indeed, using equation (67) under the assumption that the parameter  $a \approx m_p\omega$ , while the other parameter vanishes  $b \approx 0$ , we obtain

$$R_p(\omega, B_x) \approx \frac{|q|}{m_p\omega^2} E_y. \quad (74)$$

In actual fact the product  $|q|E_y$  appearing in equation (74) is identical with the product  $m_0\omega^2 A$  appearing in the equation of motion of a particular electron within the electron fluid of the lattice volume in a semiconductor. If we accept this assumption as a reasonable approximation we obtain a radius of the orbital motion of a heavy particle as follows

$$R_p(\omega, B_x) \approx \frac{m_0}{m_p} A, \quad (75)$$

where  $A$  designates some amplitude associated with an individual electron as comprised by the electron fluid of the semiconductor. This physical quantity has an order of magnitude

$10^{-8}$  cm up to  $10^{-7}$  cm, so that the actual orbital radius of a heavy particle (proton, deuteron) has an order of magnitude  $10^{-11}$  cm up to  $10^{-10}$  cm. This shows that there are two phenomena in resonance. In other words, an orbital motion of a particular heavy particle by the action of a combined time-dependent electric field  $E_y$  and a constant magnetic induction field  $B_x$  which generate some orbital radius  $R(\omega, B_x)$ , on the one hand, is in a tight resonance with the plasma dynamics in a lattice volume of a semiconductor which generates a linear displacement  $A$  of the genuine electron, on the other hand.

One concludes, upon comparing equations as derived in Sections 5 and 6, that orbiting speeds of heavy particles are equally favourable with respect to the condition necessary for the appearance of a cold - fusion reaction, here fixed by the limit  $10^9$  cms $^{-1}$ . It is very important to notice that an electron - electron magnetic interaction would be absent if the magnetic induction  $\vec{B}$  were too weak to make the magnetic moments parallel with the  $A_1A_2$  line in Figure 1.

(2) In order to gain a numerical insight into the physical mechanism we quote the following estimation. In the first place we must keep in mind that there should exist a function  $P(v)$  which will determine some finite although small probability, for a speed  $v$  of a given heavy particle, to penetrate into the Coulomb barrier established by another heavy particle. Using the textbook of Landau - Lifshitz (1987) we can write the function  $P(v)$ , for values within a reasonable interval of speeds, as follows

$$P(v) = \exp\left(-\frac{2\pi}{\hbar v}e^2\right). \quad (76)$$

If only the electric field  $\vec{E}$  were acting, while the magnetic induction field were vanishing ( $\vec{B} = 0$ ), the physical system could still achieve a stable state by allowing the proton, or deuteron, to perform a linear oscillatory motion along the  $y$  axis.

It is reasonable to assume, on the one hand, that a frequency of the orbiting heavy particle will achieve an upper limit, within a given concentration of the semiconducting electrons  $N_s$ , which we can take as the numerical evidence  $\omega_{upp} = 10^{16}$  s $^{-1}$ . On the other hand, all the available space within the lattice volume, left to heavy particles, will be limited by a lattice constant; hence, an upper amplitude associated with the linear oscillatory motion of these particles is expected to be something like  $A_{upp} = 10^{-8}$  cm. Having combined these pieces of evidence, we arrive at another limit which the speed of the heavy particle must fulfill, i.e.  $v_{upp} = A \cdot \omega = 10^8$  cms $^{-1}$ . Therefore, the probability to penetrate into the Coulomb barrier is given by

$$P(v_{upp}) = \exp\left(-\frac{2\pi}{\hbar v_{upp}}e^2\right) = 10^{-6}. \quad (77)$$

In other words, such a probability of penetration would be generated by an action of the electric field  $E_y$  alone.

(3) A heavy particle ( $p$ , or  $d$ ) acquires some amount of energy, however small, to perform fast transitions between one of the low-lying stationary states and another among the highly placed stationary states within the energy spectrum. This requires a further theoretical insight into the exact electrodynamic mechanism by which these particles collide with each other, before they fuse, in order to release energy. No doubt, this mechanism is connected with and generated by a spectrum of elementary excitations within the metallic lattice itself. As shown in Table 1 for protons and Table 2 for deuterons, the low-lying energy differences may serve as a guiding idea of how one can use optical methods to

initiate and excite those differences, all the way from a continuous spectrum down to the point where the heavy particles fuse each other.

Let us suppose that an electron plasma in the metallic lattice takes place in the exchange of energy of the proton in the one among the highly excited states and the ground state which belongs to one of the tightly bound states of the  $e_1^- p e_2^-$  material cluster. This exchange process requires  $N_{pl}$  elementary excitations on account of the electron plasma. However, such a physical process may take place only if the proper energy balance holds all the time. Indeed, we can write

$$N_{pl}\hbar\omega = H_t[n = \infty] - H_t[n = 5], \quad (78)$$

where the plasma oscillations are in the  $10^{16} \text{ s}^{-1}$  frequency range, while the energy difference in equation (78) is something like  $24 \cdot 10^3 / 5^2 \text{ eV} \approx 10^3 \text{ eV}$ , according to equation (71). Now by inserting these numbers into (78) we obtain:

$$N_{pl} \approx 10^2. \quad (79)$$

The result of the equation (79) has a very simple interpretation. It tells us that a metallic lattice, through its spectrum of oscillations, will have to pay the cost of approximately  $10^2$  its elementary excitations in order to enable the proton to initiate a transition from the continuous spectrum down to one of the tightly bound states.

A similar conclusion may be obtained if protons are replaced by deuterons. Actually, the number of elementary excitations of the electron plasma within a metallic lattice, in order to enable the deuteron to initiate a similar transition is even smaller, being something like  $N_{pl} \approx 50$ .

## Appendix

Here are the most frequently used physical constants: atomic unit of length or Niels Bohr's radius  $a_0$ ; atomic unit of energy  $E_a$ ; mass of the free electron  $m_0$ ; mass of the proton  $m_3 = m_p$ ; mass of the deuteron  $m_3 = 2m_p$ ; Planck's constant divided by  $2\pi$ ,  $h/2\pi = \hbar$ ; elementary charge on the electron as well as on the proton  $|q| = e$ ; Bohr's magneton  $\mu_B$ ; cold-fusion unit of length  $b_0$  and cold-fusion unit of energy  $E_b$ . All these quantities are expressed in practical units or the *Systeme International d'Unites*, often called the SI system.

$$\begin{aligned} a_0 &= 0.529 \cdot 10^{-10} \text{ m}; & E_a &= 27.214 \text{ eV} = 4.360 \cdot 10^{-18} \text{ J}; \\ m_0 &= 9.1 \cdot 10^{-31} \text{ kg}; & m_3 &= m_p = 1836m_0; & m_d &= 2m_p; \\ \hbar &= 1.05 \cdot 10^{-34} \text{ Js}; & |q| &= e = 1.602 \cdot 10^{-19} \text{ C}; \\ \mu_B &= 9.724 \cdot 10^{-24} \text{ JT}^{-1}; & b_0 &= \sqrt{2} \frac{\hbar}{2m_0c} = 273.05 \cdot 10^{-15} \text{ m}; \\ a_0 &= 193.80b_0; & E_b &= 193.80E_a = 5274.1 \text{ eV}. \end{aligned}$$

## Acknowledgments

I am deeply indebted to Professor Robert Blinc and his research group for the warm

hospitality during my visits to the Jožef Stefan Institute in Ljubljana, Slovenia, in the period 1998 - 2004, where I completed this work.

## References

1. A. O. Barut and G. Craig, *Physica A* **197**, 275 (1993).
2. A. Dragić, Z. Marić, and J. P. Vigier, *Physics Letters A* **265**, 163 (2000).
3. V. A. Kirkinski and Yu. A. Novikov, *Europhysics Letters* **46**, 448 (1999).
4. M. H. Miles, *Journal of Electroanalytical Chemistry* **482**, 56 (2000).
5. H. K. Oh, *Journal of Materials Processing Technology* **94**, 60 (1999).
6. J. Xiao and P. Li, *International Journal of Hydrogen Energy* **24**, 741 (1999).
7. K. Kamada, *Fusion Engineering and Design* **55**, 541 (2001).
8. E. Cisbani, G. M. Urciuoli, S. Frullani, F. Garibaldi, F. Giuliani, D. Gozzi, M. Gricia, M. Iodice, M. Lucentini, and F. Santavenere, *Nuclear Instruments and Methods in Physics Research A* **459**, 247 (2001).
9. D. J. Nagel, *Radiation Physical Chemistry* **51**, 653 (1998).
10. D. Voss, *Physics World* **12**(3), 12 (1999).
11. R. S. Berry, *Contemporary Physics* **30**, 1 (1989).
12. Lj. Novaković, *Journal of Research in Physics* **29** No. 1, 13 (2002).
13. Lj. Novaković, *Kragujevac Journal of Science* **25**, 5 (2003).
14. Lj. Novaković, *International Journal of Hydrogen Energy* **29**, 1397 (2004).
15. L. D. Landau and E. M. Lifshitz, *Quantum Mechanics*, Section 50 (Pergamon Press, Oxford, 1987).
16. F. C. Brown, *The Physics of Solid State*, (W. A. Benjamin, Inc., New York, Amsterdam, 1967).
17. J. M. Ziman, *Principles of the Theory of Solids*, (University Press, Cambridge, 1972).
18. D. N. Burghes and A. M. Downs, *Modern Introduction to Classical Mechanics and Control*, (Ellis Horwood Limited, Coll House, Chichester, Sussex, England, 1975).
19. R. P. Feynman, R. B. Leighton, and M. Sands, *The Feynman Lectures on Physics, Mainly Electromagnetism and Matter*, (Addison - Wesley Publishing Company, Reading, Massachusetts, 1964).
20. B. M. Yavorsky and A. A. Pinsky, *Fundamentals of Physics*, volume I, (Mir Publishers, Moscow, 1987).

## Background Reduction Using Fe and Pb Shielding

D. S. Mrđa, I. S. Bikit, I. V. Aničin\* , J. M. Slivka, J. J. Hansman,  
N. M. Žikić-Todorović, E. Z. Varga, S. M. Ćurčić and J. M. Puzović\*  
*Department of Physics, Faculty of Sciences, University of Novi Sad,  
Serbia and Montenegro, e-mail: mrdjad@im.ns.ac.yu*  
\* *Faculty of Physics, University of Belgrade, Serbia and Montenegro*

Received: September 15, 2003

### Abstract

The background spectrum of the Gamma-X HPGe (GMX) ORTEC low background detector was measured without shielding, in a 25 cm thick Fe shielding and 12 cm thick Pb shielding. From the results of these measurements, the relative remaining background of the Fe and Pb shielding was calculated and compared. The design and the inner lining of the Pb shield is discussed. The background count rate in the 25 keV – 1800 keV energy interval was 1.7 counts per second for the iron shield, 1 count per second with the lead shield lined with copper and 0.9 counts per second for the lead shield lined with tin. The suppression of the post radon gamma-lines by means of nitrogen purging is discussed.

*Key words:* Gamma-spectrometry, low-level counting, detector shielding

## 1. Introduction

Environmental radioactivity coming from terrestrial sources (K, Ra, U) and from cosmic radiation are the main contributors to the background of low-level gamma-spectrometries. The sources of background might be located inside the detector itself, in the shielding material and in the surrounding building. The cosmic radiation produces high energy muons which can be stopped only by very thick layers of material deep underground [1]. Active guard detectors can suppress the muon contribution also on the surface. Most frequently the detectors are shielded by lead or iron. Lead shielding against gamma-rays is very convenient because of high  $Z$  and high density but the neutron induced reactions are more frequent in this material than in Fe [2]. Some activity of  $^{210}\text{Pb}$  is always present even in the purest lead. Iron shieldings must have larger volumes than the lead ones and usually are produced from pre Second World War cast iron not containing fission products and  $^{60}\text{Co}$  used in contemporary steel production.

## 2. The Fe and Pb shields of the Nuclear Physics group in Novi Sad

The first low-level shielding of the laboratory is the 1 m<sup>3</sup> useful volume general purpose iron shield completed at the beginning of 1984. To eliminate as much as possible of

environmental background radiation, pre WWII cast steel plates from an old ship were used for the walls construction, because it contains minimum natural and virtually no man made radionuclides. Such a large protected volume has some long term advantages over shields usually built to protect only the detector crystal: it can accommodate detectors together with their Dewar vessels and cryostats of various size and shape, while it still allows for the detector crystal to be equipped with some passive or active additional shielding. There are also some drawbacks: the detector is not shielded against the activity of the Dewar vessel and the large volume of the chamber contains a significant amount of air with radioactive radon gas which increases the background count rate [3]. With its 25 cm thick walls and two doors for fast sample exchange this shielding was the herald of a large number of post Chernobyl environmental sample measurements. Later a NaI(Tl) guard detector was assembled in this shield [4] and a Compton suppression and gamma-gamma coincidence system was developed. The first tests of the low-level GMX detector equipped with HJ (bucket type) cryostat were performed in this shield. It was soon realized that the full background advantages of this detector can be exploited only with the specially designed low-level shield. The scheme of this lead shield is presented in Fig. 1. The dashed lines show the borders of the detachable parts. An oversized lead thickness of 12 cm is used having in mind the later addition of an anti-muon veto detector. The old lead was purified during the casting of the parts of the shield. The shield was tested with two inner lining materials Cu and Sn. The small inner volume of the shield could be purged with nitrogen evaporating in the Dewar vessel.

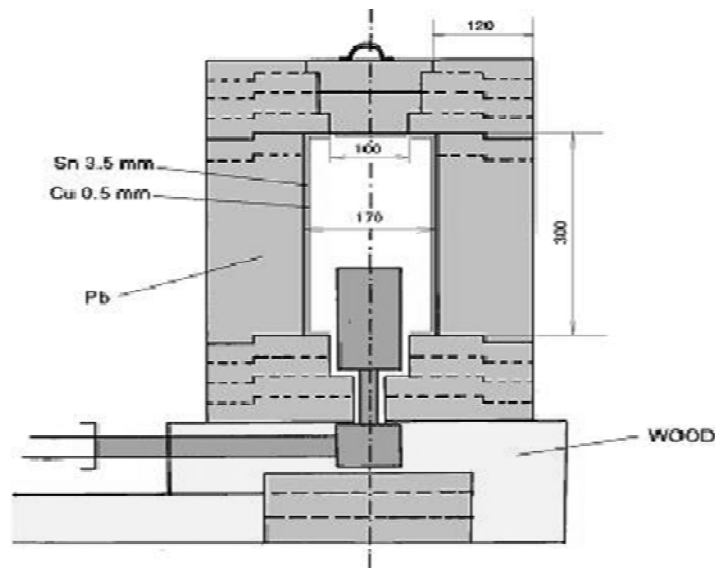


**Figure 1.** The scheme of the lead shield.

Both shields are located at the ground floor in the building of the Department of Physics.

### 3. Experimental results and discussion

The spectrum of the bare GMX detector is presented in Fig 2. In all the spectrums the numbers on the vertical axes represent counts/100 ks, while the numbers on the horizontal axes are the gamma-line energies in keV.

In Fig 3. the spectrum of the GMX detector shielded by iron is presented.

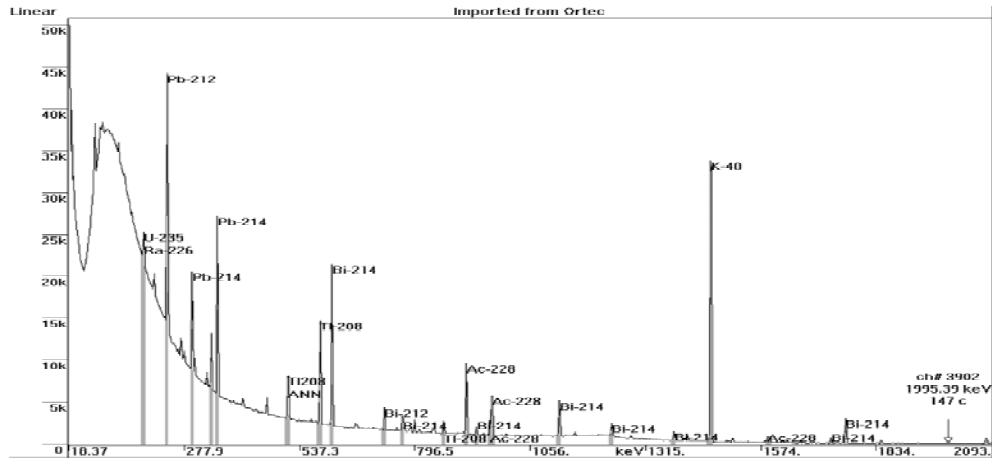


**Figure 2.** The spectrum of bare GMX detector.

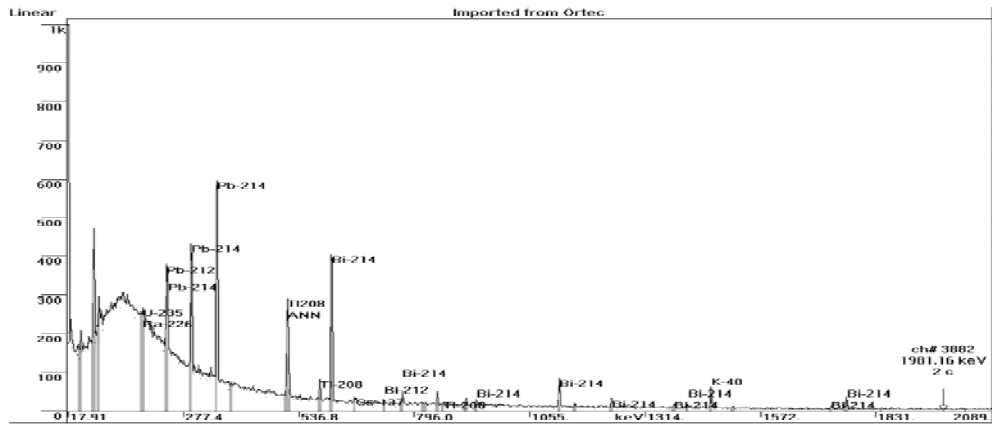


**Figure 3.** The spectrum of the GMX detector in an iron shield.

The relative remaining background factor ( $I_{Fe}/I_0$ ) is presented in the second column of Table 1. The intensity of transmitted radiation for most lines is about 1 %. The attenuation factors of post radon  $^{214}\text{Pb}$  and  $^{214}\text{Bi}$  lines show the presence of radon inside the iron chamber. The 511 keV annihilation line is reduced less than the other environmental background lines due to its cosmic origin. The intensities of the gamma-rays of  $^{228}\text{Ac}$  from the  $^{232}\text{Th}$  natural chain are most strongly reduced. In the spectrum measured inside the iron shield for 175 ks, no traces of neutron induced gamma-rays in germanium are found.

Column three of Table 1. presents the remaining background factor for the lead shield without any inner lining and no nitrogen inlet. The lead  $K_\alpha$  has about three times larger intensity than in iron, as is expected. The  $^{228}\text{Ac}$  gamma-rays are below the detection limits while the 511 keV annihilation line has roughly the same intensity as in iron. The 661 keV line of  $^{137}\text{Cs}$  is also not visible. The post radon lines of  $^{214}\text{Bi}$  and  $^{214}\text{Pb}$  are relative to the iron reduced almost by an order of magnitude. This is a consequence of the smaller inner volume of the Pb shielding assembly. The effect of the lining of the Pb

**Table 1.** Relative remaining background factors for various shielding configurations ( $I_0$  - bare detector,  $I_{Fe}$  - detector shielded with iron,  $I_{Pb}$  - detector shielded with Pb without lining,  $I_{PbCuN_2}$  - the detector shielded with Pb lined with Cu and flushed by  $N_2$ ,  $I_{Sn}$  - the detector shielded with Pb lined with Sn and copper and flushed with  $N_2$ ).

$E$ [keV]/ ISOTOPE	$I_{Fe}/I_0$ [%]	$I_{Pb}/I_0$ [%]	$I_{PbCuN_2}/I_0$ [%]	$I_{Sn}/I_0$ [%]
50-1800	0.96	0.55	0.57	0.52
100-120	0.68	0.21	0.30	0.22
200-220	1.06	0.43	0.56	0.46
360-380	1.24	0.79	0.87	0.84
540-560	1.06	0.86	0.85	0.87
730-750	1.08	1.04	1.10	1.07
880-900	1.16	1.22	1.11	1.15
1160-1180	1.01	0.99	0.90	1.01
1350-1370	1.60	1.66	1.41	1.58
1700-1720	2.84	3.24	3.14	3.00
72.8 Pb- $K_\alpha$	2.74	8.97	<0.93	<0.40
129.1 $^{228}\text{Ac}$	<3.56	<0.90	<1.83	<0.74
186.1 $^{226}\text{Ra}$ , 185.7 $^{235}\text{U}$	1.19	<0.38	<1.09	<0.61
209.3 $^{228}\text{Ac}$	<2.09	<0.50	<1.04	<0.56
238.6 $^{212}\text{Pb}$	0.76	0.10	0.10	0.06
295.2 $^{214}\text{Pb}$	2.86	0.31	<0.25	<0.11
351.9 $^{214}\text{Pb}$	2.54	0.33	<0.13	<0.05
511 ANN	7.69	6.19	5.01	5.49
583.2 $^{208}\text{Tl}$	0.38	<0.11	0.13	0.05
609.3 $^{214}\text{Bi}$	2.00	0.18	<0.08	0.09
661.6 $^{137}\text{Cs}$	1.76	<1.48	<1.70	<1.2
768.4 $^{214}\text{Bi}$	1.15	<0.45	<0.48	<0.32
911.2 $^{228}\text{Ac}$	0.29	<0.10	<0.10	<0.05
969.0 $^{228}\text{Ac}$	<0.31	<0.17	<0.18	<0.07
1120.4 $^{214}\text{Bi}$	1.41	0.15	0.11	<0.10
1460.8 $^{40}\text{K}$	0.13	0.11	0.08	0.09
1764.6 $^{214}\text{Bi}$	1.11	0.19	<0.10	0.10

shield with 1 cm of copper is presented in column four Table 1. Of course the lead x-rays are completely absorbed by the copper. On the other hand, the continuum below 511 keV increased significantly. The intensity of 511 keV gamma-ray is slightly reduced. Due to the flushing effect of nitrogen, the post radon lines disappeared from the spectra. In order to reduce the enhanced Compton scattering of the 511 keV gamma-rays on copper, it was decided to redesign the inner lining of the Pb chamber. Monte-Carlo calculations have been performed in order to select the most appropriate material and the optimal thickness. It was found that Sn is more appropriate than the most frequently used Cd. The optimal thickness of Sn is found to be 3.5 mm. The Sn x-rays are reduced by 0.5 mm Cu. The spectrum of the GMX detector in the Pb shield lined with Sn and Cu flushed by nitrogen is presented in Fig. 4.

As can be already visually noticed by a comparison of Fig 3. and Fig 4., the most

significant background lines in the iron shield almost disappeared in the lead shield. The most dominant line in the Pb spectrum is the 511 keV annihilation line. More quantitatively the difference between the copper and tin lining can be seen by comparing columns four and five. The continuum below 511 keV is less intensive with Sn lining but it is still higher than in unlined Pb. In the one mega second recording time Sn spectrum, almost all strong background disappeared except the 511 keV line with intensity about 10 % above the value recorded with the Cu line. The significant difference between the continuum with copper and tin lining is best seen in Fig 5.

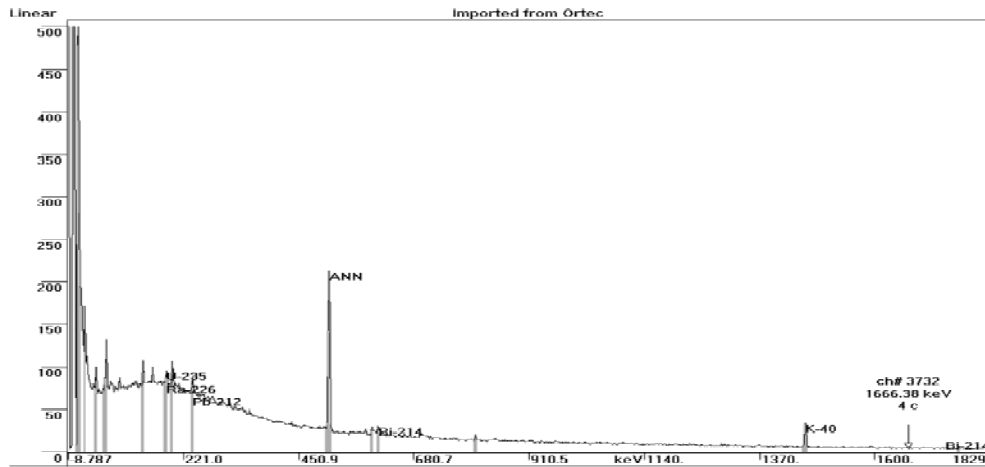


**Figure 4.** The spectrum of the GMX detector in the lead shield lined with Sn and Cu and flushed with liquid nitrogen measured for 1.08 Ms.

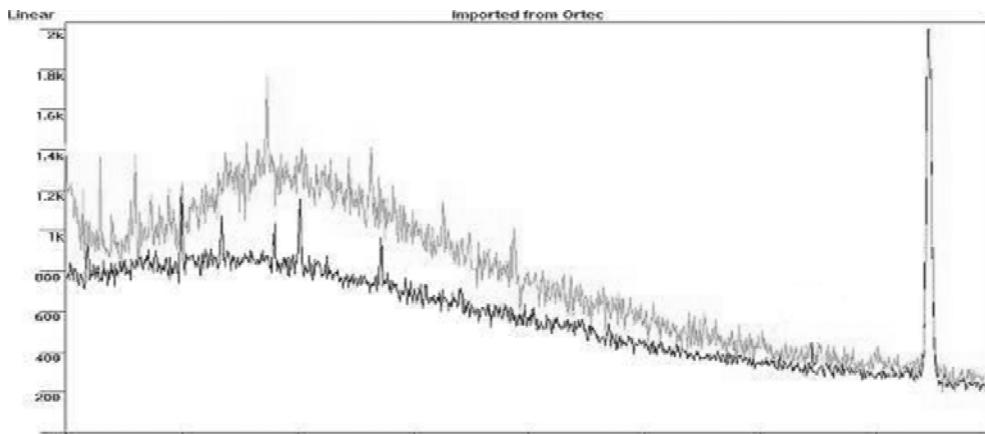


**Figure 5.** Comparison of the spectral region below 511 keV for copper (upper curve) and tin (lower curve) lining.

#### 4. Conclusions

The new design lead shield for the HJ cryostat low background GMX detector exhibited very good performances. It seems that the shielding material (lead and tin) purchased in local stores was a lucky choice. No traces of any contamination in the shielding materials were found. In the low energy region, some weak gamma-lines mainly from neutron

induced reactions on germanium were found. The list of these lines together with the 46.6 keV  $^{210}\text{Pb}$  gamma-line, the only recorded natural radioactive contaminant of lead, is presented in Table 2.

**Table 2.** Low energy weak gamma-lines in the spectrum of GMX shielded by Pb lined with Sn and Cu.

$E_\gamma$ [keV]	NUCLIDE	$I$ [c/ks]
23.8	$^{71}\text{Ge}$	$1.16\pm 0.12$
46.6	$^{210}\text{Pb}$	$0.89\pm 0.13$
66.5	$^{73m}\text{Ge}$	$1.55\pm 0.13$
139.7	$^{75m}\text{Ge}$	$0.42\pm 0.12$
159.4	$^{77m}\text{Ge}$	$0.49\pm 0.18$
198.5	$^{71}\text{Ge}$	$0.54\pm 0.14$

As mentioned earlier the oversized lead thickness probably enhances the 511 keV line intensity and the continuum below 511 keV. These components of the background can be reduced by the additional cosmic ray veto shield. We hope that with this addition our low-level gamma-spectroscopy system will be able to compete with shallow underground laboratories [5].

## Acknowledgments

The authors acknowledge the financial support of the Ministry of Science, Technology and Development of Serbia, as part of the project Nuclear Spectroscopy and Rare Processes (No 1859).

## References

1. J. M. Puzović and I. V. Aničin, Nucl. Instr. And Meth. A **480**, 565 (2002).
2. G. Heusser, Nul. Instr. Ans. Meth. A **369**, 539 (1996).
3. I. Bikit, L. Marinkov, M. Vesković, XXVIII Yug. Conf. of ETAN, Split, Yugoslavia, ETAN VI, p.51 (1984).
4. I. Bikit, J. Slivka, M. Krmar, Z. Djurčić, N. Žikić, Lj. Čonkić, M. Vesković, I. Aničin, Nucl. Instr. and Meth. In Phys. Res. A **421**, 266 (1999).
5. G. Heusser, Annu. Rev. Nucl. Part. Sci. **45**, 543 (1995).

## Calibration of GMX HPGe Detector with NBS Reference Source

E. Z. Varga, I. S. Bikit, J. M. Slivka, N. M. Žikić-Todorović,  
D. S. Mrđa, S. M. Ćurčić and M. J. Vesković  
*Department of Physics, Faculty of Sciences, University of Novi Sad,  
Trg Dositeja Obradovića 4, 21000 Novi Sad, Serbia and Montenegro,  
e-mail: ester@im.ns.ac.yu*

Received: September 16, 2003

### Abstract

Efficiency determination of high-resolution semiconductor gamma-spectrometers for voluminous samples is not simple. Computing methods for determination of the efficiency for voluminous samples using measured values for point sources are commercially available, but the systematic error for this method might be significant. The reference material NBS SRM 4350B was developed in the National Bureau of Standards a long time ago. This natural material is analyzed by the manufacturer for 8 declared radionuclides whose concentration was determined by mass spectrometry. In this paper the present features of this material are investigated and the applicability as a national reference material is discussed.

*Key words:* Efficiency, gamma-spectrometry, reference material, radionuclides

### 1. Introduction

High purity germanium spectrometers are the basic tool for determination of radioisotope concentration due to their excellent resolution. However, when absolute results are needed the efficiency calibration still presents a significant problem [1].

These detectors are not uniform like NaI(Tl) crystals and the frequently not well known construction details limit the reliability of the Monte Carlo [2] and other semi empirical numerical calibration methods [3]. Thus these detectors are today most safely calibrated by spiked voluminous radioactive samples. Usually the activities of the spiked radionuclides in these materials are determined only by nuclear spectroscopic methods, i.e. by measuring by means of calibrated detectors. This means that the reported activity of the certified radioactive material is affected by the calibration errors of the primary detector. Therefore, the reference materials which are analyzed by chemical methods like mass spectroscopy have definite metrological advantages. As far as we know the NBS SRM 4350B reference material is one of the rare examples of calibration materials prepared in this manner. Of course, since the date of production 9th September 1981 some of the activity in this material is decayed. In the present paper we investigate the applicability of this material as a primary metrological standard today.

The Standard Reference Material (SRM) is pulverized river sediment [4]. The material has been tested to a minimum sample size of 5 grams, for which it has been found to be homogenous. Random and systematic uncertainties have been combined in quadrature at a level corresponding to a standard deviation of the mean, the stated overall uncertainties are 3 times this value and are roughly at the 99 % confidence level.

The mass spectrometry data are presented in Table 1.

**Table 1.** SRM mass spectrometry data.

radionuclide	activity concentration [Bq/g]	total uncertainty [%]	half-life [y]
$^{60}\text{Co}$	$4.64 \times 10^{-3}$	5.0	5.28
$^{137}\text{Cs}$	$2.90 \times 10^{-2}$	6.3	30.07
$^{152}\text{Eu}$	$3.05 \times 10^{-2}$	4.0	13.54
$^{154}\text{Eu}$	$3.78 \times 10^{-3}$	15	8.48
$^{226}\text{Ra}$	$3.58 \times 10^{-2}$	10	1600
$^{241}\text{Am}$	$1.5 \times 10^{-4}$	21	432.2
$^{40}\text{K}$	$5.6 \times 10^{-1}$	9	$1.277 \times 10^9$
$^{232}\text{Th}$	$3.32 \times 10^{-2}$	11	$1.405 \times 10^{10}$
$^{235}\text{U}$	$1.7 \times 10^{-3}$	9	$7.038 \times 10^8$
$^{238}\text{U}$	$3.08 \times 10^{-2}$	10	$4.468 \times 10^9$

## 2. Experimental technique and results

The 201.4 gram NBS SRM 4350B sample was measured on the GMX type HPGe spectrometer with nominal efficiency 36 % and resolution less than 2 keV. The detection assembly was shielded by a 12 cm thick lead shield. The material was placed in an  $\Phi = 67$  mm and  $h = 62$  mm plastic container. The container was hermetically sealed for one year before the measurement. Quite sufficient to ensure the radon equilibrium. The time of measurement was 131784 seconds. The results of the measurements are presented in Table 2.

The efficiency curve derived from these results is presented in Fig.1. The experimental data were fitted by the formula:

$$\ln E_f = a_1 - \left( (a_2 + a_3 \cdot e^{-a_4 E}) e^{-a_5 E} \right) \ln E, \quad \varepsilon = e^{\ln E_f} \quad (1)$$

Where  $\varepsilon$  is the detection efficiency,  $E$  is the gamma-ray energy, while  $a_1 - a_5$  are the fitted parameters.

From Fig. 1. one can easily see that due to the weakness of the gamma-lines below 200 keV the statistical error of the efficiency function at low energies is very poor. That drawback of the NBS SRM 4350B source was corrected by means of the  $\text{UO}_2(\text{NO}_3)_2 \times 6\text{H}_2\text{O}$  source diluted in a starch matrix. The relative efficiencies of the  $^{235}\text{U}$  and  $^{238}\text{U}$  lines are presented in Table 3.

**Table 2.** Results of measurements.

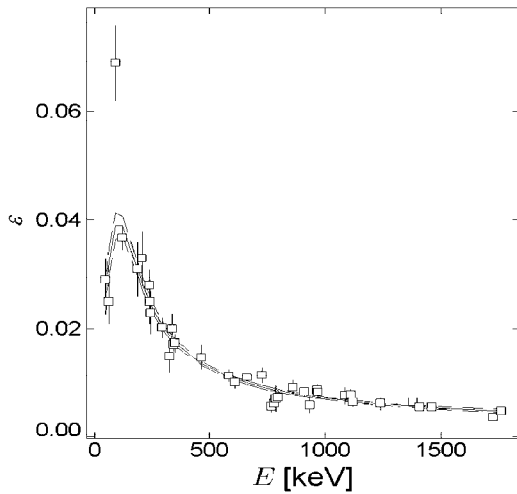
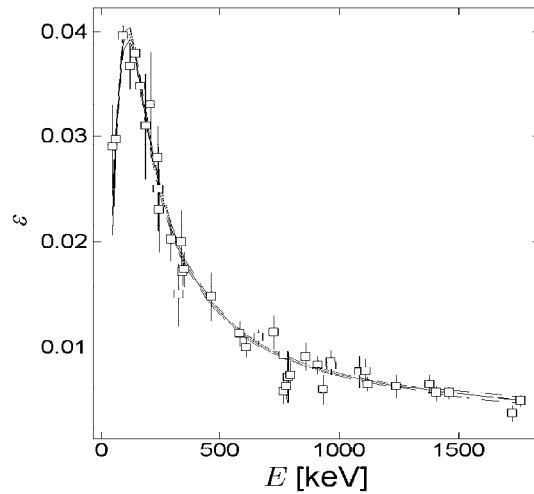
radionuclide	$\bar{E}$ [keV]	$p_\gamma$	$A$ [Bq]	$N$	$s(N)$
Pb 210	46.539	0.0425	7.2(7)	1181	125
Th 234	63.290	0.0484	6.2(6)	1004	119
Th 234 D	92.600	0.0516	6.2(6)	2896	126
Eu 152	121.783	0.2842	2.0(8)	2823	132
Ra 226 D	185.700	0.0350	6.7(7)	1745	123
U 235 D	186.100	0.5750	0.34(3)	1745	123
Ac 228	209.253	0.0388	6.7(7)	1128	111
Pb 212	238.632	0.4330	6.7(7)	10738	142
Ra 224 D	240.987	0.0397	6.7(7)	2671	87
Pb 214 D	241.981	0.0750	7.2(7)	2671	87
Eu 152	244.699	0.0749	2.05(8)	463	76
Pb 214	295.213	0.1850	7.2(7)	3554	95
Ac 228	327.995	0.0295	6.7(7)	382	69
Ra 223 D	338.280	0.0279	0.34(3)	1951	82
Ac 228 D	338.322	0.1125	6.7(7)	1951	82
Eu 152	344.281	0.2658	2.05(8)	1230	74
Pb 214	351.921	0.3580	7.2(7)	5929	107
Ac 228	463.095	0.0444	6.7(7)	580	66
Tl 208	583.191	0.8448	2.41(25)	3035	79
Bi 214	609.312	0.4479	7.2(7)	4240	83
Cs 137	661.660	0.8510	3.57(22)	4401	89
Bi 212	727330	0.0658	6.7(7)	661	58
Bi 214	768.356	0.0480	7.2(7)	258	46
Eu 152	778.903	0.1296	2.05(8)	217	44
Bi 212 T	785.370	0.0110	6.7(7)	147	43
Pb 214 T	785.910	0.0085	7.2(7)	147	43
Bi 214 T	786.100	0.0030	7.2(7)	147	43
Ac 228	794.947	0.0434	6.7(7)	278	42
Tl 208	860.564	0.1240	2.41(25)	357	42
Ac 228	911.020	0.2660	6.7(7)	1948	62
Bi 214	934.061	0.0303	7.2(7)	171	37
Eu 152 D	964.131	0.1433	2.05(8)	717	42
Ac 228 D	964.770	0.0511	6.7(7)	717	42
Ac 228	968.971	0.1617	6.7(7)	1167	50
Eu 152	1085.914	0.0991	2.05(8)	203	44
Eu 152	1112.116	0.1354	2.05(8)	283	44
Bi 214	1120.787	0.1480	7.2(7)	898	52
Bi 214	1238.110	0.0586	7.2(7)	345	53
Bi 214	1377.669	0.0392	7.2(7)	240	27
Bi 214 D	1407.980	0.0280	7.2(7)	467	33
Eu 152 D	1408.011	0.2087	2.05(8)	467	33
K 40	1460.830	0.1067	113(13)	8812	99
Bi 214	1729.595	0.0288	7.2(7)	102	19
Bi 214	1764.494	0.1536	7.2(7)	710	33

D – unresolved doublet, T – unresolved triplet,  $\bar{E}$  – gamma-ray energy,  $p_\gamma$  – absolute gamma-ray intensity,  $A$  – source activity,  $N$  – net counts in total absorption peak,  $s(N)$  – standard deviation of  $N$

**Table 3.** Relative efficiencies of the  $^{235}\text{U}$  and  $^{238}\text{U}$  gamma-lines.

U-238, Th-234		U-235	
$E$ [keV]	$\varepsilon_i/\varepsilon_{ref}$	$E$ [keV]	$\varepsilon_i/\varepsilon_{ref}$
63.3	3.24	143.8	1.124
92.6	5.06	163.3	1.096
766.6	1.32	205.3	1
1001.4	1		

The normalization to the 1001.4 keV and 205.3 keV was performed in order to get absolute detection efficiencies via the normalization to the efficiency curve in Fig. 1. Before this procedure the starch matrix was converted into the sediment matrix by means of the computer code OMEGA. The efficiency curve derived in this manner is presented in Fig. 2.

**Figure 1.** Efficiency curve obtained with NBS SRM 4350B.**Figure 2.** Efficiency curve obtained with uranyl-nitrate and NBS SRM 4350B.

### 3. Discussion and conclusions

The activity concentration of the radionuclides in the NBS SRM 4350B source is rather low thus the detector calibration is possible only in good quality shielding and might be lengthy. On the other hand, the weak source activity makes that random summing negligible as well as counting dead time. The data points are not corrected for true cascade summing. According to our estimation and the data of Michotte [5] the summing correction for the most strong cascade transitions is less than 1 %. Despite the about 10 % activity uncertainties of the certified radionuclides, the statistical error of the fitted curve is very good. Above 100 keV the error of the efficiency curve is about 2 % while at low energies it increases to 3 %. This error is bigger than the subpercent errors quoted in Ref. [6] obtained with kBq activity sources, but the possible systematic errors in Ref. [6] might be bigger than ours. Having in mind the general dependence of the relative counting error

on the mass ( $m$ ) and counting time ( $t$ ):

$$\frac{\Delta N}{N} \propto \frac{1}{\sqrt{m \cdot t}} \quad (2)$$

We can see that the statistical error of the efficiency curve can be improved by using longer counting periods. On the other hand the detector calibration for small voluminous sources ( $m \approx 10$  g) with the SRM source may need a very long counting.

All the presented data with the quoted limitations show that the SRM source can be safely adopted as a national standard for gamma-spectroscopy.

### Acknowledgments

The authors acknowledge the financial support of the Ministry of Science, Technology and Development of Serbia, as part of the project Nuclear Spectroscopy and Rare Processes (No 1859).

### References

1. H. L. Oczkowski, *Journal on Methods and Applications of Absolute Chronology* **20**, 31 (2001).
2. M. Garcia-Talavera, H. Nader, M. J. Daza, B. Quintana, *Applied Radiation and Isotopes* **53**, 777 (2000).
3. L. Moens, J. de Donder, Lin Xi-lei, F. de Corte, A. De Wiapelaere, A. Simonits, J. Hoste, *Nuclear Instruments and Methods* **187**, 451 (1981).
4. "Environmental Radioactivity", Standard Reference Material 4350B, National Bureau of Standards Certificate, Washington D.C. 20234 (1981).
5. C. Michotte: Efficiency calibration of the Ge(Li) detector of the BIPM for SIR-type ampoules, Rapport BIPM-99/3
6. J. C. Hardy et al., *Radiation Applications and Isotopes* **56**, 65 (2002).

## Effect of Self-Absorption in Voluminous Sources in Gamma-Spectrometry

S. Ćurčić, I. Bikit, J. Slivka, D. Mrđa, N. Žikić-Todorović, E. Varga, M. Vesković  
*Department of Physics, Faculty of Sciences, University of Novi Sad,  
Trg Dositeja Obradovića 4, 21000 Novi Sad, Serbia and Montenegro  
e-mail:bikit@im.ns.ac.yu*

Received: September 16, 2003

### Abstract

The detection efficiency for voluminous sources, typical for environmental radioactivity investigations, can not be exactly separated into intrinsic detector efficiency and self-absorption effect. The semi-empirical method developed by L. Moens et al. for efficiency calibration is tested by means of cylindrical sources with known matrix and activity. It is shown that the method works properly for cylindrical sources. Based on this conclusion, the self-absorption for various matrix cylindrical sources is evaluated by this method.

*Key words:* Gamma spectroscopy, self-absorption, voluminous sources

### 1. Introduction

Determination of absolute peak efficiency in gamma-spectrometry measurements with semiconductor detectors for given radiation energy and source geometry is a very difficult task. Generally, there are three different ways for solution of this problem:

1. The relative solution, where the source and standard are very similar. The results obtained are usually reliable, but the systematic error of the calibration sources might be questionable. Recent results using this method [1] quote sub-percent precision combining measurements with radioactive sources and Monte Carlo interpolation techniques.
2. The absolute solution, where the efficiency is determined by the Monte Carlo technique only [2]. In this approach the detector construction data with high precision are needed, together with the chemical composition of the source. The basic problem is the quality of the program (the minimal energy of photon-electron interaction in detector and its surrounding, values of the cross-section for some interactions, etc.). Due to all of these uncertainties this method still can not produce reliable absolute efficiency values.

3. Semi-empirical, which is a combination of measurements and estimations. The effective solid angle method, introduced in the beginning of the 80's [3,4], simultaneously takes into account the influence of gamma-attenuation, geometry of measurement and detector response.

Taking into account that in most practical measurements only a few fixed geometries are used, we propose a simple and accurate method, combining approaches 1. and 3. The detector efficiency in a given geometry (in our case a cylinder) is measured by a referent source, while the matrix (self-absorption effect for different samples) are corrected for by the method of the effective solid angle (our computer code OMEGA).

## 2. Methods and experiments

The concept of the effective solid angle relates the total efficiency  $\varepsilon_T$  to the effective solid angle  $\bar{\Omega}$  by

$$\varepsilon_T = \frac{\Omega}{4\pi} . \quad (1)$$

The needed total absorption peak efficiency  $\varepsilon_P$  is derived from the relation

$$\varepsilon_P = \frac{P}{T} \varepsilon_T , \quad (2)$$

where  $P/T$  is the "virtual" peak to total ratio, an intrinsic property of the bare detector which can not be measured. This problem is solved by introducing relative total absorption peak efficiencies

$$\varepsilon_{P,X} = \varepsilon_{P,R} \left( \frac{\bar{\Omega}_X}{\bar{\Omega}_R} \right) , \quad (3)$$

where the  $(\bar{\Omega}_X/\bar{\Omega}_R)$  ratio is calculated numerically. Assuming that the intrinsic  $P/T$  ratio is not dependent on source geometry,  $\varepsilon_{P,R}$  is measured by point sources. It seems plausible that using voluminous reference sources, the accuracy of the method can be better tested.

In order to test this assumption, the  $125 \pm 12$  p.p.m  $^{235}\text{U}$  content natural phosphate sample is measured in  $\Phi = 67$  mm cylindrical containers with heights 7, 15 and 31 mm. The measurements were done by means of a 36 % nominal efficiency GMX type detector in a low background shield.

The errors of the experimental efficiency ratios listed in Table 1. depend only on counting statistics and do not exceed 1 %, sufficient for the testing of the solid angle concept. The relative deviations in Table 1. are defined as

$$\Delta = \frac{EXP - OMEGA}{EXP} (\%) . \quad (4)$$

In Fig 1. and 2. the experimental and semi empirical efficiency ratios are compared. The general shapes of the curves are similar, but some differences at the low energy region can be noticed visually. More quantitative the experimental and semi empirical efficiency ratios are compared in Table 1.

**Table 1.** Comparative table of measured and calculated efficiency ratios ( $\varepsilon_{15}/\varepsilon_{31}$  is the efficiency ratio for cylinders of diameter 67 mm, and heights 15 mm, 31 mm respectively, a  $\varepsilon_7/\varepsilon_{31}$  is the efficiency ratio for cylinders of diameter 67 mm, and heights 7 mm, 31 mm respectively).

$E_\gamma$ [keV]	$\varepsilon_{15}/\varepsilon_{31}$ (exp.)	$\varepsilon_{15}/\varepsilon_{31}$ (omega)	$\Delta$ [%]	$E_\gamma$ [keV]	$\varepsilon_7/\varepsilon_{31}$ (exp.)	$\varepsilon_7/\varepsilon_{31}$ (omega)	$\Delta$ [%]
40	1.65385	1.72836	-4.51	40	2.73077	2.94687	-7.91
45	1.61972	1.66432	-2.75	45	2.5704	2.65117	-3.14
50	1.58065	1.60196	-1.35	50	2.45161	2.42157	+1.22
55	1.54303	1.54889	-0.38	55	2.31454	2.25214	+2.70
60	1.51099	1.50776	+0.21	60	2.22527	2.12748	+4.39
70	1.45238	1.4502	+0.15	70	2.04762	1.96398	+4.08
80	1.41304	1.41244	+0.04	80	1.95652	1.8684	+4.50
90	1.40816	1.38902	+1.36	90	1.87755	1.80866	+3.67
100	1.39216	1.3744	+1.27	100	1.80392	1.77141	+1.80
110	1.38462	1.36095	+1.71	110	1.76923	1.7413	+1.58
120	1.36538	1.35301	+0.91	120	1.73077	1.72019	+0.61
130	1.34615	1.34597	+0.01	130	1.67308	1.70474	-1.89
140	1.35294	1.34088	+0.89	140	1.66667	1.69261	-1.56
160	1.34737	1.33172	+1.16	160	1.64211	1.67215	-1.83
180	1.34396	1.32595	+1.34	180	1.61731	1.65756	-2.49
200	1.34577	1.3196	+1.94	200	1.61692	1.64432	-1.69
250	1.34154	1.30928	+2.40	250	1.60308	1.62075	-1.10
300	1.33829	1.30263	+2.66	300	1.59851	1.60461	-0.38
350	1.33188	1.29625	+2.67	350	1.59389	1.59102	+0.18
400	1.325	1.29252	+2.45	400	1.585	1.58095	+0.26
500	1.31677	1.28452	+2.45	500	1.57764	1.56499	+0.80
600	1.30882	1.27738	+2.40	600	1.56618	1.55007	+1.03
700	1.29167	1.27286	+1.46	700	1.55	1.53962	+0.67
800	1.28704	1.26923	+1.38	800	1.53704	1.53047	+0.43
1000	1.26882	1.26227	+0.52	1000	1.51613	1.51626	-0.01
1200	1.26492	1.25714	+0.62	1200	1.49165	1.5054	-0.92
1400	1.25159	1.25368	-0.17	1400	1.47014	1.49656	-1.80
1600	1.24142	1.24874	-0.59	1600	1.44855	1.48773	-2.70

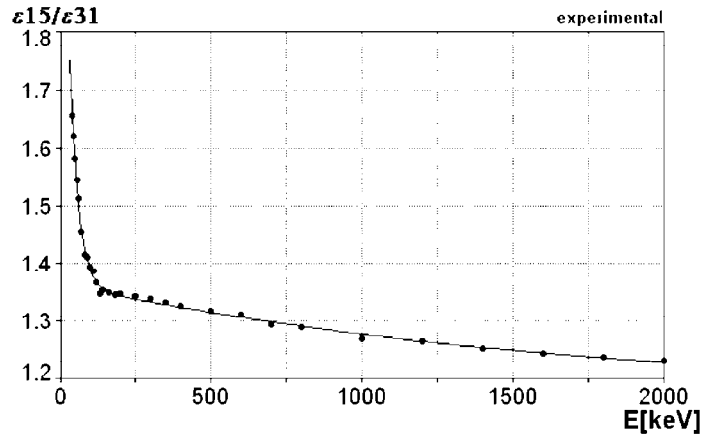


**Figure 1.** Experimentally determined efficiency ratio for the cylindrical geometry diameter of 67 mm, and heights 15 mm and 31 mm.

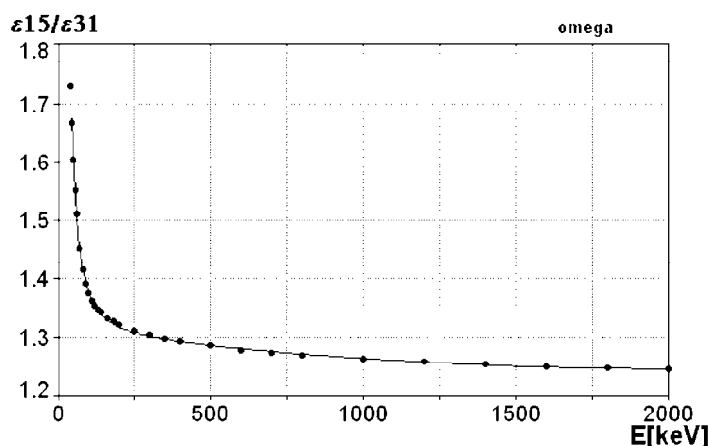


**Figure 2.** Efficiency ratio for the cylindrical geometry diameter of 67 mm, and heights 15 mm and 31 mm, calculated by program OMEGA.

### 3. Discussion and conclusions

At first, when we compare the deviations obtained with the data of Ref.[5] we can notice that our values are much smaller. This means that our assumption on the improvement of the semi-empirical method by using voluminous referent sources is fully justified. Instead of more than 30 % deviations at energies below 1000 keV, we measured only 4.5 % deviations at 40 keV. We agree with Ref.[5] that the method of effective solid angle overestimates the detection efficiency at low energy. In the energy range 200 – 600 keV the source of the discrepancy between the measured and calculated values for the first set of results is not very clear.

Nevertheless, the semi-empirical method can be safely used for self-absorption corrections for different matrix samples in same the geometry. The example of such a calculation is presented in Fig. 3.

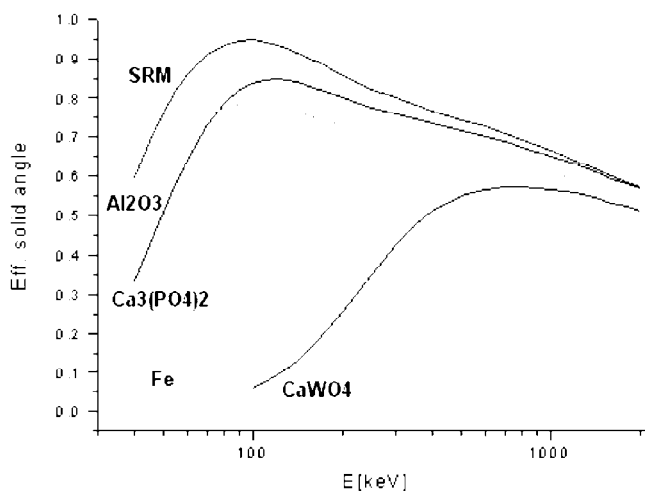


**Figure 3.** The effective solid angle for different composition sources with volume of  $\Phi = 67$  mm,  $h = 31$  mm. (SRM-NBS reference sediment sample).

Having in mind that the effective solid angle is proportional to the absolute detection efficiency, we can first see from Fig. 3. that the self-absorption effects may be significant even for different low  $Z$  materials below 100 keV. The difference between the efficiencies for the sediment SRM,  $\text{Al}_2\text{O}_3$  and  $\text{Ca}_3(\text{PO}_4)_2$  in this energy region is about 20 %. This difference drops to below 10 % above 1 MeV. The self- absorption effects in high  $Z$  and highly dense materials are of course much more pronounced.

### Acknowledgments

The authors acknowledge the financial support of the Ministry of Science, Technology and Development of Serbia, as part of the project Nuclear Spectroscopy and Rare Processes (No 1859).

### References

1. J. C. Hardy et al., Radiation Applications and Isotopes **56**, 65 (2002).
2. J. M. Puzović, I. V. Aničin, Nuclear Instruments and Methods **414**, 279 (1998).
3. L. Moens, J. De Donder, Lin Xi-lei, F. De Corte, A. De Wispelaer, A. Simontis and J. Hoste, Nuclear Instruments and Methods **187**, 451 (1981).
4. S. Jovanović, A. Dlabac, N. Mihaljević, P. Vukotić, XIX Symposium JDZZ, Petrovac, Yugoslavia, p. 127 (1997).
5. P. Vukotić, S. Dapčević, S. Jovanović, Ionizing Radiation Nature (Monograph), Vinča Institute, p. 299 (1995).

## Study of the Broadening Mechanisms in Plasma of Wall Stabilized Electric Arc

S. Hamzaoui\*, S. Djurović, M. Ćirišan and Z. Ben Lakhdar\*  
*Department of Physics, Faculty of Science, University of Novi Sad,  
Trg Dositeja Obradovića 4., 21000 Novi Sad, Serbia and Montenegro;  
Laboratory of atomic and molecular spectroscopy and applications,  
Faculty of Sciences of Tunis, Campus University 1060, Tunis*

Received: February 20, 2004

### Abstract

Subject of this work is analysis of different pressure broadening mechanisms contribution to the spectral line widths and shifts. For present plasma conditions, Stark broadening is dominant, while van der Waals broadening is not negligible. Resonant broadening is order of magnitude smaller than Van der Waals broadening. Natural broadening for this plasma conditions is completely negligible while instrumental and Doppler broadening should always be taken into account. Contribution of mentioned broadening mechanisms is considered for three neutral argon spectral lines, for electron densities from  $0.74 \cdot 10^{22} \text{ m}^{-3}$  to  $2.9 \cdot 10^{22} \text{ m}^{-3}$  and temperatures from 9300 K to 10800 K.

*Key words:* Spectral line, pressure broadening, Doppler broadening, instrumental broadening

### 1. Introduction

Spectral lines always have certain profiles, i.e. a definite distribution of the radiation intensities in a given range of wavelengths (frequencies), and therefore, have a finite width. The line shape and width depend upon the type of emitter and the physical conditions under which emitter exists, as well as upon characteristics of the used spectral apparatus.

Broadening mechanisms of spectral lines of atoms and ions in plasma can be divided in three groups: i) Natural broadening, caused by finite average lifetime of atoms in excited state, ii) Doppler broadening, due to motion of the emitter atoms with respect to the observation system, and iii) Pressure broadening, caused by the interaction of the emitters with the neutral and charged particles [1].

Spectral line profiles provide a lot of information about the plasma conditions, such as concentration of neutral and charged particles and their temperatures. Experimentally obtained data are of great importance for plasma diagnostic, theory testing and the different plasma applications.

The aim of this paper is to separate different broadening mechanisms and make comparison between their contributions. The contribution of each mentioned broadening mechanism is considered for three neutral argon spectral lines, emitted from wall stabilized arc plasma, for electron densities from  $0.74 \cdot 10^{22} \text{ m}^{-3}$  to  $2.9 \cdot 10^{22} \text{ m}^{-3}$  and temperatures from 9300 K to 10800 K.

## 2. Spectral line broadening

### 2.1 Natural broadening

From the quantum mechanics point of view, the natural line width is a consequence of the energy uncertainty of stationary atomic states. This uncertainty is given by the well known Heisenberg relation.

$$\Delta\nu \approx \frac{1}{2\pi} \left( \frac{1}{\tau_n} + \frac{1}{\tau_m} \right) \quad (1)$$

For example for Ar I 425.936 nm,  $\Delta\nu \approx 6.6 \cdot 10^5 \text{ s}^{-1}$ . Transition probabilities ( $1/\tau$ ) are taken from [2]. So conversion to wavelength gives natural halfwidth  $w_N \approx 4 \cdot 10^{-7} \text{ nm}$ .

### 2.2 Doppler broadening

Excited atoms and ions as radiation sources in plasma are in the state of permanent motion. This can be thermal motion, motion due to turbulence or motion of either the whole plasma or its part with respect to the observer. Thus, Doppler effect arises. The distribution of radiation intensities against the wavelengths due to Doppler effect is of the Gaussian type [1] and the Doppler line halfwidth can be calculated as:

$$w_D = 7.162 \cdot 10^{-7} \lambda_0 \left( \frac{T}{M} \right)^{1/2} \quad (2)$$

where  $T$  is expressed in K and  $M$  in atomic mass units.

### 2.3 Pressure broadening

Spectral line broadening caused by the interaction of emitters with surrounding particles (perturbers), depends on the concentration of these particles and is called pressure broadening. Depending on the type of emitter - perturber interaction this broadening may be either: a) Resonance broadening, if the emitter interacts with the perturber of the same type, b) Van der Waals broadening, if the interaction with neutral particles is involved, or c) Stark broadening, when the perturbers are charged particles, electron and ions. Stark and van der Waals effects also cause the shift of the spectral lines [1]. Under real conditions, these broadening mechanisms act simultaneously.

#### 2.3a Resonance broadening

Resonance broadening appears when either the upper or the lower level of the observed transition has the allowed dipole transition to the ground state and when the emitter is surrounded by similar atoms in the ground state. Starting from the Baranger [3] and Griem et al. [4] theories, Griem [1] derived an expression for the spectral line width due to dipol-dipol interaction with the ground level of the same sort of atoms. Later, Ali and Griem [5, 6] corrected this expression and obtained the following equation for the half-halfwidth due to resonance broadening:

$$\omega_R = 1.92\pi \left( \frac{g_1}{g_R} \right)^{1/2} \frac{Ne^2 f_R}{m\omega'} \quad (3)$$

where  $g_1$  and  $g_R$  are the statistical weights of the ground and excited levels,  $N$  density of perturbed particles,  $f_R$  the oscillator strength,  $m$  the electron mass and  $\omega'$  the corresponding angular frequency. Resonance broadening may be caused by atoms and ions of another kind whose energy levels are close to the corresponding atomic level of the emitter. In terms of wavelengths, the above expression for the resonance half- halfwidth assumes the form:

$$w_R = 4.30 \cdot 10^{-14} \left( \frac{g_1}{g_R} \right)^{1/2} \lambda^2 \lambda_R f_R N \quad (4)$$

### 2.3b Van der Waals broadening

The forces by which neutral atoms are interacting with emitter atoms are of short-range type. The position of the considered level of the emitter atom depends on the emitter-perturber distance. Averaging over all the possible distances between the emitters and neutral perturbers results in broadening of the spectral lines. The intensity maximum of the line will be shifted in comparison to the line maximum radiation of the unperturbed atom and it will appear at the wavelength corresponding to the most probable distance between the emitter and perturber.

Griem [1] estimated the van der Waals half-halfwidth, which may be written in the following form [7]:

$$\omega_V = \pi \left( \frac{4\pi}{3} \right)^{4/5} C^{2/5} \bar{v}^{3/5} N \quad (5)$$

where  $\bar{v}$  is the average relative velocity of colliding atoms,  $N$  is the perturber density.  $C$  is the difference of the van der Waals constants for the upper and lower level:

$$C = C_i - C_f; \quad C_i = \bar{\alpha} \frac{e^2 a_0^2}{h} \bar{R}_i^2 \quad (6)$$

The quantity  $\bar{\alpha}$  is the average polarizability of neutral perturbers, expressed as [1, 8]:

$$\bar{\alpha} = \frac{9}{2} a_0^3 \left( \frac{3E_H}{4E_{2p}} \right)^2 \quad (7)$$

where  $a_0$  is the Bohr radius,  $E_H$  the ionization energy of hydrogen atom,  $E_{2p}$  the energy of first excitation level of the perturber. In (6)  $\bar{R}_i^2$  denotes the square of the position vector of the excited electron, which in a Coulombic approximation is:

$$\bar{R}_i^2 = \frac{n_i^{*2}}{2} \left[ 5n_i^{*2} + 1 - 3l_i(l_i + 1) \right] \quad (8)$$

where  $l_i$  is the corresponding orbital quantum number and  $n_i^*$  the effective quantum number:

$$n_i^* = \left( \frac{E_H}{E_I - E_i} \right)^{1/2} \quad (9)$$

$E_I$  is the emitter's ionization energy and  $E_i$  is the energy of the considered level of the emitter atom. In terms of wavelength the van der Waals half-halfwidth can be expressed as [7]:

$$w_V = 4.09 \cdot 10^{-12} \lambda^2 (\bar{\alpha} \bar{R}_i^2)^{2/5} \left( \frac{T}{\mu} \right)^{3/10} N \quad (10)$$

where  $\mu$  is the reduced mass of the emitter-perturber system, and

$$\bar{R}^2 = \bar{R}_i^2 - \bar{R}_f^2 \quad (11)$$

Van der Waals shift can be estimated as [1]:

$$d_V = -\frac{2}{3}w_V \quad (12)$$

### 2.3c Stark broadening

Stark broadening is observed as a change in atomic energy level positions under the influence of electric field. In plasma, this is the electric microfield created by the electrons and ions. Radiation of particular atoms consists of the lines shifted and split into components, but in contrast to a static electric field, the electric microfield in plasma is changing in space and time, and these changes are different for the various atoms. So, the result of this effect are the spectral lines which are broadened and shifted.

So-called linear Stark effect is characteristic for the hydrogen atom and hydrogen-like ions. Namely, the amount of energy by which a given energy level of an atom in electric field is shifted is proportional to the strength of this field. In the case of nonhydrogenic atoms there is a quadratic dependence between the additional energy and electric field intensity, that is the quadratic Stark effect. After appearance of the works of Baranger [9 - 11] and Kolb and Griem [12], the Stark broadening of spectral lines has become a subject of numerous theoretical and experimental papers.

In the present work we are not going to deal with the classification and analysis of these works. There are several monographs and review articles devoted to the Stark broadening of spectral lines [1, 13 - 18], as well as critical reviews of experimental data [19 - 24]. The bibliography concerning the problem of spectral line broadening has been presented in [25 - 28].

The ions and electrons, as perturbers, can be treated separately because of large differences in their masses and velocities. Starting from this assumption, two approximations in Stark broadening theory have been adopted: quasi-static (ion) and impact (electron) approximation.

The impact approximation [16] gives as a result a symmetrical Lorentz form of spectral line:

$$I(\omega) = \frac{w_e}{\pi} \frac{I_0}{(\omega - \omega_0 - d_e)^2 + w_e^2} \quad (13)$$

with a halfwidth  $w_e$  and shift  $d_e$  determined by the following expressions:

$$w_e = -\frac{1}{\hbar} I_m \ll i f^* | H | i f^* \gg = -R_e \ll i f^* | \Phi | i f^* \gg \quad (14)$$

$$d_e = \frac{1}{\hbar} R_e \ll i f^* | H | i f^* \gg = -I_m \ll i f^* | \Phi | i f^* \gg \quad (15)$$

These expressions represent fundamental results of the impact approximation, on the basis of which, using different theoretical approaches, as for example in [4, 29, 30], one can obtain the parameters  $w_e$  and  $d_e$ , determining the Lorentz shape of the spectral lines.

### 2.3d Effect of ions on broadening of isolated lines

In acting as perturbing particles, ions are usually less effective in spectral line broadening than electrons. The exceptions are the lines belonging to one-electron systems and

the lines with forbidden components, though in these cases the ion broadening is not dominant. Because of this, in considering the isolated line profiles, the ion broadening is calculated as a small correction for the electron impact broadening. Calculation of this type of line profile, the so-called  $j(x)$  profile, in quasi-static approximation [1, 4], can be written in the form:

$$j_{A,R}(x) = \frac{1}{\pi} \int_0^\infty \frac{W_R(\beta)d\beta}{1 + (x - A^{4/3}\beta^2)^2} \quad (16)$$

where  $W_R(\beta)$  is the electric microfield distribution,  $\beta$  is the ratio of the electric field and Holtsmark field strength ( $F/F_0$ ), and  $x$  is the reduced frequency, or the reduced wavelength:

$$x = \frac{\omega - \omega_0 - d_e}{w_e} = \frac{\lambda - \lambda_0 - d_e}{w_e} \quad (17)$$

where  $\omega_0$  is the unperturbed frequency and  $\lambda_0$  is the unperturbed wavelength. Expression (16) is also dependent on two additional parameters, the ion broadening parameter  $A$ , and the Debye shielding parameter  $R$ :

$$A = \left( \frac{CF_0^2}{w_e} \right)^{3/4} \quad (18)$$

$$R = 6^{1/3}\pi^{1/6} \left( \frac{e^2}{kT} \right)^{1/2} N^{1/6} \quad (19)$$

where  $C = C_4/e$  and  $C_4$  is the constant of the quadratic Stark effect. The  $j_{A,R}(x)$  profile with the ion effect taken into account, gives the additional shift and line asymmetry. Expressions for the halfwidth and shift of the maximum of line profile, in this case, can be written in the form [19]:

$$w_{st} \simeq 2w_e \left[ 1 + 1.75 \cdot 10^{-4} N_e^{1/4} A (1 - 0.068 \cdot N_e^{1/6} T^{-1/2}) \right] \cdot 10^{-16} N_e \quad (20)$$

$$d_{st} \simeq \left[ d_e \pm 2.00 \cdot 10^{-4} N_e^{1/4} A w_e (1 - 0.068 \cdot N_e^{1/6} T^{-1/2}) \right] \cdot 10^{-16} N_e \quad (21)$$

where the values of  $C$ ,  $d_e$  and  $A$  are taken from the electron density of  $N_e = 1 \cdot 10^{16} \text{ cm}^{-3}$  as it was given in [16].

Because of the asymmetry of the line profile, the shift measured at the half of line height differs from that measured for the maximum. This difference can be expressed by different numerical coefficient in the second term of (21) [7]:

$$d_{st} \simeq \left[ d_e \pm 3.20 \cdot 10^{-4} N_e^{1/4} A w_e (1 - 0.068 \cdot N_e^{1/6} T^{-1/2}) \right] \cdot 10^{-16} N_e \quad (22)$$

The sign before the second term in the shift expressions (21) and (22) is determined by the sign of the electron impact shift  $d_e$  in the range of low temperatures.

The applications of the above expressions for the halfwidth and shift of spectral lines of neutral atoms is limited by the conditions  $R \leq 0.8$  and  $0.05 \leq A \leq 0.5$ . For the values  $A \leq 0.05$ , in considering the emitter-perturber interactions, one has to take into account the quadrupole effect also. The values  $A \geq 0.5$  correspond to the conditions when the linear Stark effect is dominant [16].

In some cases, especially when light ions are considered, the ion motion can not be neglected [16, 31].

### 3. Experimental apparatus and plasma diagnostics

As a plasma source wall stabilized electric arc was used. Diameter of the arc channel is 5 mm and its length is 50 mm. Arc operates in argon under atmospheric pressure with a small addition of hydrogen (2 %), which is used for diagnostic purposes. The current of 30 A is supplied to the arc from the current stabilized ( $\pm 0.3$  %) power supply.

In order to avoid plasma inhomogeneity in the region close to the electrode as well as the distortion of the line profile due to strong self-absorption effect in argon arc plasma, spectroscopic observation of the line shapes has to be performed side-on, i.e. perpendicularly to the arc axis. Since the atmospheric pressure arc plasma is axially inhomogeneous, the Abel inversion procedure has to be applied to recover line profiles from the integral radial intensity measurements.

Optical setup and experimental procedure are described in detail in [32, 33]. Here, minimum details will be given for completeness. The plan-parallel glass plate rotation enables us to shift the plasma image across the entrance slit of the monochromator.

A low pressure argon Geissler tube is used as a reference source of unshifted argon lines. For the shift measurements, the light from both arc plasma and reference source is focused onto the entrance slit of the monochromator through the partially transparent (reflecting) mirror. In this way by using a chopper, the light from the reference source or from the arc plasma can be detected alternatively by the photomultiplier placed at the exit slit of the monochromator.

Radial distribution of electron density  $N_e$  in the range  $(0.74 - 2.90) \cdot 10^{22} \text{ m}^{-3}$  along the plasma radius was determined from halfwidth of the Abeled [34] Balmer  $H_\beta$  line profiles.  $N_e$  measurement is performed in conjunction with theoretical calculations [35]. Electron temperature  $T_e$  in the range (9280 – 10750) K is deduced from [36]. The results are given in the Table 1.

**Table 1.** Plasma diagnostic data.  $r$  is distance from arc plasma axis.

No.	$r$ (mm)	$N_e$ ( $10^{22} \text{ m}^{-3}$ )	$T$ (K)
1.	0	2.90	10760
2.	0.167	2.82	10730
3.	0.333	2.70	10700
4.	0.500	2.46	10550
5.	0.667	2.15	10400
6.	0.833	1.90	10250
7.	1.000	1.60	10050
8.	1.167	1.40	9900
9.	1.333	1.20	9720
10.	1.500	0.98	9520
11.	1.667	0.83	9400
12.	1.833	0.74	9280

Estimated errors of measured electron densities 9 %, were derived from the error in

$H_\beta$  halfwidth measurements and typical uncertainty in  $N_e$  determination from  $H_\beta$  profile [37]. Error in temperature measurements of 3 % was estimated from the uncertainty of  $N_e$  and its influence to  $T_e$  determination.

The scanning of the plasma emission was accomplished, as already mentioned, by rotating plane-parallel plate, in 16 points along the radius plasma column. Later we used only 12 profiles. To preserve achieved accuracy of electron density determination, the last four profiles were excluded from the analysis. Namely, the problem was weakly defined  $H_\beta$  line profiles in outer plasma layers.

#### 4. Results of measurements

In the figure 1a and 1b, set of Ar I 425.936 nm raw experimental profiles and Abel profiles, are given. Since the plasma was radially inhomogeneous, the Abel procedure had to be applied in order to get radial distribution of the profiles. Here we used an Abel inversion procedure based on the Jacobi polynomials, which is described in [34].

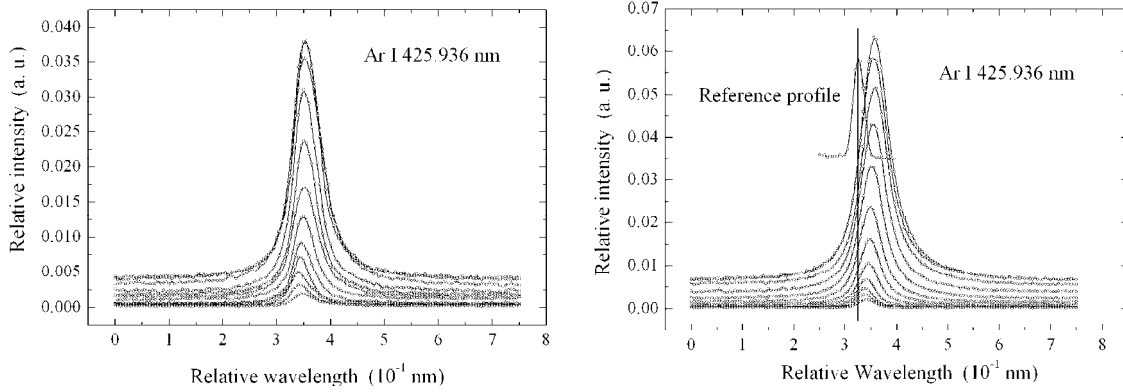


**Figure 1a.** Set of the raw experimental profiles. **Figure 1b.** Set of the profiles after Abel inversion procedure.

**Table 2.** Halfwidth and shift measured data.

No.	Ar I 415.859 nm			Ar I 425.936 nm			Ar I 430.010 nm		
	$4s[3/2]_2^o - 5p[3/2]_2$			$4s'[1/2]_1^o - 5p'[1/2]_0$			$4s[3/2]_1^o - 5p[5/2]_2$		
	$w_m$	$d_{mp}$	$d_{mh}$	$w_m$	$d_{mp}$	$d_{mh}$	$w_m$	$d_{mp}$	$d_{mh}$
	$10^{-1}\text{nm}$	$10^{-1}\text{nm}$	$10^{-1}\text{nm}$	$10^{-1}\text{nm}$	$10^{-1}\text{nm}$	$10^{-1}\text{nm}$	$10^{-1}\text{nm}$	$10^{-1}\text{nm}$	$10^{-1}\text{nm}$
1.	0.439	0.237	0.253	0.593	0.255	0.279	0.476	0.155	0.192
2.	0.429	0.234	0.244	0.568	0.246	0.262	0.468	0.150	0.188
3.	0.416	0.232	0.242	0.558	0.231	0.255	0.442	0.147	0.185
4.	0.396	0.219	0.234	0.535	0.225	0.241	0.428	0.135	0.173
5.	0.366	0.196	0.216	0.492	0.194	0.219	0.402	0.129	0.152
6.	0.324	0.182	0.197	0.441	0.183	0.199	0.366	0.113	0.136
7.	0.296	0.160	0.175	0.399	0.162	0.178	0.326	0.100	0.123
8.	0.261	0.151	0.162	0.333	0.143	0.151	0.300	0.090	0.113
9.	0.221	0.137	0.137	0.309	0.124	0.132	0.254	0.079	0.093
10.	0.181	0.107	0.123	0.254	0.108	0.116	0.225	0.072	0.079
11.	0.150	0.077	0.087	0.244	0.091	0.099	0.190	0.049	0.065
12.	0.126	0.065	0.071	0.214	0.080	0.094	0.164	0.048	0.055

Halfwidth and shift measured data, after Abel inversion procedure, for the three blue Ar I lines are given in Table 2. The numbers in the first column of Table 2 are corresponding to the different values of electron densities and temperatures along the plasma radius as shown in Table 1.

Measured halfwidths are the result of all pressure broadening mechanisms as well as Doppler and instrumental broadening. So, to separate all these broadening contributions, deconvolution procedure is needed. For the shift data, only Stark and van der Waals shift contribute to measured values.

## 5. Separation of various broadening mechanisms

In general case, if two effects cause simultaneous broadening of a spectral line, the resulting profile is not algebraic sum of the profiles. If one effect can be described by the  $A(x)$  function and the other by the function  $B(x)$ , then the resulting spectral distribution is defined by the convolution of these two functions [1, 19]:

$$K(x) = \frac{1}{2\pi} \int_{-\infty}^{\infty} A(y)B(x-y)dy \quad (23)$$

If for example, both functions are of the Gaussian type, the resulting halfwidth is:

$$w_{GR} = (w_{G1}^2 + w_{G2}^2)^{1/2} \quad (24)$$

This can be used for separation of the Doppler and instrumental halfwidths.

However, if functions  $A(x)$  and  $B(x)$  are different, deconvolution is more complex. The solution of the problem of separating halfwidths in the case of convolution of the Lorentz and Gaussian profile, the so-called Voigt profile, has been described in [38]. When deconvolution procedure [38] is used for spectral lines of neutral atoms, an error can be made because asymmetrical Stark  $j(x)$  profile is described by the symmetrical Lorentz profile. The solutions for convolution of  $j(x)$  and Gaussian profile:

$$K(x) = \frac{1}{2\pi} \int_{-\infty}^{\infty} j_{A,R}(y)G(x-y)dy \quad (25)$$

has been given in Ref. 39. The same reference contains the tabulated ratios  $k_j = w_j/w$  and  $k_G = w_G/w$  as a function of  $k = w_{1/10}/w$  for different parameters  $R$  and  $A$ . Deconvolution is carried out in the same way as in the case of the Voigt profile:

$$\begin{aligned} w_G &= k_G w_E \\ w_j &= k_j w_E \end{aligned} \quad (26)$$

where  $w_E$  is halfwidth of the experimental profile. If the whole procedure is followed correctly, then the values  $w_G$  obtained from (26) and  $\beta$  calculated from (24), where, for example,  $w_{G1}$  is the Doppler halfwidth and  $w_{G2}$  is the measured instrumental halfwidth, should be approximately equal.

Instrumental halfwidth for this experiment is 0.0208 nm. The parameter  $R$  is calculated from (19) and parameter  $A$  is derived for this experimental conditions from Ref. 16. The corresponding halfwidths, of the Ar I lines, as the result of the deconvolution procedure, are given in Table 3.

**Table 3.** Results of the deconvolution procedure.

No.	Doppler halfwidth $10^{-1}$ nm	Pressure halfwidth $10^{-1}$ nm	Resonance halfwidth $10^{-1}$ nm	Van der Waals halfwidth $10^{-1}$ nm	Stark halfwidth $10^{-1}$ nm
Ar I 415.859 nm					
1.	0.0489	0.4391	0.0027	0.0102	0.4262
2.	0.0488	0.4288	0.0027	0.0103	0.4158
3.	0.0487	0.4161	0.0028	0.0103	0.4030
4.	0.0484	0.3958	0.0028	0.0105	0.3825
5.	0.0480	0.3661	0.0029	0.0107	0.3525
6.	0.0477	0.3241	0.0030	0.0109	0.3102
7.	0.0472	0.2958	0.0030	0.0112	0.2816
8.	0.0469	0.2613	0.0031	0.0114	0.2468
9.	0.0464	0.2213	0.0032	0.0116	0.2065
10.	0.0460	0.1814	0.0033	0.0119	0.1663
11.	0.0457	0.1501	0.0033	0.0120	0.1347
12.	0.0454	0.1260	0.0034	0.0122	0.1104
Ar I 425.936 nm					
1.	0.0501	0.5931	0.0150	0.0125	0.5657
2.	0.0500	0.5679	0.0150	0.0125	0.5403
3.	0.0499	0.5576	0.0151	0.0126	0.5299
4.	0.0496	0.5347	0.0155	0.0128	0.5064
5.	0.0492	0.4921	0.0159	0.0131	0.4632
6.	0.0488	0.4415	0.0162	0.0133	0.4119
7.	0.0484	0.3991	0.0167	0.0136	0.3688
8.	0.0480	0.3326	0.0171	0.0139	0.3016
9.	0.0476	0.3093	0.0175	0.0141	0.2776
10.	0.0471	0.2543	0.0180	0.0145	0.2218
11.	0.0468	0.2436	0.0183	0.0146	0.2106
12.	0.0465	0.2143	0.0186	0.0148	0.1809
Ar I 430.010 nm					
1.	0.0505	0.4758	0.0029	0.0113	0.4616
2.	0.0505	0.4682	0.0029	0.0113	0.4539
3.	0.0504	0.4424	0.0029	0.0114	0.4281
4.	0.0500	0.4280	0.0030	0.0116	0.4134
5.	0.0497	0.4019	0.0031	0.0118	0.3871
6.	0.0493	0.3663	0.0031	0.0121	0.3511
7.	0.0488	0.3261	0.0032	0.0123	0.3105
8.	0.0485	0.3003	0.0033	0.0126	0.2844
9.	0.0480	0.2539	0.0034	0.0128	0.2377
10.	0.0475	0.2251	0.0035	0.0131	0.2085
11.	0.0472	0.1900	0.0035	0.0133	0.1733
12.	0.0469	0.1636	0.0036	0.0134	0.1466

The data for density of ground state particles, necessary for resonance and van der Waals halfwidth calculations, are taken from Ref. 36. Pressure halfwidth is the sum of resonance, van der Waals and Stark halfwidths.

It is obvious that Stark broadening is the most important broadening effect for this plasma conditions. Estimated errors for Stark halfwidths are between  $\pm 5\%$  and  $\pm 10\%$  for the plasma experimental conditions ranging from the largest to smallest electron density and temperature. Stark halfwidths for Ar I 415.859 nm line are from 97% to 88% of

pressure halfwidths from highest to lowest electron density. Van der Waals halfwidths are from 2.3 % to 9.7 % and resonance halfwidths are from 0.6 % to 2.7 % of pressure halfwidth for plasma conditions in this experiment. The similar results are for Ar I 430.010 nm line.

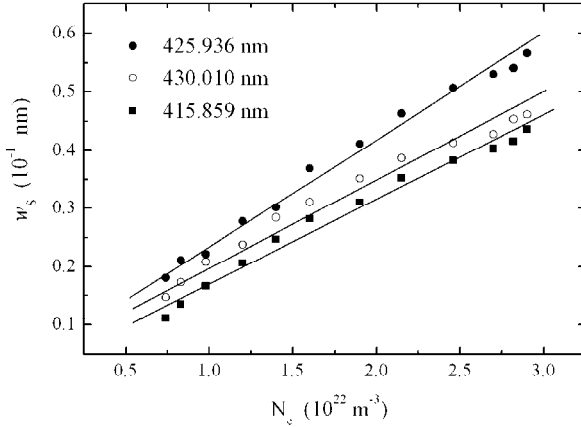


**Figure 2.** The measured Stark halfwidth of Ar I 425.936 nm line versus electron density.

## 6. Shift measurements

Using unperturbed and unshifted lines from reference source, see Fig. 1b, the shifts of three considered argon lines are measured. The results of peak shifts and shifts at the half intensity position are presented in Table 4. Stark and van der Waals shifts are separated.

Estimated errors for Stark shifts are between  $\pm 4\%$  and  $\pm 12\%$  for the plasma experimental conditions ranging from the largest to smallest electron density and temperature.

From Table 4 one can see that van der Waals shift has very small contributions to the total pressure peak shift for 415.859 nm and 425.936 nm lines. It is from 1.5 % to 6 % of

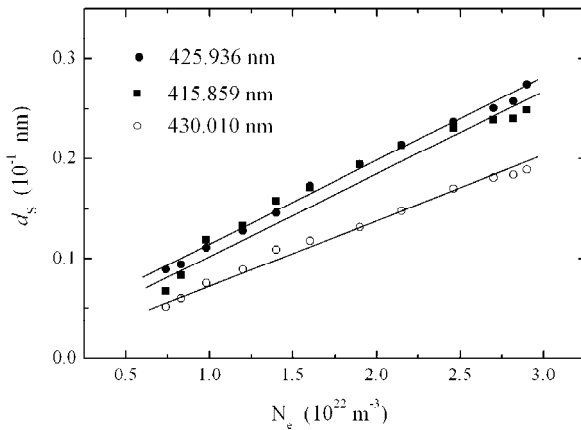


**Figure 3.** The measured Stark shift at the half intensity position of Ar I 425.936 nm line versus electron density.

total pressure peak shift for 415.859 nm and 425.936 nm lines. For these two lines resonance broadening is order of magnitude less than van der Waals broadening, while for Ar I 425.936 nm line these two broadenings are practically the same.

Doppler halfwidths are from 11 % to 36 % of pressure halfwidths from highest to lowest electron density.

Stark halfwidths versus electron density are graphically presented in Fig. 2.

All three spectral argon lines show similar trend versus electron density.

total shift from highest to lowest electron density. The shift of the 430.010 nm line is smaller and the contribution of van der Waals shift is more significant. The peak shift is from 5 % to 18 % of total shift from highest to lowest electron density. Practically, the same contribution of van der Waals shift is to shifts measured at half intensity position.

Example of Stark shift measurements at the half intensity position is shown in Fig. 3.

**Table 4.** Shift measurements.

No.	Measured shifts		Van der Waals shift $10^{-1}$ nm	Stark shifts	
	Peak shift $10^{-1}$ nm	Shift at the halfwidth $10^{-1}$ nm		Peak shift $10^{-1}$ nm	Shift at the halfwidth $10^{-1}$ nm
Ar I 415.859 nm					
1.	0.237	0.253	-0.0034	0.234	0.249
2.	0.234	0.244	-0.0034	0.230	0.240
3.	0.232	0.242	-0.0034	0.228	0.239
4.	0.219	0.234	-0.0035	0.215	0.231
5.	0.196	0.216	-0.0036	0.192	0.213
6.	0.182	0.197	-0.0036	0.178	0.194
7.	0.160	0.175	-0.0037	0.156	0.171
8.	0.151	0.162	-0.0038	0.148	0.158
9.	0.137	0.137	-0.0039	0.133	0.133
10.	0.107	0.123	-0.0040	0.103	0.119
11.	0.077	0.087	-0.0040	0.073	0.083
12.	0.065	0.071	-0.0041	0.061	0.067
Ar I 425.936 nm					
1.	0.255	0.279	-0.0042	0.251	0.275
2.	0.246	0.262	-0.0042	0.242	0.258
3.	0.231	0.255	-0.0042	0.227	0.251
4.	0.225	0.241	-0.0043	0.221	0.237
5.	0.194	0.219	-0.0044	0.190	0.214
6.	0.183	0.199	-0.0044	0.178	0.194
7.	0.162	0.178	-0.0045	0.157	0.173
8.	0.143	0.151	-0.0046	0.138	0.146
9.	0.124	0.132	-0.0047	0.119	0.128
10.	0.108	0.116	-0.0048	0.103	0.111
11.	0.091	0.099	-0.0049	0.086	0.094
12.	0.080	0.094	-0.0049	0.075	0.089
Ar I 430.010 nm					
1.	0.155	0.192	-0.0075	0.151	0.189
2.	0.150	0.188	-0.0075	0.146	0.184
3.	0.147	0.185	-0.0076	0.143	0.181
4.	0.135	0.173	-0.0077	0.131	0.170
5.	0.129	0.152	-0.0079	0.125	0.148
6.	0.113	0.136	-0.0080	0.109	0.132
7.	0.100	0.123	-0.0082	0.095	0.118
8.	0.090	0.113	-0.0084	0.086	0.109
9.	0.079	0.093	-0.0085	0.074	0.089
10.	0.072	0.079	-0.0087	0.067	0.075
11.	0.049	0.065	-0.0088	0.045	0.060
12.	0.048	0.055	-0.0089	0.044	0.051

## 7. Conclusion

Influence of all broadening mechanisms in plasma of wall stabilized electric arc to spectral line widths and shifts is considered. Radial distribution of electron density was in the range of  $(2.9 - 0.74) \cdot 10^{22} \text{ m}^{-3}$  and electron temperature was in the range of  $(10760 - 9280) \text{ K}$ .

In comparison with other broadening mechanisms, for plasma conditions in this experiment, natural broadening is always negligible.

Doppler and instrumental broadening should always be taken into account.

Comparison of pressure broadenings show that Stark effect is dominant for all plasma conditions. Resonance and van der Waals broadening influence on the line halfwidth is small for plasma conditions in this experiment. However, pressure broadening, for this and similar plasma conditions, always has to be corrected to these effects, in order to obtain good and reliable Stark broadening parameters. Stark parameters, both line widths and shifts, are important for plasma diagnostic purposes.

Influence of van der Waals shift to pressure shift is more significant than van der Waals broadening.

Obtained Stark widths and shifts for all three considered lines are in agreement with previous measurements [32, 33].

Since argon atoms are heavy particles ion dynamic effect is not considered in this paper.

## Acknowledgments

This work is partially supported by Ministry of Science, Technology and Development, Republic of Serbia.

## References

1. H. R. Griem, *Plasma Spectroscopy*, p. 63 (McGraw-Hill, New York, 1964).
2. W. L. Wiese, M. W. Smith and B. M. Glennon, *Atomic Transition Probabilities*, Vol. I, p. 194 (Natl. Bur. Stand., Washington DC, 1966).
3. M. Baranger, *Atomic and Molecular Processes*, Ed. D. R. Bates (Academic Press, New York and London, 1962).
4. H. R. Griem, M. Baranger, A. C. Kolb and G. K. Oertel, *Phys. Rev.* **125**, 177 (1962).
5. A. W. Ali and H. R. Griem, *Phys. Rev.* **140**, 1044 (1965).
6. A. W. Ali and H. R. Griem, *Phys. Rev.* **144**, 366 (1966).
7. D. E. Kelleher, *J. Quant. Spectrosc. Radiat. Transfer* **25**, 191 (1981).
8. C. W. Allen, *Astrophysical Quantities*, 3rd Ed. (Athlone Press, New York, 1973).
9. M. Baranger, *Phys. Rev.* **111**, 481 (1958).
10. M. Baranger, *Phys. Rev.* **111**, 494 (1958).
11. M. Baranger, *Phys. Rev.* **112**, 855 (1958).
12. A. C. Kolb and H. R. Griem, *Phys. Rev.* **111**, 514 (1958).
13. M. Baranger, *Atomic and Molecular Processes*, Ed. D. R. Bates (Academic Press, New York, 1962).

14. R. G. Breene, *Handbuch der Physik*, Vol. 27, Ed. S. Flugge (Springer-Verlag, Berlin and New York, 1964).
15. I. I. Sobelman, *An Introduction to the Theory of Atomic spectra*, Ed. G. K. Woodgate (Pergamon Press, New York, 1972).
16. H. R. Griem, *Spectral Line Broadening by Plasmas*, (Academic Press, New York, 1974).
17. H. R. Griem, *Advances in Atomic and Molecular Physics*, Vol. 11, Ed. D. R. Bates and B. Bederson (Academic Press, New York and London, 1975).
18. V. S. Lisica, *UFN* **122**, 449 (1977).
19. N. Konjević and J. R. Roberts, *J. Phys. Chem. Ref. Data* **5**, 209 (1976).
20. N. Konjević and W. L. Wiese, *J. Phys. Chem. Ref. Data* **5**, 295 (1976).
21. N. Konjević, M. S. Dimitrijević and W. L. Wiese, *J. Phys. Chem. Ref. Data* **13**, 619 (1984).
22. N. Konjević, M. S. Dimitrijević and W. L. Wiese, *J. Phys. Chem. Ref. Data* **13**, 649 (1984).
23. N. Konjević and W. L. Wiese, *J. Phys. Chem. Ref. Data* **19**, 1307 (1990).
24. N. Konjević, A. Lesage, J. R. Fuhr and W. L. Wiese, *J. Phys. Chem. Ref. Data* **31**, 819 (2002).
25. J. R. Fuhr, W. L. Wiese and L. J. Roszman, NBS Spec. Publ. 366 (U. S. Gov. Print. Office, Washington DC, 1972).
26. J. R. Fuhr, L. J. Roszman and W. L. Wiese, NBS Spec. Publ. 366, Suppl. 1 (U. S. Gov. Print. Office, Washington DC, 1974).
27. J. R. Fuhr, G. A. Martin and B. J. Specht, NBS Spec. Publ. 366, Suppl. 2 (U. S. Gov. Print. Office, Washington DC, 1975).
28. J. R. Fuhr, and A. Lesage, NIST Spec. Publ. 366, Suppl. 4 (U. S. Gov. Print. Office, Washington DC, 1993).
29. J. Cooper and G. K. Oertel, *Phys. Rev. Lett.* **18**, 985 (1967).
30. J. Cooper and G. K. Oertel, *Phys. Rev.* **180**, 286 (1969).
31. J. Barnard, J. Cooper and E. W. Smith, *J. Quant. Spectrosc. Radiat. Transfer* **14**, 1025 (1974).
32. S. Djurović, Z. Mijatović, R. Kobilarov and N. Konjević, *J. Quant. Spectrosc. Radiat. Transfer* **57**, 695 (1997).
33. S. Djurović, D. Nikolić, Z. Mijatović, R. Kobilarov and N. Konjević, *Plasma Sources Sci. Technol.* **57**, 95 (2002).
34. S. Djurović, *J. Res. Phys.* **28**, 153 (1999).
35. C. R. Vidal, J. Cooper and E. W. Smith, *Astrophys. J. Ser.* **25**, 37 (1973).

36. C. H. Popenoe and J. B. Shumaker Jr., *J. Res. NBS, Phys. Chem.* **69A**, 495 (1965).
37. W. L. Wiese, D. E. Kelleher and D. R. Paquette, *Phys. Rev. A* **6**, 1132 (1972).
38. J. T. Davies and J. M. Vaughan, *Astrophys. J.* **137**, 1302 (1963).
39. Z. Mijatović, R. Kobilarov, B. T. Vujičić, N. Konjević and D. Nikolić, *J. Quant. Spectrosc. Radiat. Transfer* **50**, 339 (1993).

# Journal of Research in Physics

Volume 30    Number 1    December 2004

## CONTENTS

F. Skuban, S. R. Lukić, Yu. S. Tver'yanovich, D. M. Petrović, S. J. Skuban	<i>Magnetic Susceptibility of Glasses of the Sb-As-S-Se-I System</i>	1
M. Vučinić-Vasić, M. Mitrić, A. Kapor, N. Furmanova	<i>Structure and Magnetic Properties of the Solid Solutions of <math>(Al_{1-x}Fe_x)(H_2O)_6(NO_3)_3 \cdot 3H_2O</math> Type</i>	9
D. Ž. Obadović, M. Garić, A. Vajda, A. Bubnov, M. Kašpar, V. Hamplova	<i>Structural Properties of Ferroelectric Liquid Crystals with 2-Alkoxypropionate Chiral Group by X-ray Diffraction</i>	19
Ljubisav Novaković	<i>Three-Particle Interactions with a Possible Application to Cold Fusion</i>	27
D. S. Mrđa, I. S. Bikit, I. V. Aničin, J. M. Slivka, J. J. Hansman, N. M. Žikić-Todorović, E. Z. Varga, S. M. Čurčić, J. M. Puzović	<i>Background Reduction Using Fe and Pb Shielding</i>	49
E. Z. Varga, I. S. Bikit, J. M. Slivka, N. M. Žikić-Todorović, D. S. Mrđa, S. M. Čurčić, M. J. Vesković	<i>Calibration of GMX HPGGe Detector with NBS Reference Source</i>	55
S. M. Čurčić, I. S. Bikit, J. M. Slivka, D. S. Mrđa, N. M. Žikić-Todorović, E. Z. Varga, M. J. Vesković	<i>Effect of Self-Absorption in Voluminous Sources in Gamma-Spectrometry</i>	61
S. Hamzaoui, S. Djurović, M. Čirišan and Z. Ben Lakhdar	<i>Study of the Broadening Mechanisms in Plasma of Wall Stabilized Electric Arc</i>	67